

**MODELLING, ASSESSMENT AND APPLICATIONS OF MULTIPLE
QUANTUM WELL OPTICAL ABSORPTION MODULATORS**

Peter John Stevens

Thesis submitted for the degree of Ph.D,
University of London.

November 1989.

ProQuest Number: 10610558

All rights reserved

INFORMATION TO ALL USERS

The quality of this reproduction is dependent upon the quality of the copy submitted.

In the unlikely event that the author did not send a complete manuscript and there are missing pages, these will be noted. Also, if material had to be removed, a note will indicate the deletion.



ProQuest 10610558

Published by ProQuest LLC (2017). Copyright of the Dissertation is held by the Author.

All rights reserved.

This work is protected against unauthorized copying under Title 17, United States Code
Microform Edition © ProQuest LLC.

ProQuest LLC.
789 East Eisenhower Parkway
P.O. Box 1346
Ann Arbor, MI 48106 – 1346

to my parents

ABSTRACT

This thesis describes a wide-ranging investigation of the multiple quantum well electroabsorption modulator, from the physical effect governing its operation to the systems in which it might be used.

First, the important properties of the device are discussed and the parameters describing the modulation performance defined. A physical model for the field dependent absorption spectrum of quantum well material is developed and used to assess, understand and model the modulator operation. For realistic results this calculation includes the reduction in oscillator strength and the field-enhanced broadening mechanisms. These are inhomogeneous broadening mechanisms caused by well width fluctuations and field variations within the device. The theory is used to explain results from an experimental investigation into modulators of different well widths.

Using the above model the optimal design of a non-resonant modulator is determined. It is found that in a transverse modulator, for operation at a particular voltage, there is an optimum thickness of device and this is used to investigate expected device performance. The work is briefly extended to embrace resonant devices such as the asymmetric Fabry-Perot modulator.

Some applications of the modulator are then considered. The design of an optical interconnect for an electronic chip is investigated, with the intent of minimising the power dissipation for a optical link and comparing that dissipation with that of the equivalent electronic link. Finally new fibre-optic architectures are proposed that utilise the functional duality of the MQW diode as both modulator and detector.

TABLE OF CONTENTS

	Page Number
Abstract	3
Table of Contents	4
Acknowledgements	6
Preface	8
<i>Chapter 1</i> Description of Modulator	
1.1 Device Operation	11
1.2 Material Systems and their growth	20
1.3 Device Performance	23
1.4 Published Modulator Results	28
1.5 Summary	31
<i>Chapter 2</i> Calculation of Field Dependent Absorption	
2.1 Introduction	33
2.2 Evaluation of Subband Energies	34
2.3 Determination of Well Widths	40
2.4 Calculation of Absorption Spectra	42
2.5 Broadening Mechanisms	48
2.6 Comparison with Experimental Spectra	56
2.7 Effect of Well Width on Absorption Spectra	64
2.8 Summary	67
<i>Chapter 3</i> Optimisation of Device Modulation	
3.1 Introduction	70
3.2 Waveguide Devices	70
3.3 Transverse Modulator Optimisation Technique	72
3.4 Bias-Absorbing, 100 Å Well Width Performance	75
3.5 Effect of Well Width on Modulation	79
3.6 Bias-Transmitting Mode	81
3.7 Resonant Devices	83
3.8 Comparison with Experimental Results	86

3.9 Summary	87
<i>Chapter 4 Modelling for (GaIn)As/InP Material</i>	
4.1 Introduction	91
4.2 Physical Modelling	91
4.3 Non-Resonant Modulator Modelling	93
4.4 Resonant Modulators	98
4.5 Summary	99
<i>Chapter 5 Applications in Fibre Optics</i>	
5.1 Introduction	102
5.2 High Speed Fibre Optic Links	102
5.3 Novel Fibre Optic Architectures	104
5.4 Summary	112
<i>Chapter 6 MQW Modulators for Optical Interconnects</i>	
6.1 Introduction	114
6.2 Transmitter Design	117
6.3 Temperature Sensitivity of Modulators	121
6.4 Implications for System Architectures of Temperature Sensitivity	124
6.5 Receiver Design	126
6.6 Optical Power Budget	132
6.7 Causes of Power Dissipation	132
6.8 Calculation of Power Dissipation	134
6.9 Comparison with Electrical Interconnect	139
6.10 Summary	141
Conclusions	143
List of Publications	146
References	147

ACKNOWLEDGEMENTS

I have found that studying for a doctorate is not unlike entering an archery competition. You've never held a bow and arrow in your life before, but they tell you "you're young, you'll learn"; and you do. But then a mightier problem arises: there don't appear to be any targets. You direct your fire in one direction, and then another, just hoping your arrows make their mark. Eventually you realise the object is to shoot where nobody has shot before, and the more you shoot, the more clearly your imagination defines a target. You coast along for a while and then you encounter your final hurdle. You have to track down all of your previous arrows and try and justify shooting where you did.

Needless to say, the above is a somewhat disconcerting procedure. Thankfully, I have been surrounded by people who have helped to make it enjoyable, and but for them I doubt whether I would have reached this final showdown. Principal among these must be my supervisor, Gareth Parry, who has set a shining example of support, encouragement and enthusiasm in a frequently selfish academic world. Secondly, Mark Whitehead has been an invaluable colleague whose many late night sessions have provided a solid experimental foundation to my work. Craig Tombling has been my right hand man ever since joining the department, and life will seem strange when I can turn around and ask silly questions no more. Mark Abbott on the other hand has saved me many an unhappy hour sitting in front of a computer screen getting increasingly baffled. The reader also has cause to be thankful. If it weren't for Mark A., they would be reading a dot matrix printer output with hand drawn equations.

I could go on and on, but from now on I intend to list everyone else. Each will know his own valued and individual contribution. Many thanks go to John Midwinter, Chris Carey, Tony Rivers, Tony Overbury, Mic Taylor, Marc Desmulliez, Alex Gracian, Ian Bennion, Andy Moseley, David Robbins, Mike Wale, John Roberts, Karl Woodbridge, Peter Dobson, Peter Blood, Mike Shorthose, David Guy, Takaaki Mukai, Tatsuya Kimura, Hiroshi Kanbe, Kevin Jelley, Prof. M.Yamanishi, Prof. M.Asada and the rest of the digital optics group at UCL. I gratefully acknowledge the SERC and Plessey Research (Caswell) for financial support for this project. NTT, Plessey and Cable and Wireless also provided me the unique opportunity of visiting Tokyo for three months.

Finally I come to my family and friends. Without them, I would not have been able to enter the archery contest, nor contemplate what I might go on to do henceforth.

PREFACE

The quantum well electroabsorption modulator, first proposed and demonstrated by AT&T Bell laboratories [Wood et al., 1984], was developed for a variety of reasons. Firstly, it has provided interesting new physics to understand and model. Secondly, at the time of its development people were seeking alternative ways to obtain optical non-linearities for all-optical processing and small hybrid circuits made up with MQW modulators such as the SEED [Miller, D.A.B. et al., 1984] and the T-SEED [Wheatley et al.] gave attractive non-linear characteristics. Finally, the MQW modulator provides an efficient and flexible interface between electronics and optics that allows electronics access to the enormous communication capabilities that optics offers. It is really the latter that is still driving development today.

When I started this work, working GaAs/(GaAl)As MQW modulators had been reported, and it was projected that I should develop equivalent devices in the (GaIn)As/InP material system. After setting up fabrication and measurement facilities, the material available then did not give very encouraging results, and it was not possible to proceed with an experimental study. My response to this was to develop a greater understanding for, and a model for, the physical effect utilised in the modulator: electro-absorption. Since many high quality experimental results were being generated by the group then in the GaAs/(GaAl)As system, I concentrated upon that system. This work forms the basis for chapter 2: the first realistic model for field-dependent absorption in MQWs to include all the significant spectral broadening mechanisms. Much of this work was first published in the IEEE Journal of Quantum Electronics.

A natural extension of the physical modelling was to consider the device performance. A colleague (M.Whitehead) was investigating resonant, or Fabry-Perot modulators. My work was initially directed at non-resonant modulators, for which no systematic study of the potential modulation performance had been carried out. In these non-resonant modulators the achievable modulation is limited by two conflicting requirements: the absorption is such that the device should be reasonably thick, but the thicker the device, the higher the voltage required to give the high fields needed. A method of optimising the number of wells in the device and using this to determine what modulation could be expected in diodes of differing well width and material quality, can be found in chapter 3 and was in part published in the Journal of Lightwave Technology.

Meanwhile my colleague's research had culminated in the invention of the asymmetric Fabry-Perot modulator (AFPM) [Whitehead et al., 1989b], and it became clear the AFPM offered substantial improvements in achievable modulation, and that my work should at least address it. A simple extension of non-resonant device optimisation to the AFPM was possible and is also covered in chapter 3.

In chapter 4 we use the same model and optimisation techniques developed for GaAs/(GaAl)As, to investigate (GaIn)As/InP performance. The same type of electroabsorption modulation is possible in (GaIn)As/InP but modulators require higher voltages than in the GaAs based system, confirming the now available experimental results from AT&T, Plessey, RSRE and British Telecom.

After having determined what performance we can expect from MQW diodes, I turned to the applications in which they might be used. One branch of such applications is in fibre-optics: already an important commercial use of other III-V devices. Chapter 5 considers two classes of fibre-optic applications, the first utilising the very high speed of MQW modulators for clean high frequency external modulation of a laser source, and the second using the functional duality of the MQW modulator as both a modulator and detector in novel networks for local area links. I had intended to expand the work on the latter experimentally, but at that time I left to spend 3 months at NTT research laboratories in Tokyo, Japan, modelling the characteristics of quantum well laser amplifiers. This work, although closely related to the modelling presented here, is not directly relevant to the thesis itself, and is being submitted as a separate paper. This paper will also be sent to the IEEE Journal of Quantum Electronics.

On my return from Japan, I was invited to work within the ESPRIT programme on optical interconnects (OLIVES). In part this has meant the development and measurement of low capacitance modulators designed to work at high speed, but also a more general investigation of the practical design of the system. This survey concludes the topics covered in this thesis and is described in chapter 6.

Chapter 1

DESCRIPTION OF THE MODULATOR

1.1 Device Operation

An electroabsorption modulator utilises changes in absorption close to the bandedge of semiconductor material on the application of an electric field. The changes in absorption cause changes in transmission and hence provide a means of modulating the light as it passes through the device. In bulk semiconductors the field dependent change in the absorption spectrum is called the Franz-Keldysh effect. However multiple quantum well material offers greater changes in absorption because of the following differences between it and bulk semiconductor:

- i) A step-like density of states at the band-edge
- ii) The increased strength of exciton transitions
- iii) The quantum confined Stark effect (QCSE).

But what is a quantum well ? Quantum well material is composed of ultra-thin layers of different semiconductors, typically only 100 Å (or about 30 monolayers) thick, as shown in figure 1.1.1. The materials have different band energies and the electrons prefer to remain in the lower gap or well material. However they are quantum-mechanically confined in the narrow wells, causing fundamental changes to the density of states in the valence and conduction bands and hence to the shape of the absorption spectra. Figure 1.1.2 illustrates how the density of states is altered as the dimensionality of the quantum confinement is increased. Full three dimensional confinement gives rise to well defined energy levels as is seen in a hydrogen atom. A quantum well only gives confinement in one dimension and hence a steplike density of states is seen. The conduction and valence band split up into a series of subbands, the edges of which define the position of the step in the density of states function. The bottom of each subband is at a level equal to the energy level in the one dimensional potential well defined by the conduction or valence band-edges of the two materials. There are two sets of valence subbands belonging to the heavy and light hole states respectively.

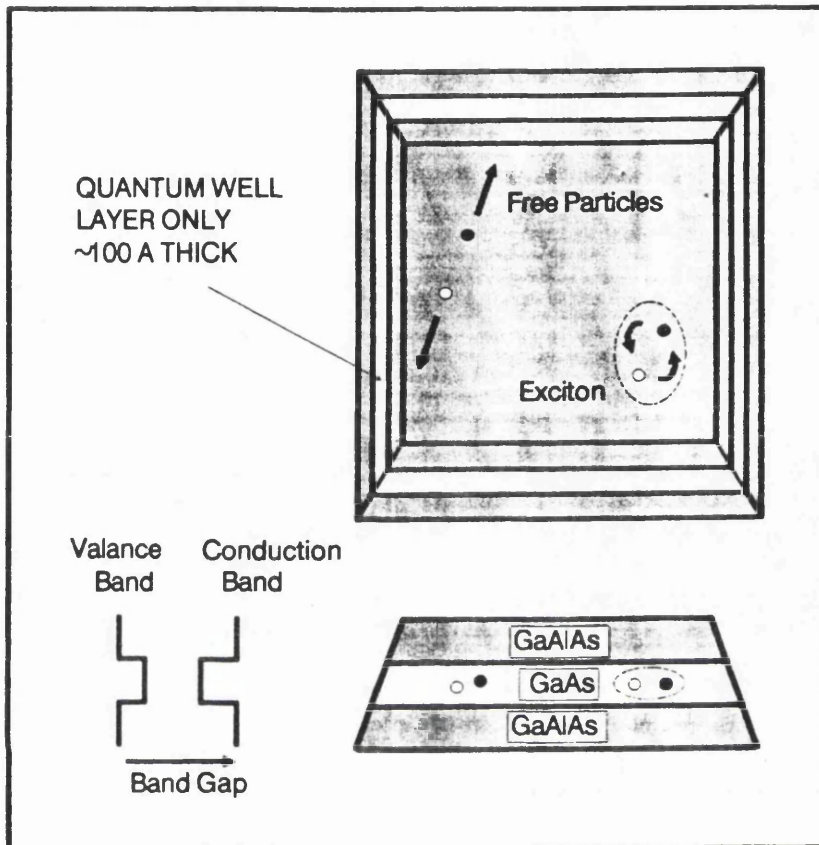


Figure 1.1.1 A GaAs/(GaAl)As quantum well showing how electrons and holes are confined in the well material. The electrons and holes are either free particles or form a bound exciton pair.

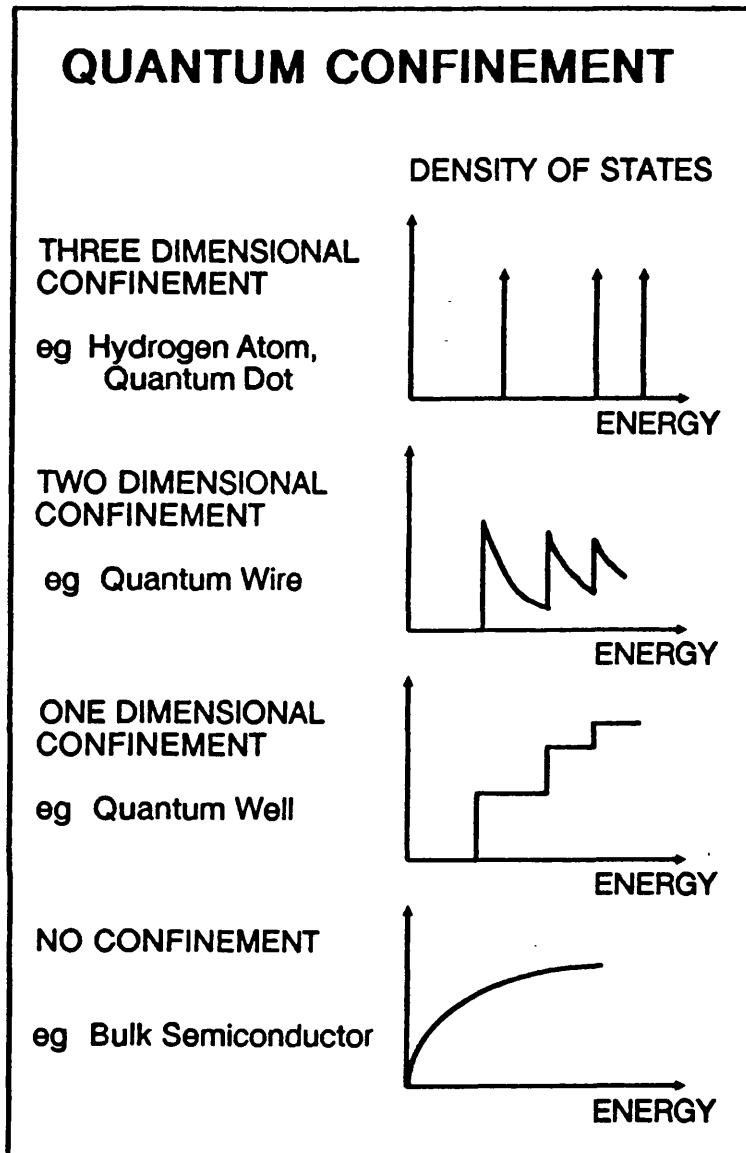


Figure 1.1.2 The shape of the density of states function for different degrees of quantum confinement.

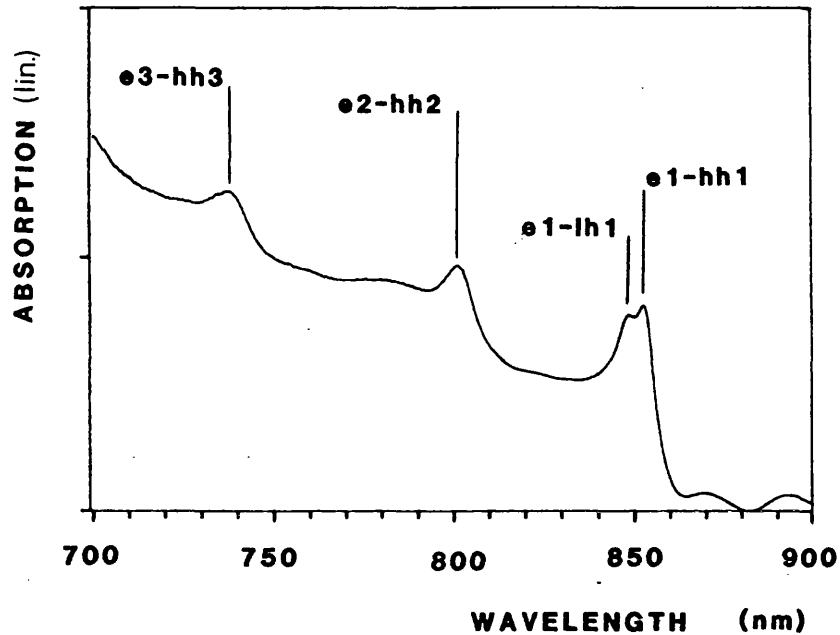


Figure 1.1.3 Absorption spectrum of GaAs/(GaAl)As MQWs with 100 Å wells and 100 Å barriers. Excitonic transitions between the electron (e) and heavy (hh) and light (lh) subband are labelled. Note that the small undulation in absorption longer than the e1-hh1 bandedge are spurious and caused by Fabry-Perot effects. Measurement by M.Whitehead.

The step-like density of states is clearly evident in the experimental absorption spectrum of figure 1.1.3. However extra transitions are seen just below the edge on each subband. These are exciton states which arise when the electron and hole formed by the absorption of a photon do not have enough energy to escape from one another and hence form a bound state, as illustrated in figure 1.1.1. This state is confined in three dimensions by the coulomb potential and hence has a well defined energy level rather than forming part of a continuum. Excitons are not exclusive to MQW material and are also formed in bulk material although quantum confinement shrinks the size of the exciton and hence increases its oscillator strength with the result that they are easily resolved even at room temperature [Dingle et al., 1974].

The QCSE is a shift of the subbands and associated exciton transitions to

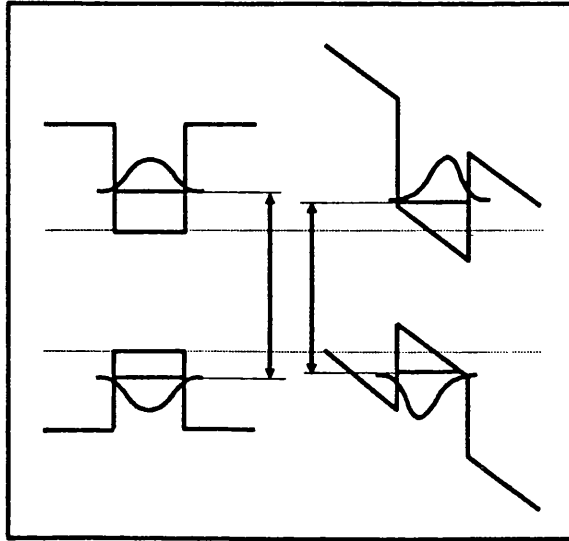


Figure 1.1.4 Illustration of the Stark shift of subband levels in quantum wells on the application of an electric field.

lower energy on the application of an electric field perpendicular to the wells. The size of this shift has been explained [Miller,D.A.B. et al. 1985] by the shifts in the subband energies as the wells become tilted, as shown in figure 1.1.4. But equally important is the fact that the excitons remain resolvable as they shift because the barriers on either side of the well inhibit field-induced ionization of the exciton and hence prevent the transition broadening through the Heisenberg uncertainty principle. The shift of the excitons and subband gap can be clearly seen in the absorption spectra shown in figure 1.1.5. Along with the shift, a reduction in the initial transition's oscillator strength and some field enhanced broadening is evident. This field enhanced broadening is caused by inhomogeneous mechanisms linked to interface roughness and variations in field over the wells. As the initially visible transitions subside, initially forbidden transitions grow so that the area under the absorption spectrum stays constant [Miller,D.A.B. et al.,1986]. A model for calculating the absorption spectra will be presented in chapter 2.

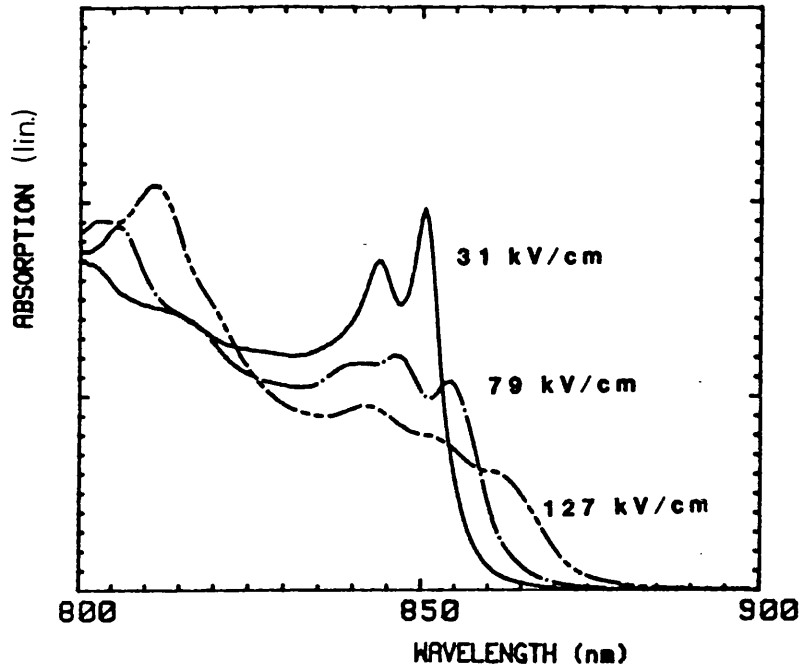


Figure 1.1.5 Field dependent absorption spectrum of GaAs/(GaAl)As MQWs (98 Å wells/111 Å barriers) derived from photocurrent measurements on PIN diode. Measurement by M.Whitehead.

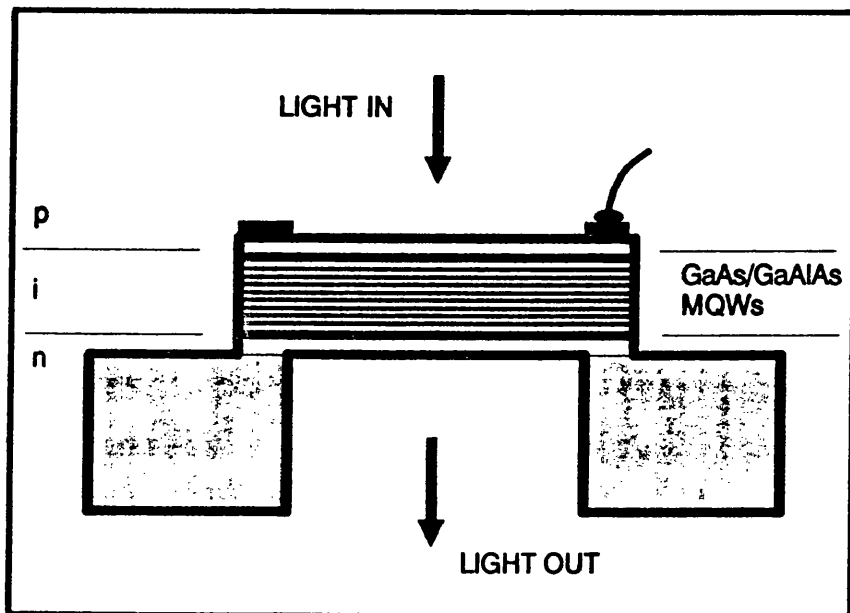


Figure 1.1.6 Schematic diagram (not to scale) of p-i-n structure used for a transverse MQW modulator.

In order to apply the electric field over the wells without large currents flowing through the material, the quantum wells are generally incorporated within the intrinsic region of a p-i-n diode structure as illustrated in figure 1.1.6. A sizeable electric field can then be applied by reverse biasing the device. Typical bias dependent transmission measurements on such a device give the spectra shown in figure 1.1.7. It is interesting to note that this structure is also that of an effective photodiode thus giving important duality of function to the device.

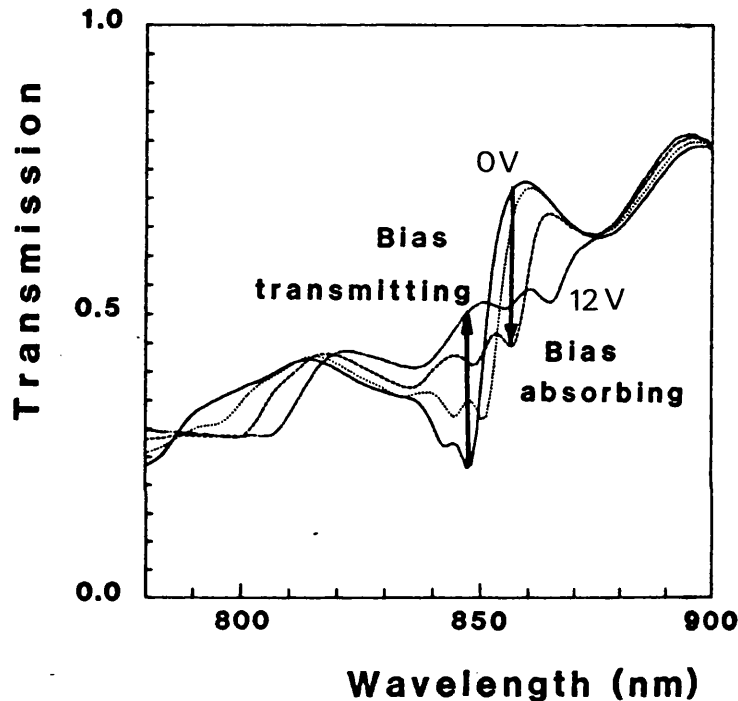


Figure 1.1.7 Transmission spectra on a GaAs/ (GaAl)As MQW p-i-n diode with 60 periods of 87 Å wells and 60 Å barriers, for biases of 0,4,8 and 12V. Modulator operates in either a bias absorbing mode at the biased exciton peak or in a bias transmitting mode on the unbiased exciton peak. Measurement by M.Whitehead.

Quantum well modulators can be made in two geometries: with the light travelling parallel to the wells within a waveguide structure [Tarucha et al. 1985, Wood et al. 1985b] and with the light propagating perpendicular in the transverse structure [Wood et al. 1984] as illustrated in figure 1.1.8. Waveguide modulators offer a much larger interaction length and hence better modulation can be obtained. They are particularly suited to integrated optic applications in which other waveguide components surround them.

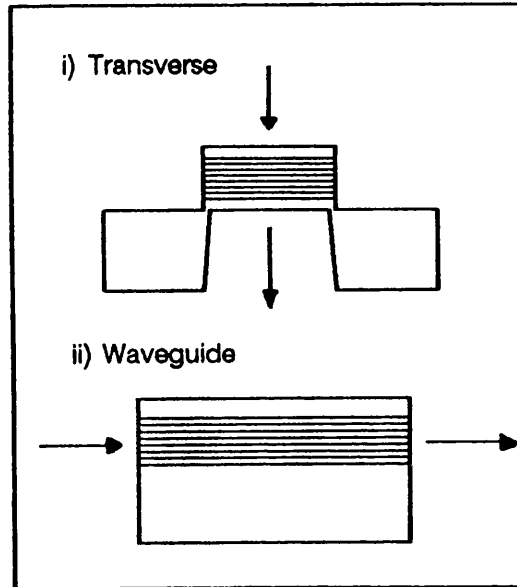


Figure 1.1.8 Illustration of normal incidence (transverse) or waveguide geometries for MQW modulators.

The principal attraction of the transverse modulator is the ease with which one can couple into it. They are two distinct types: non resonant ones with anti-reflection coatings on one or both surfaces, or resonant ones with reflections on both surfaces. The *non-resonant* modulator is limited in achievable contrast by the thickness of the absorbing region. A reflector on the back surface can change a transmission modulator to a reflective one with twice the optical interaction length [Boyd et al. 1987]. In GaAs/(GaAl)As devices the reflector removes the need to etch away the absorbing substrate.

In order to use the limited interaction length most effectively transverse modulators need to work at wavelengths where the change in absorption is largest, or more specifically, at the exciton peaks. However there are two possible modes of operation. The first uses a longer wavelength than the bandedge at zero field. A bias is then applied to shift the exciton peak to that wavelength, with the large increase in absorption reducing the transmission through the quantum wells. This will be henceforth referred to as a *bias-absorbing* mode. On the other hand one might choose the zero-field exciton wavelength, and then the effect of bias will be to decrease the

absorption and therefore increases the transmission: a *bias-transmitting* mode. These are both illustrated in figure 1.1.7. Waveguide devices are normally only operated in a bias-absorbing mode because a low value of absorption is required in the high transmission state so that the insertion loss is kept small.

Quantum well *resonant* modulators were first suggested in high finesse forms whose operation relied upon the electrorefractive shift of the transmission resonance [Guy et al., 1986]. These high finesse modulators were difficult to grow, and their operation was very sensitive to environmental fluctuations as a result of the narrow resonance linewidth. More recently, Whitehead and Parry have proposed and demonstrated the *asymmetric Fabry-Perot modulator* (AFPM) [1989a]. Figure 1.1.9 compares the non-resonant reflection modulator with the AFPM. The operation of the AFPM relies upon the destructive interference between the front surface reflection and the sum of back surface reflections. With low absorption in the cavity the back surface reflections dominate and a reasonable reflectivity in the on-state is possible. When the the absorption is increased one eventually reaches a state in which complete destructive interference can occur with a

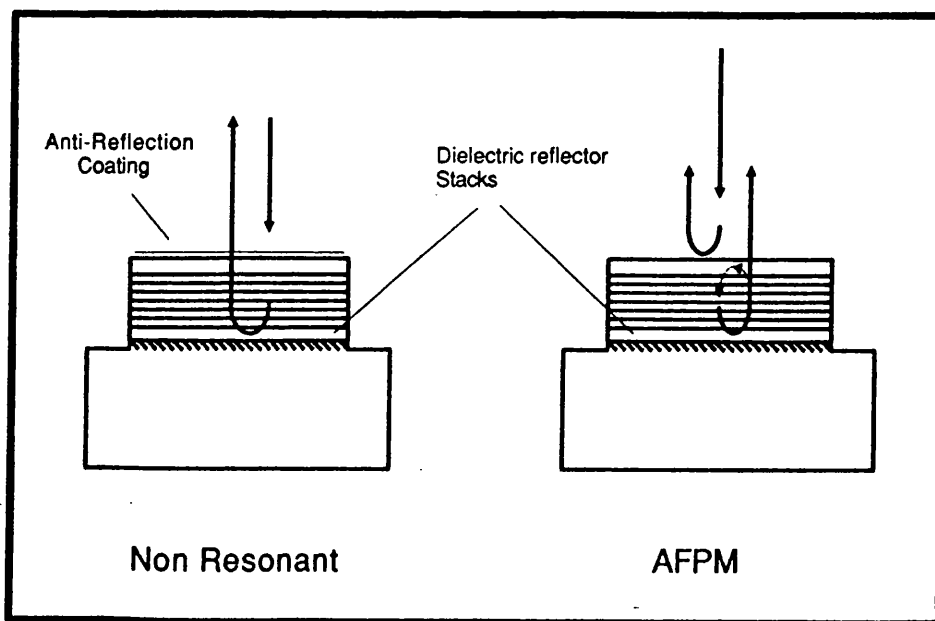


Figure 1.1.9 Cross sections through a non-resonant reflection modulator and the AFPM. The AFPM has a front reflection that destructively interferes with the back reflections. At a particular absorption in the QWs the overall reflection is zero.

zero reflection output. This gives a theoretically infinite contrast. The operation of the AFPM can be seen in figure 1.1.10, which shows almost zero reflection in the biased state at the resonant wavelength.

In addition to giving very high contrast the AFPM also makes a very effective photodetector, since most of the incident light in the zero reflectivity resonant state gets absorbed within the cavity. Thus a high quantum efficiency can be achieved without needing an extensive intrinsic region and the accompanying high reverse bias voltages.

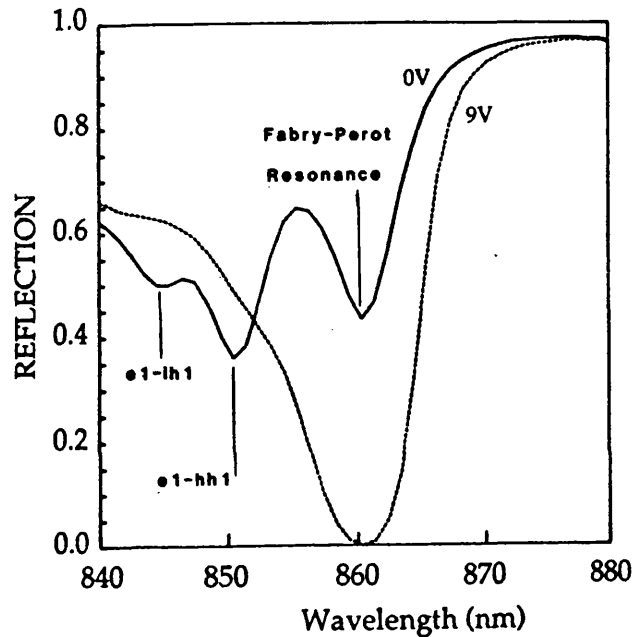


Figure 1.1.10 Bias dependent reflection spectra for AFPM device with 75 periods of 95 Å wells and 60 Å barriers with front and back reflectivities of 30% and >95%.

1.2 Material Systems and their Growth

The realization of the the quantum well modulator has been made possible by some remarkable achievements in the growth of thin layers of III-V semiconductor material. It is not the purpose of this work to describe growth methods in detail but it is worth briefly mentioning the competing techniques used for growing thin semiconductor layers.

The most important material parameters are the quality of the interface between the well and barrier and the background doping in the MQW

intrinsic region. Liquid phase epitaxy (LPE) is a relatively simple technique suitable for the growth of layers not less than 1000 Å. Since the effects of quantum confinement are not really evident until the layer thickness is less than the bulk material exciton radius (≈ 300 Å in GaAs), more sophisticated techniques are required for the growth of quantum wells. The two most common techniques are molecular beam epitaxy (MBE) [Gossard] and metal-organic vapour-phase epitaxy (MOVPE) [Frijink et al., Roberts et al.]. Both techniques can produce interfaces between layers that are smooth to only a few monolayers. The advantages of MBE have been cited as sharper interfaces, in-situ RHEED surface analysis and the non-toxicity of the chemicals used. MOVPE however is better able to grow phosphorus containing compounds, and allows rapid source reloading and reprocessing. While it is difficult to be certain which of these techniques will be favoured in the future it is reasonable to assume that MOVPE will prove more useful in large scale production whereas MBE might be more valuable for research. There is also a hybrid technique called gas-source MBE that combines some of the advantages of both MBE and MOVPE.

The above techniques are not solely important for the manufacture of active optical devices, and somewhat thicker multilayers are being grown as optical filters. Most useful of these is the quarter wavelength stack used as a reflector [van der Ziel and Ilegems, Gourley and Drummond], as it makes possible the fabrication of integrated normal incidence reflective [Boyd et al. 1987] and Fabry-Perot modulators [Whitehead et al. 1989b].

Quantum wells have been grown in a number of material systems and these can be split into two categories : lattice matched and strained layer systems. In lattice-matched QWs the well and barrier material have the same lattice spacing as the substrate and hence the strain in the materials is relatively small. The most developed of all material systems used for QWs is GaAs/(GaAl)As which operates at wavelengths in the range 800-870 nm. This wavelength is determined by the thickness of the quantum wells, and as will be shown later, this well width is also important in governing modulation characteristics. Background dopings of under 10^{15} cm⁻³ and interface smoothness of less than a monolayer are now achievable and a clear QCSE has been seen in both MBE- [D.A.B.Miller et al. 1985, Whitehead et al. 1987a] and MOVPE-grown material [Whitehead et al. 1987b]. From a more theoretical viewpoint, this material is also attractive because a consistent set of effective masses and band offsets have been found [R.C.Miller et al.,

Duggan et al.]

However, there is considerable interest in developing other MQW material systems, partly in order to achieve a transparent substrate at the operating wavelength and partly to operate at specific wavelengths such as the 1550 nm optical fibre low loss region. The system which has progressed furthest to date has been (GaIn)As/InP in which a clear QCSE has recently been seen in a MOVPE grown sample [Bar-Joseph et al., Moseley et al.]. There is, however, an additional uncertainty in the composition of the ternary well material. This complication has delayed a proper characterisation of the material and there are many conflicting values for the band offsets, effective masses and band nonparabolicities [Forrest et al., Lang et al., Skolnick et al., Sauer et al., Sarkar et al.].

The exciton peak wavelengths for the (GaIn)As/InP system are in the range 1450-1650 nm, but unfortunately, for operation at 1.55 μm , the well width is rather narrow ($\approx 70 \text{ \AA}$) and large operating voltages are required. This has led to the use of the quaternary system (GaIn)(AsP)/InP so that the band-gap of the well material can be altered while retaining a lattice match [Zucker et al.].

MQW material of (GaIn)As wells but AlInAs barriers has also been grown, but with less success [Wakita et al. 1985] although the reason for this is not yet clear. Encouraging results have also been seen in GaSb/(GaAl)Sb [Miyazawa et al.], but there is even less known about it, than (GaIn)As/InP and it requires growth on rare GaSb substrates and the handling of nasty antimony compounds.

Recently it has been discovered that MQWs can be grown with wells and barriers of different lattice constants. The thickness of the layers is small enough so that the materials become highly strained but have a remarkably low density of dislocations. The most commonly used strained-layer material system is (InGa)As/GaAs [Das et al.] in which one has a transparent substrate as well as the ability of choosing both the well material band-gap and the well width to alter the wavelength. On a slightly different note, there is also considerable interest in growing the quantum well material on silicon substrates [Barnes et al.]. This might make the modulators cheaper to manufacture, more robust, and more speculatively, allow them to be integrated with electronic circuitry or a silicon motherboard.

1.3 Modulator Performance

The important device characteristics are:

i) Degree of Modulation

An ideal modulator transmits all of the incident light in its on-state, and absorbs it all in its off-state. In practice this ideal modulation is not realised and in optimising the device one must choose some figure of merit to describe the modulation. Unfortunately, different applications require different figures of merit: some prefer a high on-state, while others require a high contrast ratio between the on and off states.

Binary modulation is fully characterised by the transmission through the device in the on- (T_{hi}) and off- (T_{lo}) states, as shown in figure 1.3.1. The contrast ratio (T_{hi}/T_{lo}) and modulation depth ($(T_{hi}-T_{lo})/T_{hi}$) are both often used. In certain application, especially where optical signals are merged such as an optical logic gate or telecommunications switch [Ajisawa et al.], a high contrast is a necessity. The problem with using it as a figure of merit is that it can often mask a very high insertion loss (T_{hi}).

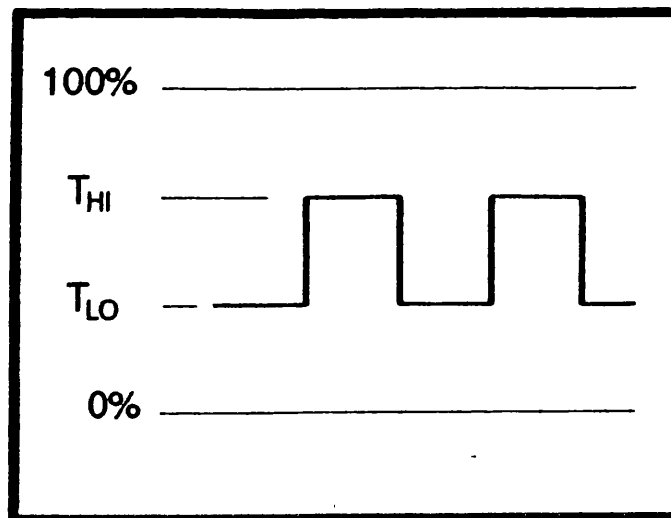


Figure 1.3.1 Definitions for binary signal modulation.

In a simple communication system, the single parameter that best describe optimum modulation is often the transmission change ($T_{hi}-T_{lo}$), as this is directly proportional to the modulated signal. For a reflection modulators we use reflection change.

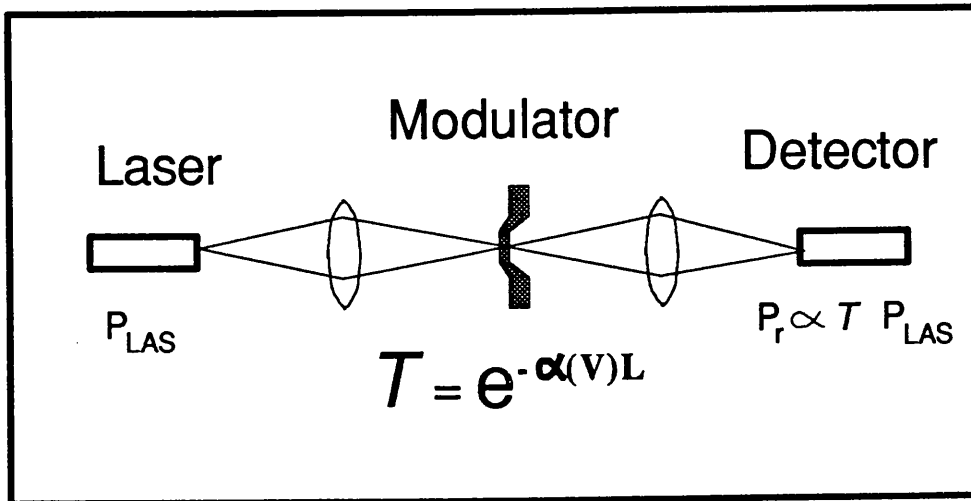


Figure 1.3.2 Simple communication link with MQW diode modulating light for a laser source with signal being detected in a photodetector.

To illustrate this point consider the simple system shown in figure 1.3.2 where laser light is incident on a modulator, and then passed to a simple p-i-n photodetector. The photocurrent generated in the photodetector for transmission T through the modulator is:

$$i_s = \eta_{s-m} \eta_{m-r} P_{las} T \frac{\eta_{ph} e \lambda}{hc} \quad (1.3.1)$$

where P_{las} is the laser light output, η_{ph} the quantum efficiency of the detector, η_{s-m} and η_{m-r} are the optical imaging losses from laser to modulator and modulator to receiver, λ the wavelength, h is Planck's constant, c is the speed of light.

The 'AC' coupled signal is then

$$i_{s,ac} = \eta_{s-m} \eta_{m-r} P_{las} \Delta T \frac{\eta_{ph} e \lambda}{hc} \quad (1.3.2)$$

where ΔT is the transmission change

$$\Delta T = T_{hi} - T_{lo} \quad (1.3.3)$$

If the receiver noise is dominated by thermal noise which is the same for the on and off state [Gowar], then the signal to noise ratio is

$$K_{s-n} = \eta_{s-m} \eta_{m-r} P_{las} \Delta T \frac{\eta_{ph} e \lambda}{hc} \frac{\sqrt{R}}{\sqrt{(4kTB_w)}} \quad (1.3.4)$$

where R is the receiver input resistance, k is Boltzmann's constant, T is the temperature and B_w is the receiver bandwidth.

The transmission change therefore determines the signal to noise at the receiver. This is supported by the experimental results of Delavaux et al. who have measured the dependence of the receiver bit error rate for changing contrast ratios of a LiNbO_3 modulator with a PINFET receiver. They analyse their results in terms of a power penalty in the receiver caused by the low contrast ratios and this can be well fitted by

$$\text{Power penalty} = \Delta T / T_{hi} \quad (1.3.5)$$

As one might expect, when the signal high state power is multiplied by the power penalty, the result is proportional to the transmission change, hence supporting the use of ΔT as a figure of merit.

The above calculation is only fully valid for a receiver dominated by thermal noise as is typical for a p-i-n detector. Avalanche photodiode (APD) receivers will generally be operated in regime where shot noise becomes significant and hence the noise becomes dependent upon the optical power received. The effect of low contrast upon the operation of an avalanche photodetector has been considered by McDonald et al. who show that the further power penalty, resulting from using a APD as opposed to a p-i-n, is an order of magnitude smaller than the overall one.

ii) *Operating Voltage*

In order to ease the burden of the driver circuitry, the operating voltage should be as low as possible. Ideally the modulator should be directly driven from standard logic levels, and certainly within the supply rails of the electronic circuitry (typically 5 V or 12 V). It will be shown that the operating voltage determines the optimum device thickness and hence the modulator performance.

iii) *Speed/Capacitance*

Liquid crystal and other competing technologies are all of relatively slow speed (except LiNbO₃) compared to the MQW modulator and hence speed is one of the MQW modulator's strongest selling points. The speed of the device is mainly determined by its p-i-n capacitance and hence scales linearly with the modulator area. Boyd et al. [1989] have recently demonstrated operation at 5.5 GHz in a 50 μm diameter device when driven by 50Ω resistance. One should note however that the driven resistance in some instances will not be so low (eg. ≈10 kΩ for minimum size MOSFET), and hence it is important to keep the capacitance as low as possible.

iv) *Operating Wavelength*

This depends upon the material system being used and the well width selected. For GaAs/(GaAl)As it is typically 860 nm.

v) *Optical Bandwidth*

This is generally related to the linewidth of excitonic absorption peak and is typically 5-10 nm. Typical multimoded semiconductor lasers have a spectral width of 3 nm and thus are compatible with the modulator.

vi) *Saturation Power*

One potential problem with the MQW electroabsorption modulators is that the exciton feature being used can be bleached by carriers generated through absorption of the optical power. The density of electron hole pairs generated in a small volume of QW material is:

$$N = I\alpha\tau/E \quad (1.3.6)$$

where I is the intensity, E is the photon energy (1.45 eV), α is the absorption (10000 cm⁻¹), τ is the carrier lifetime.

We estimate saturation occurs when the density of the electron-hole pairs exceeds the density of excitons ($1/\pi L_w R_{ex}^2$, where L_w is the well width (100 Å) and R_{ex} is the exciton radius (70 Å)) [Chemla et al., 1984]. Thus the saturation intensity is

$$I_s = E/2\alpha\tau L_w \pi R_{ex}^2 \quad (1.3.7)$$

The lifetime in the p-i-n is short, especially when a bias is applied,

because the electric field enhances tunnelling out of the wells [Larsson et al., 1988]. Larsson et al. [1985] measured photocurrent response times of less than 100 ps. Using this above value we calculate a saturation intensity of 75 kWcm^{-2} , or 75 mW for a $10 \times 10 \mu\text{m}$ spot size. Boyd et al. [1989] have recently measured saturation intensities for the same spot size of 3 mW in a high speed reflection modulator. This low value is still unexplained, but it might be related to space charge effects in which the photogenerated carriers tend to screen out the electric field. The topic of carrier escape from quantum wells is one of intense contemporary interest and is likely to provide ways of obtaining operating intensities close to those predicted above.

vii) *Temperature Tolerance*

The bandedge of MQW material shifts with temperature and hence the optimum modulation wavelength changes. We can define two different figures to describe the temperature tolerance of the modulator. If the source wavelength is fixed, changes of the order of 10 K will have shifted the exciton a significant distance away and the modulation will decrease. This is called the fixed wavelength temperature variation (FWTV). On the other hand if one is able to tune the source wavelength to that of optimum modulation, a greater temperature variation can be tolerated. This is the scanning wavelength temperature variation (SWTV). Although experimental measurements are still to be made it is predicted that the SWTV of an AFPM is smaller than for a non-resonant device because not only does the absorption edge shift, but changes in the cavity refractive index cause a shift of the resonant wavelength. The temperature tolerance of modulators will be discussed in more detail in chapter 6, where the implications for use of the modulator in an optical interconnect are presented.

viii) *Angular Tolerance*

A change in modulation with incident angle for a non-resonant modulator can arise from : i) the increased optical path length can actually increase modulation, and ii), in a very small transmission modulator, the modulator width can be smaller than the substrate thickness and light can be deflected by the edges of the etched hole in the substrate if the modulator. Resonant modulators however are more sensitive,

since a change of incident angle also changes the resonant wavelength. At normal incidence the sensitivity to angle is rather small and a tolerance of up to 20° is predicted. Off normal resonance the sensitivity is much greater, and at 45° the permitted range is only $\pm 5\%$. More details can be found in chapter 6.

1.4 Published Modulation Results

There are now a large number of published experimental results for electroabsorption modulators. Modulation data for normal incidence devices are listed in table 1.4.1. These figures should be treated with some caution since the insertion losses will tend to vary with the experimental arrangement. Many of the non-resonant devices have at least one uncoated surface and hence suffer from reflection losses of about 1.5 dB at each interface. Furthermore, even in intentionally non-resonant devices, imperfect anti-reflection coatings can cause Fabry-Perot effects to be visible in the spectrum which can change the modulation by up to 10%.

The GaAs non-resonant transmission devices show typical operating voltages of 5-10 V, contrasts of 3 dB, and transmission changes of 30-40%. The results of Whitehead et al. [1988b] indicate the influence of well width upon the modulation. Thin wells give the best transmission change, but require large voltages, and tend to work in the bias-absorbing mode. Thicker wells operate at low voltages, and normally in a bias-transmitting mode. Hsu et al. achieve a contrast of 10 in the *bias-transmitting* mode by making a much thicker device. Unfortunately, along with the 10 dB contrast they get a 13 dB insertion loss and require an operating voltage of 20 V.

We can compare the MQW results with those of Wight et al. for bulk GaAs modulators utilising the Franz-Keldysh effect. Because the changes of absorption are much smaller in these materials, the insertion loss is generally high (8.2 dB) and the modulation limited (1.1 dB).

Reflection modulators using built-in dielectric stacks were first presented by Boyd et al., and the doubling of the optical interaction length doubles the achievable contrast. Much higher contrasts again are possible using AFPMs, with insertion losses as low as 3 dB. (GaIn)As quantum wells have lower absorption coefficients, and require a thicker intrinsic region and operate at a higher voltage.

Group	Well Width Å	Number of wells	Contrast Ratio dB	Insertion Loss dB	Transmission Change %	Volts V	Speed ps
GaAs Transmission							
<i>Wood et al., 1984</i>	95	50	2.83	1.87	-35	8	
<i>Wood et al., 1985a</i>	95	50	2.19	1.19	-32	9	<131
<i>Whitehead et al., 1988b</i>	47	75	2.8	1.8	-36	20	
<i>Whitehead et al., 1988b</i>	87	60	3.4	3.1	-27	12	
<i>Whitehead et al., 1988b</i>	147	45	2.5	2.67	24	12	
<i>Hsu et al., 1988a</i>	100	200	10	13	5	20	
Bulk GaAs Transmission							
<i>Wight et al., 1985</i>			1.1	8.2	3.5	5	
Non-resonant Reflection							
<i>Boyd et al., 1987</i>	97	65	9.0	6.0	-22	18	29
AFPM							
<i>Whitehead et al. 1989c</i>	95	75	20	3.5	-42.6	9	
AFPM on Silicon							
<i>Barnes et al., 1989</i>	120	75	1.45	2.22	-17	8	
(GaIn)As Transmission							
<i>Koren et al., 1987a</i>	100	100	0.97	4.56	-7	20	30
<i>Wakita et al., 1985</i>	75	60	0.93	?	?	20	
<i>Guy et al., 1989</i>	100	150	2.4	2.8	-40	40	

Table 1.4.1 Performance of normal incidence electro-absorption modulators.

Waveguide results are presented in table 1.4.2. In waveguides the coupling losses are often large and will vary depending on the optics used. The longer, unconstrained, interaction length possible in a waveguide makes very high contrasts possible, independent of whether the material is GaAs or (GaIn)As or even bulk material [Noda,Y. et al].

In this section we have concentrated upon the use of MQW diodes as modulators, although we have already mentioned that they make good photodetectors as well. The response time of the device as a detector is bias-dependent and has been investigated by Larsson et al. [1985]. Response times of typically 100 ps were observed indicating that very high speed operation is also possible as a photodetector.

Group	Well Width Å	Number of wells	Contrast Ratio dB	Insertion Loss dB	Transmission Difference %	Volts V	Speed ps
GaAs Waveguide							
<i>Wood et al., 1985b</i>	97	2	10	7.21	-17	15	97
<i>Tarucha et al., 1985</i>	18	16	3.01	?	?	1.4	350
(GaIn)As Waveguide							
<i>Wakita et al., 1987a</i>	67	10	8.86	13	-13	1.8	
<i>Wakita et al., 1987a</i>	67	40	15	12	-6.1	9	160
<i>Koren et al., 1987b</i>	80	80	18.7	2.7	-50	20	53
Bulk (GaIn)As Waveguide							
<i>Noda, Y., et al., 1986</i>			23	9.6	-10.9	11	41
Strained Layer (GaIn)As/GaAs							
<i>Das et al., 1987</i>	100	64	1.21	0.91	-20	9	150
GaAs Coupled Wells							
<i>Islam et al., 1988</i>	47.5	4	11.4	?	?	3.5	

Table 1.4.2 Performance of waveguide electro-absorption modulators. Negative values of transmission change are for bias-absorbing modes.

1.5 Summary

In this chapter we have described the MQW electroabsorption modulator and its operation. It can be manufactured in a number of different material systems, but GaAs/(GaAl)As is much the most developed and understood. We have then defined and estimated what are the device's most important properties. In describing the modulation we have introduced the use of transmission change to describe the modulation, especially in simple communication links where it reflects the 'AC' modulation on the light signal. Finally we have made a survey of data from published devices. From this collected data, we find that non-resonant transverse devices operating at low voltages and low insertion losses have limited contrasts and waveguide devices offer high contrasts, but with associated difficulties of coupling into the guide. On the other hand the recently proposed and demonstrated AFPM seems to offer high contrast, low insertion loss operation at reasonable voltages.

Chapter 2

CALCULATION OF FIELD DEPENDENT ABSORPTION

2.1 Introduction

As described in the preceding chapter, the quantum well electroabsorption modulator utilises the large changes of absorption on the application of an electric field perpendicular to the wells. The first step in optimising the device must therefore be the understanding and modelling of this basic electroabsorption effect.

The dominant features at the band edge are transitions between the conduction and valence $n=1$ subbands and their associated excitons. Miller, D.A.B. et al. [1985] was the first to consider the changes in absorption arising from the application of an electric field. In the direction parallel to the wells, it was found that the exciton broadened rapidly due to ionisation in the applied electric field. However, a qualitatively different effect is seen for a perpendicular field where the barriers prevent field ionisation. The excitons therefore remain resolved at high fields and a clear Stark shift to lower energy is seen. Accompanying this shift one also gets a reduction in oscillator strength and additional inhomogeneous broadening. The shift has been modelled by many authors [Miller, D.A.B. et al. 1985, Fernandez and Castro, Bastard et al., Austin and Jaros, Matsuura and Kamizato, Singh and Hong, Harwit et al.] and named the Quantum Confined Stark Effect (QCSE). The reduction in the exciton's oscillator strength has been successfully related to the overlap integral between the electron and the hole wavefunctions [Miller, D.A.B. et al. 1986]. A number of broadening mechanisms in a practical modulator have been proposed : lifetime broadening due to tunnelling through the barriers and phonon interaction , inhomogeneous broadening caused by well width fluctuation [Juang et al.] and electric field variations from well to well due to background doping in the intrinsic region [Newson and Kurobe].

Several authors had used calculations of the subband energies to evaluate a theoretical absorption spectrum [Sanders and Bajaj, Klipstein and Apsley, Ikonic et al.], but to my knowledge no one has previously included both the loss in oscillator strength and the effects of the inhomogeneous broadening mechanisms described above, and made comparisons with experimental data.

In this chapter we develop such a model for GaAs/(GaAl)As material.

2.2 Evaluation of Subband Energies

Multiple quantum well material has, by definition, barriers of such a width that coupling between wells is unimportant so that the electronic states of the material are characterised by those of the single well. A relatively simple theory to describe the electronic states of a quantum well has been developed in the last few years. This theory is based on the envelope approximation in which the wavefunction is split into the Bloch states and an envelope function that spatially modulates the Bloch states [Bastard and Brum]. Once the band edges and the effective masses describing the Bloch states of the component materials have been determined, the envelope function is relatively easily calculated as a result of the simplicity of geometry of the well structure.

It is found that the component of electron momentum perpendicular to the wells is quantised and as a result the valence and conduction bands are split into a series of subbands. Within each subband the electrons are only free in two dimensions and this restriction causes the density of states function to have a step-like shape at the band edge. The quantum confinement also lifts the degeneracy of the valence band and leads to the observation of two sets of subband transitions, namely the heavy and the light hole.

The edges of the subbands described above are equal to the energy levels in the one dimensional well defined by the alignment of the band-edges in the two component materials. In a perpendicular electric field, these wells tilt and the energy level changes with respect to the centre of the well. This change is the origin of the QCSE. The shift has been modelled perturbatively [Fernandez and Castro], using variational methods [Bastard et al.], using exact Airy function solutions [Austin and Jaros, Matsuura and Kamizato], and by Monte Carlo [Singh and Hong] and tunnelling resonance methods [Miller, D.A.B. et al 1985, Harwit et al.].

We have used the tunnelling resonance technique, in which the energy levels are evaluated by searching for resonances in transmission through a double barrier structure. The structure of the barrier used is shown in figure 2.2.1 where the sloping portions are split up into a large number of steps. This model has been chosen for the following reasons: i) the solution within each step is the sum of two simple exponentials (with either real or imaginary arguments) as opposed to more complex Airy functions for the

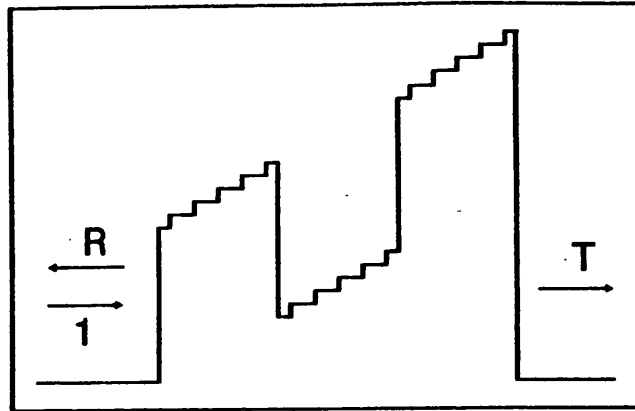


Figure 2.2.1 Resonant tunnelling barrier used to determine energy levels in a finite potential well in an electric field. Typically 20 steps are used in each layer.

continuously sloping potentials; ii) the tunnelling through the finite barriers is also modelled; iii) the non-parabolicity of the bands can be taken into account when calculating the wavenumber in each step; iv) the electron-hole overlap integral can be easily calculated from the values of the wavefunction evaluated in each step.

Within each step the envelope-function is assumed to be the combination of a forward and a reverse travelling wave or their evanescent equivalents:

$$f(z) = A \exp(ikz) + B \exp(-ikz) \quad (2.2.1)$$

where f is the envelope-function, A and B arbitrary constants and k the wavenumber. The wavenumber is

$$k = 2\pi[2m_{\perp}^*(E - V(z))]^{1/2}/h \quad (2.2.2)$$

where E is the particle energy, h is Planck's constant, V , the potential and m_{\perp}^* the effective mass perpendicular to the wells.

Two easily applicable methods have been proposed to account for nonparabolic bands by Hiroshima and Lang and Nelson et al. [1987a]. The energy dependent effective mass approach [Hiroshima and Lang] has been

chosen since it includes the nonparabolicity of the barrier material and the effects of nonparabolicity on the boundary conditions at the interface. The energy dependent effective masses used for the electron and the light hole are given by

$$m_{\perp}^*(E) = m_{\perp}^* [1 + (E - V(z)) / E_{np}] \quad (2.2.3)$$

$$\text{where } E_{np} = \hbar^2 / 8\pi^2 m_{\perp}^* \gamma \quad (2.2.4)$$

where γ is the band nonparabolicity. The calculation of the transmission coefficient is made by using a transfer matrix to evaluate the wavefunction throughout the structure. The mathematics is exactly the same as that used to calculate the optical transmission through a series of dielectric layers of differing refractive indices [Born and Wolf]. At any interface the value of the envelope wavefunction itself (f) and $(1/m^*)\partial f/\partial z$ are conserved [Bastard and Brum]. A transfer matrix is then used to relate the values of the f and $(1/m^*)\partial f/\partial z$ on either side of a potential step:

$$\begin{pmatrix} f \\ (1/m_{\perp}^*) \partial f / \partial z \end{pmatrix}_{z=z_0 + \Delta z} = \begin{pmatrix} \cos(k\Delta z) & (m_{\perp}^*/k) \sin(k\Delta z) \\ (k/m_{\perp}^*) \sin(k\Delta z) & \cos(k\Delta z) \end{pmatrix} \begin{pmatrix} f \\ (1/m_{\perp}^*) \partial f / \partial z \end{pmatrix}_{z=z_0} \quad (2.2.5)$$

where Δz is the width of the step.

A single transmitted wave can be set up to the right of figure 2.2.1, and the envelope-function can then be evaluated from the right to the left of figure 2.2.1. The energy of the particle is then varied until a resonance is found in the transmission corresponding to the energy level in the well. For an electron in a well of 100 Å at a field of 100 kV/cm, 20 steps within the well (step height of 5 meV) were enough to give an accuracy in the energy level of 0.005 meV. Excellent agreement with the calculations of the heavy hole level given by Miller, D.A.B. et al. [1985] is found when the same effective masses and band offset ratios are used. There is also agreement to within 2 meV with similar calculations that use the exact Airy functions and this is most likely to be caused by a small error when calculating the Airy function at that time. Figure 2.2.2 show the calculated $n=1$ electron and heavy and light hole subband energies for a 100 Å well for 30% aluminium barriers. Note that the heaviest particle, the heavy hole, shifts the most. The

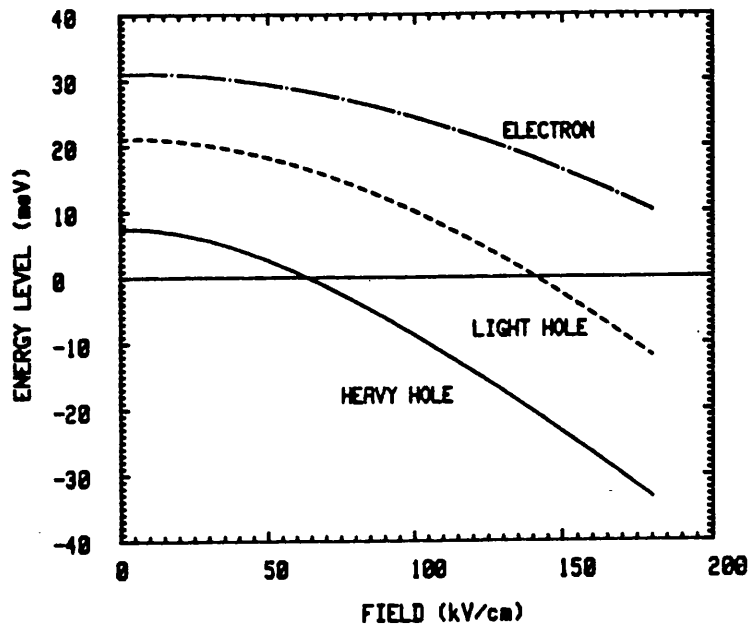


Figure 2.2.2 Energy level of the $n=1$ electron, heavy and light hole subbands as a function of electric field. The well width is 100 \AA and the barriers are of 30 % aluminium.

band non-parabolicity is found to have a minor effect of the zero-field subband energy, but very little difference is seen in the shift. Negative subband energies are possible at high fields because the energy level is measured with respect to the potential of the middle of the well, significantly above the bottom corner of the well when the electric field is applied.

Before calculating the transition energies between conduction and valence subbands, one more item must be addressed: the effect of stress in the well material. Miller, D.A.B. et al. [1985] suggest that the difference in lattice constant for the GaAs (5.6533 \AA) and the (GaAl)As (5.6564 \AA) gives rise to a strain in the sample that shifts the light hole subbands. One might expect the larger bulk of the GaAs substrate to determine the lattice constant in the wells and since the wells are also GaAs there should be no strain shift. However there is evidence that during growth, the formation of lattice interface dislocations relieves the strain in the (GaAl)As buffer and barrier regions, at the same time introducing it into the GaAs wells [Dingle and Wiegmann]. We find that a consistent split between the light and heavy

hole excitons (sample I) when we assume a stress of 47 MN/m^2 present in the GaAs, a value suggesting the stress is equally shared between well and barrier material. This causes shifts of -0.25 and 3.2 meV for the heavy and light holes respectively.

The subband gap for both the heavy and light hole subbands is the sum of the bulk well material band gap (E_g), the m^{th} electron (E_c^m) and the n^{th} hole (E_v^n) subband levels, and the strain shift (E_{strn}):

$$E_{\text{cv}}^{m,n}(F) = E_g + E_c^m(F) + E_v^n(F) - E_{\text{strn}} \quad (2.2.6)$$

where F is the electric field.

The effective masses [Miller,R.C. et al.], bandgaps [Casey and Parish], band offset ratios [Duggan et al.] and nonparabolicity parameters [Nelson et al., 1987a] used for the GaAs/(GaAl)As are shown in table 2.2.1.

Parameter	Value
Electron mass (m_0)	$0.0667 + 0.0835x$
Heavy Hole Mass (m_0)	$0.34 + 0.412x$
Light Hole Mass (m_0)	$0.094 + 0.066x$
Bandgap (eV)	$1.4247 + 1.247x$
Band Offset Ratio (%)	65
Electron Nonparabolicity (m^2)	4.9×10^{-19}
Light Hole Nonparabolicity (m^2)	7.35×10^{-19}

Table 2.2.1 List of parameters of (GaAl)As used in the calculations of the subband energies of MQWs. The assumed temperature is 295 K and X is the aluminium mole fraction.

The tunnelling resonance technique also provides values of the wavefunction through the well and the surrounding barriers. Numerical integration can then be used to calculate the electron-hole overlap integral:

$$M_{\text{cv}}^{m,n} = \left| \int f_c^m(z) f_v^n(z)^* dz \right| \quad (2.2.7)$$

where f_c^m and f_v^n are the m^{th} conduction and n^{th} valence subband envelope wavefunctions respectively.

The wavefunctions used are truncated at the first minima reached in the

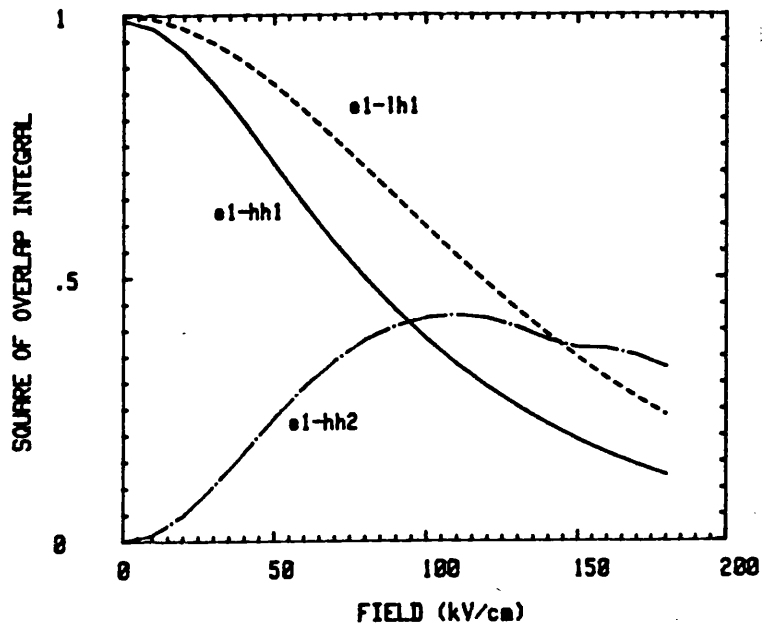


Figure 2.2.3 The square of the overlap integral between the electron and hole wavefunctions as a function of perpendicular electric field. The calculation is for 100 Å wells and 60 Å barriers and a barrier aluminium concentration of 30%.

barriers. The oscillator strength is proportional to the square of the overlap integral [Miller, D.A.B. et al. 1986]. Figure 2.2.3 plots the square of the overlap integral as a function of electric field for the $n=1$ heavy hole to $m=1$ electron (e1-hh1), $n=1$ light hole to $m=1$ electron (e1-lh1) and $n=2$ heavy hole to $m=1$ electron (e1-hh2) transitions. The wavefunctions for transitions with differing subband numbers, are almost orthogonal to one another at zero field and are called forbidden transitions because of the small initial overlap. On the application of an electric field the initially allowed transitions' oscillator strengths subside, whereas the forbidden transitions grow. This is clearly seen in figure 2.2.3 where the e1-hh1 and e1-lh1 transition subside and the e1-hh2 transition grows.

The width of the tunnelling resonance is related to the tunnelling through the barriers by the Heisenberg uncertainty principle. The linewidth of the electron, heavy and light hole are shown in figure 2.2.4 and it can be seen that up to 150 kV/cm they do not exceed 1 meV.

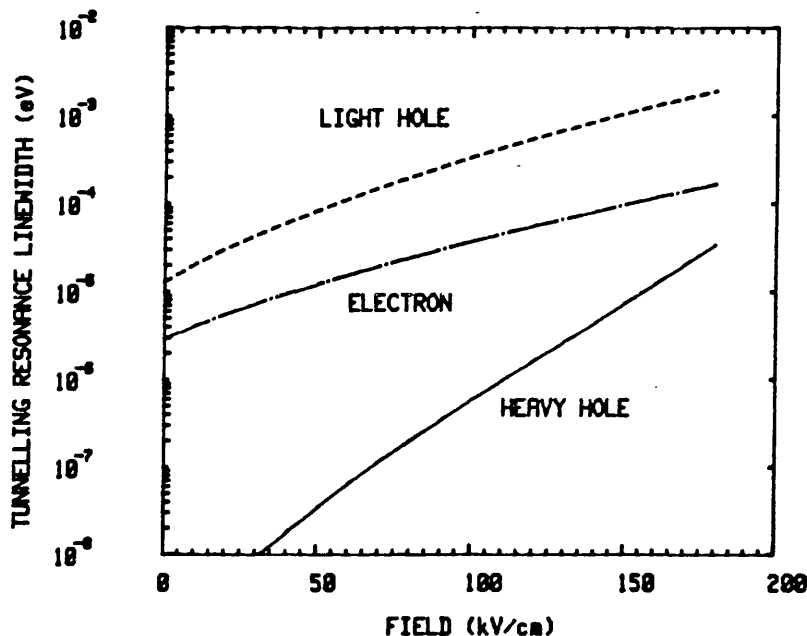


Figure 2.2.4 The variation of the tunnelling resonance linewidth with electric field for electron (middle), and light (upper) and heavy hole (lower) $n=1$ levels. The calculation is for 100 Å wells and 60 Å barriers and a barrier aluminium concentration of 30%.

2.3 Determination of Well Widths

An assessment of the well widths of quantum well devices is a natural prerequisite for modelling their physical characteristics since the Stark shift is sensitively dependent upon it.

The thickness of the layers in an epitaxially grown sample cannot be predicted accurately in advance because of uncertainty in the growth rates. Hence some form of characterisation is required after growth, either by photoluminescence (PL), photoluminescence excitation (PLE), x-ray

diffraction (XRD) or transmission electron microscopy (TEM). Of these PLE and XRD are the most reliable and good agreement between the various methods has been found [Orton et al.]. However, there is still a possibility that the growth rates over the wafer can vary, and hence the assessment of the well width of a particular device is best derived from measurements taken on that device.

Fortunately, the presence of well defined exciton transitions in the absorption spectra allows us to do just that. We have already mentioned these exciton transitions as being states created with photon energies just below the subband separation energy and arising from the mutual attraction between the excited electron and hole. The transition energy is given by

$$E_{\text{ex}} = E_{\text{cv}}^{m,n} - E_b \quad (2.3.1)$$

where E_b is the binding energy. Calculation of the binding energy of a quantum well exciton was first done by Greene et al., and subsequently by many authors [Miller, D.A.B. et al. 1985, Ekenberg and Altarelli, Nelson et al., 1987b]. The well width dependence of the binding energy is important and for our calculations we use the results of Ekenberg and Altarelli with the following fit (in meV):

$$E_b^{\text{hh}} = 14.2 - 0.0705 L_w + 1.75 \times 10^{-4} L_w^2 \quad (2.3.2)$$

$$E_b^{\text{lh}} = 16.1 - 0.061 L_w + 10^{-4} L_w^2 \quad (2.3.3)$$

where L_w is the well width. We neglect the small variation of E_b with barrier aluminium concentration.

Figure 2.3.1 shows the variation of the excitonic peak as a function of the QW thickness. The estimates obtained from this graph have been found to be reliable and have been used in recalibrating the MOCVD growth kit at Sheffield University which had earlier routinely produced well thicknesses less than those specified.

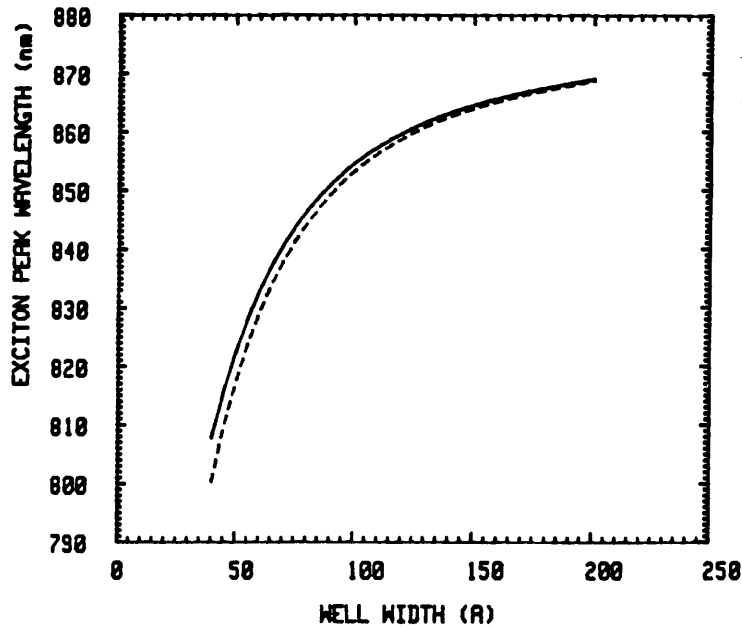


Figure 2.3.1 Exciton wavelength for e1-hh1 transition against well width, for barrier aluminium concentrations of 30 % (solid) and 40 % (dashed). The temperature is 297 K.

2.4 Calculation of Absorption Spectra

Calculations of the absorption spectra near to the band edge have been published by several authors: an empirical model using two Gaussians for the heavy and light hole excitons and a single continuum has been proposed by Chemla et al. [1984] and several models derived from more fundamental calculations of the band structure [Sanders and Bajaj, Klipstein and Apsley, Ikonic et al.]. However none of them model the field dependent broadening mechanisms necessary to give good agreement with experimental results.

In order to calculate the absorption spectrum of quantum well material a similar approach to that of Elliot's for bulk material, is taken and one assumes that two fundamentally different transitions contribute to the absorption of photons. First there is a continuum of transitions, at energies greater than the subband separation, $E_{cv}^{m,n}$, between free particle states in the various conduction and valence subbands. Secondly there are

transitions to excitonic states just below the subband gap energy.

The unbroadened contribution from each pair of subbands can be written as the sum of a delta function to describe the exciton and a step function, multiplied by the Sommerfeld factor for the continuum:

$$\alpha_{hh/lh}^{m,n} = \alpha_{\infty} M_{cv}^{m,n}{}^2(F) \{ f_{ex} \delta[E - E_{cv}^{m,n}(F) + E_b] + H[E - E_{cv}^{m,n}(F)] S[E, E_{cv}^{m,n}(F)] \} \quad (2.4.1)$$

where E is the photon energy, F the electric field, α_{∞} the absorption of the continuum, $M_{cv}^{m,n}$ the overlap integral between the electron and hole wavefunctions, f_{ex} the relative strength of the exciton to the continuum, $\delta[E]$ the Dirac delta function which describes the unbroadened exciton, $E_{cv}^{m,n}$ the field-dependent separation between the $n=1$ electron and hole subbands, E_b the exciton binding energy, $H[E]$ the Heaviside step function and $S[E, E_{cv}]$ the Sommerfeld factor.

Equation (2.4.1) is similar to that used by Klipstein and Apsley. The heavy and light hole states are uncoupled and only a single 1S exciton state is included. Dawson et al. [1986] have observed a 2S exciton state, but only with a good sample at low temperatures using PLE. Theory predicts that its strength is 1/27 of that of the 1S state, and both it and higher states can be included in the calculation. The following other features are added that make our calculation different from that of Klipstein and Apsley : the oscillator strengths for the two transitions considered are proportional to the square of the overlap integral between the electron and the hole envelope functions, a Sommerfeld factor is included in the shape of the continuum, and further inhomogeneous broadening is accounted for by successive convolution with the appropriate lineshape.

The Sommerfeld factor is an enhancement of the free particle subband absorption around the band edge because of the Coulomb attraction between the electron and hole, and for a two-dimensional exciton it was first calculated by Shinada and Sugano and is given by

$$S[E, E_{cv}^{m,n}] = \frac{2}{1 + \exp[-2\pi R_y^{1/2} / (E - E_{cv}^{m,n})^{1/2}]} \quad (2.4.2)$$

where R_y is the Rydberg constant:

$$R_y = \frac{e^4 \mu}{8\epsilon^2 h^2} \quad (2.4.3)$$

with μ the reduced mass of the exciton:

$$\mu = \frac{m_{\parallel c}^* m_{\parallel v}^*}{m_{\parallel c}^* + m_{\parallel v}^*} \quad (2.4.4)$$

and e is the electronic charge, ϵ the permittivity of MQW material which is assumed to be midway between those of the well and barrier material and $m_{\parallel c}^*$ and $m_{\parallel v}^*$ are the effective masses of the electron and hole parallel to the plane of the well. The heavy and light hole masses differ from their values in the perpendicular direction and are given by [Chemla and Miller, 1987]:

$$m_{\parallel hh}^* = \frac{4m_{\perp hh}^* m_{\perp lh}^*}{3m_{\perp hh}^* + m_{\perp lh}^*} \quad (2.4.5)$$

$$m_{\parallel lh}^* = \frac{4m_{\perp hh}^* m_{\perp lh}^*}{m_{\perp hh}^* + 3m_{\perp lh}^*} \quad (2.4.6)$$

The relative oscillator strengths for the heavy and light hole transitions depend upon the polarisation of the light. When the light is propagating perpendicular to the well, the electric field vector is always directed in plane of the QW. On the other hand when the light is propagating parallel to the QWs, the electric field can either be parallel or perpendicular to the QWs, ie. the transverse electric (TE) and transverse magnetic (TM) modes. The combination of states excited in the quantum well depends upon the direction of electric field. In the TM mode the heavy hole is completely suppressed at the band edge whereas in the TE mode the ratio between the oscillator strengths for the heavy and light hole contribution is 3 to 1 [Asada et al., Yamanishi and Suemune] and hence the absorption coefficient for the structure as a whole is given by

$$\alpha_{qw} = \sum_m \sum_n \alpha_{hh}^{m,n} + (1/3) \sum_m \sum_n \alpha_{lh}^{m,n} \quad (2.4.7)$$

We use this definition of absorption in our plotted spectra since it is

independent of the barrier thickness. The absorption coefficient for the composite material is given by

$$\alpha = [L_w / (L_b + L_w)] \alpha_{qw} \quad (2.4.8)$$

where L_w and L_b are the well and barrier widths respectively.

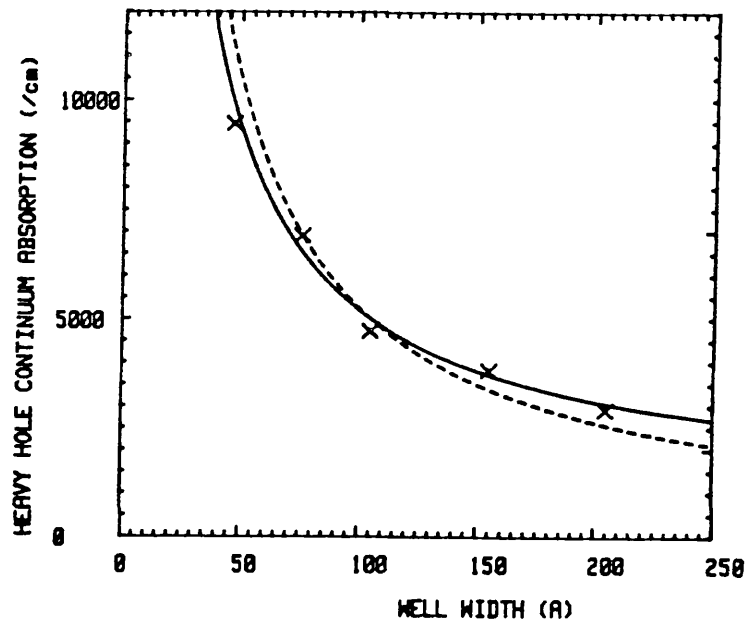


Figure 2.4.1 Values of heavy hole continuum (α_∞) derived from experimental spectra with empirical fit (solid) to the data. The dotted line is a $1/L_w$.

We define α_∞ as the absorption in the heavy hole continuum. Note that to relate it to the continuum absorption measured at wavelengths just shorter than the light hole exciton, one needs to multiply by $4/3$ to include the light hole contribution and then by $1.8-1.9$ for the Sommerfeld factor. In order to achieve the most realistic results from the modelling we have derived α_∞ from experimental results over a range of well widths. This was done by curve fitting from spectra supplied by Jelley et al., and the result can be seen in figure 2.4.1. An empirical fit to the data is given by

$$\alpha_\infty = 1000 + 4.2 \times 10^5 / L_w \quad (2.4.9)$$

Also plotted in figure 2.4.1 in the dotted line is the inversely proportional relationship, equivalent to a constant absorption per well. This is predicted by simple theory [Matsumoto et al.].

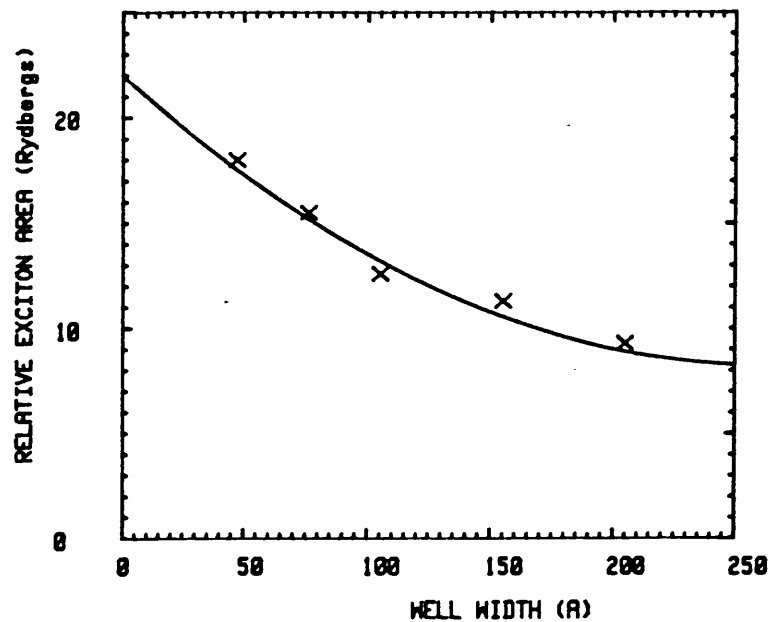


Figure 2.4.2 Values of relative exciton area (f_{ex}) derived from experimental spectra with empirical fit to the data.

In addition to the continuum level we also derive the relative exciton area (f_{ex}) from experimental spectra. Note that by area we mean the area under the absorption spectra, not the exciton's spatial extent. It is convenient to define f_{ex} in terms of the Rydberg constant since theoretical calculations predict $f_{ex} = 16 R_y$ for a 2D exciton [Shinada and Sugano, Chemla et al., 1985]. In figure 2.4.2 we plot the experimentally-derived results with the following empirical fit:

$$f_{ex} = 22 - 0.105L_w + 2 \times 10^{-4} L_w^2 \quad (2.4.10)$$

As the well width increases the quantum well exciton loses its 2D character and f_{ex} decreases. The high value the fit gives for thin wells might be the result of inaccuracy in the Sommerfeld factor. Chan has made more extensive numerical calculations for the Sommerfeld factor in a quantum well (not purely 2D) and show that it really lies between the two and three

dimensional case. However, since the Sommerfeld factor tails off slowly with increasing energy, provided one is only interested in photon energies around the band edge, it can be regarded as almost constant and the resultant lower f_{ex} is cancelled by a higher α_{ex} .

Under the application of an electric field we assume that both the relative area and the binding energy of the exciton remains constant. Thus the exciton decays with the continuum, dependent upon the electron-hole wavefunction overlap. This assumes that the lateral extent of the exciton does not change, although in practice it is likely to increase slightly as a result of the increased separation of the electron and hole. As for the binding energy, a variational calculation by Miller, D.A.B. et al. [1985] has estimated that there is a drop in binding energy of about 2.5 meV for a well of 95 Å in a field of 120 kV/cm, which is an order of magnitude lower than the overall shift of 25 meV. Two other authors [Sanders and Bajaj, Brum and Bastard] have performed similar calculations and observe a similar reduction although they do not show results at high fields.

2.5 Broadening Mechanisms

Expression (2.4.1) includes delta- and step-functions which are not practically realisable. This is because broadening of the spectra take place through a number of mechanisms which are accounted for by successive convolution with the appropriate lineshape.

i) Phonon Broadening

Any exciton created by the absorption of a photon has a finite lifetime, which will cause a broadening in the transition energy through Heisenberg's uncertainty principle. Possible mechanisms for the destruction of an exciton are recombination, tunnelling of either the electron or hole through the barrier, and phonon interaction. Chemla and Miller [1985] have shown that it takes only 300 fs for excitons to be ionised by phonons at room temperature, much shorter than the nanosecond timescale over which recombination takes place [Dawson et al.,1985, Matsusue and Sakaki]. The tunnelling rate through the barriers is dependent upon the composition and width of the barriers and can be calculated from the width of the tunnelling resonance found when calculating the subband energy. As shown in figure 2.2.4, with 60 Å barriers of 30 % aluminium concentration, at all fields of interest this broadening is less than 1 meV and can be neglected. Thus, phonon broadening is generally the dominant homogeneous broadening mechanism.

Chemla et al. [1984] have proposed that the temperature dependence of the phonon broadening is proportional to density of LO phonons, described by the Bose-Einstein distribution:

$$\Gamma_T = \frac{\Gamma_{ph}}{[\exp(h\Omega_{LO}/kT)-1]} \quad (2.5.1)$$

where Γ_T is the full width half maximum (FWHM) linewidth, k is Boltzmann's constant, T is the temperature and Ω_{LO} is the LO phonon energy (37 meV).

Γ_{ph} can be estimated from measurements of the temperature dependent exciton linewidth. At low temperatures phonon broadening can be neglected and broadening is caused by the inhomogeneous mechanisms of well width fluctuation and field variation due to background doping. Figure 2.5.1 plots linewidth measurements of a 98 Å well width device

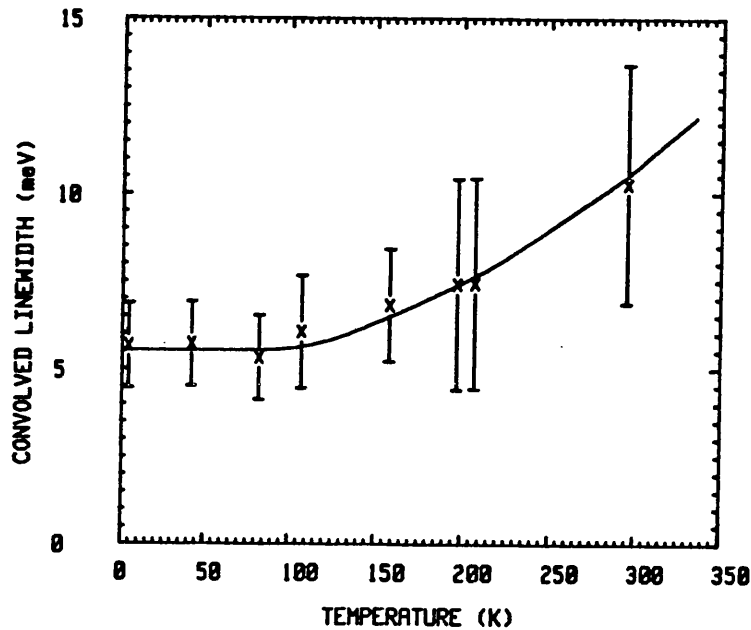


Figure 2.5.1 Heavy hole exciton linewidth measured from photocurrent data over a range of temperature. Fitted line is calculated by convolution of a Lorentzian to describe the phonon broadening, with Gaussian and square ones for the well width fluctuation and background doping mechanisms respectively. Experimental data was measured by M.Whitehead and P.Dobson on material grown at Philips Research by K. Woodbridge

(sample I) as a function of temperature [Whitehead, Dobson and Woodbridge, unpublished]. The fitted line is obtained by convolution of the low temperature broadening with that of the phonon broadening with $\Gamma_{\text{ph}} = 20.5$ meV. This value is larger than that reported by Chemla et al. [1984] (11 meV) since we have assumed a convolution of different lineshapes rather than a simple addition. It is very close to the independent estimate of 20.7 meV by Chen et al. who use a similar technique.

The rate of phonon scattering is assumed to be independent of applied field. Although we can give no absolute justification for this, the LO phonon energy is much greater than the exciton binding energy and thus any collision between a phonon and an exciton is likely to ionise the exciton [Chemla et al.].

In common with other lifetime-related homogeneous broadening, we assume a Lorentzian lineshape function:

$$L(E, E_{ex}) = \frac{\Gamma_T}{2\pi[(E-E_{ex})^2 + \Gamma_T^2/4]} \quad (2.5.2)$$

The Lorentzian lineshape does tend to have wide tails (related to the steplike impulse response), and its implications will be discussed in section 2.6.

ii) Well Width Fluctuations

The atomic layer spacing of GaAs material is 2.83 Å: a significant fraction of the overall well width. It is therefore nearly impossible to obtain completely flat interfaces between the well and barrier material, and different parts of the well will be of different width. Since the subband energies vary with well width, this variation in well thickness will cause a broadening of the absorption features.

The nature of the broadening due to well width fluctuations is dependent on the structure of the interfaces between the well and the barriers. Three possible cases are illustrated in figure 2.5.2. In figure 2.5.2(a) the spatial extent of the monolayer fluctuations on both interfaces is much larger than the exciton itself and as a result the observed spectra is the superposition of spectra for a few discrete well widths. However the opposite is the case in figure 2.5.2(c), and the exciton "feels" an average well width which is distributed as a random variable. In addition to these cases there is also the possibility of having one interface much smoother than the other so that both a superposition and convolution of the spectra is required [Bimberg et al. 1987a, Bimberg et al. 1987b]. Our model assumes that the monolayer fluctuations occur on a much smaller scale than the exciton diameter and we use a Gaussian line shape to describe the average well width fluctuation over the exciton with an expression for the FWHM linewidth in each subband given by Juang et al.:

$$\Gamma_{gss}^{m,n} = \frac{\partial E_{cv}^{m,n}(F,W)}{\partial W} 2.35 \delta W \quad (2.5.3)$$

where δW is the RMS well width fluctuation, W is a variable describing the average well width in the vicinity of the exciton and F is the electric field. The factor of 2.35 is the ratio between the standard deviation and FWHM

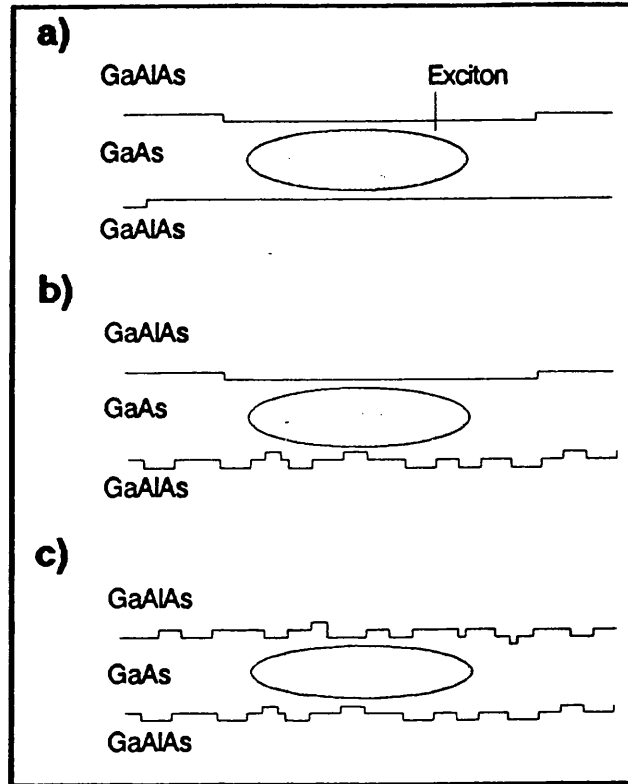


Figure 2.5.2 Three different types of interface structure leading to broadening. In case a), monolayer islands on both interfaces are greater in extent than the exciton. In case b), the exciton width is larger than monolayer islands on one interface, but smaller on the other. In figure c), the monolayer variations are smaller than the exciton at both interfaces.

linewidth of the Gaussian function. The δW takes account of variations in width from well to well in addition to fluctuations within the same well.

The broadening due to well width fluctuation is field dependent. Figure 2.5.3 plots the heavy hole $n=1$ subband energy for two slightly different well widths. The difference in subband energy for the different widths increases with field because the Stark shift is strongly dependent upon the well width.

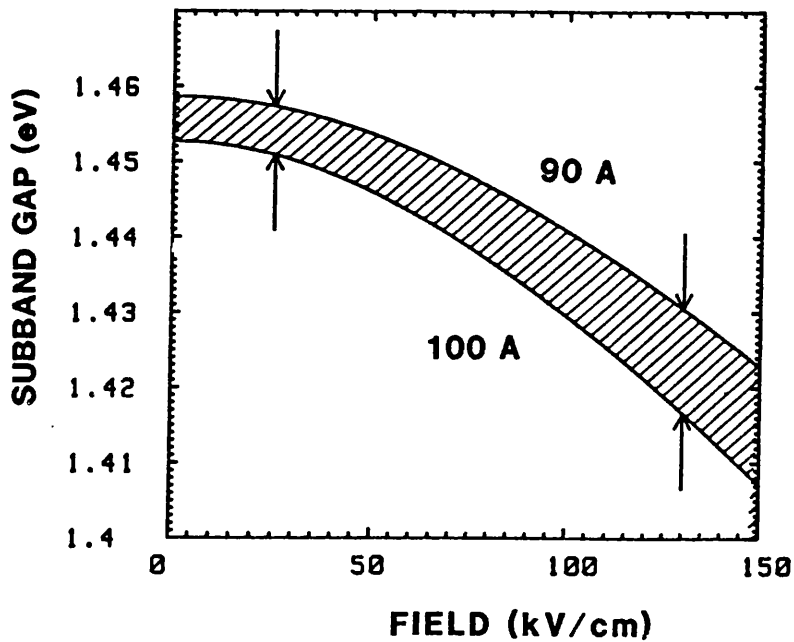


Figure 2.5.3 Graphical representation for the change in broadening caused by well width fluctuation with an applied field. The graph plots the e1-hh1 exciton transition energy as a function of field for two well widths. The different Stark shifts for the two widths causes an increased difference in energy between them at higher fields.

iii) Background Doping

In addition to the above inhomogeneous broadening caused variations in well width over the sample, there is also broadening through variations in electric field. This field variation is normally caused by doping impurities within the intrinsic region which cause a drop in field over the quantum wells [Newson and Kurobe].

Figure 2.5.4 shows how the field varies in an idealized p-i-n structure with a constant doping level in each region. One assumes the doping impurity density remains equal throughout the intrinsic region, and that all of these impurities ionise. These ionised dopants are charged and lead to a drop-off in field over the intrinsic region. Since each well is in a different field and because the subband energy is strongly dependent on field, this appears as a broadening of the absorption spectrum. On increasing the bias, provided the diode is initially fully depleted, the total variation of the field over the wells remains constant. However, figure 2.5.5 illustrates that

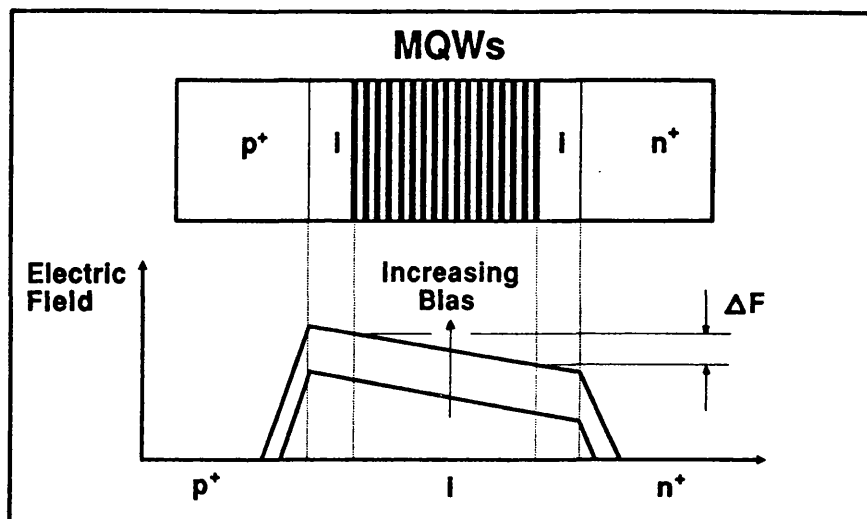


Figure 2.5.4 Diagram illustrating the variation of electric field across the quantum well as a result of background doping in the intrinsic region. The diagram is not to scale.

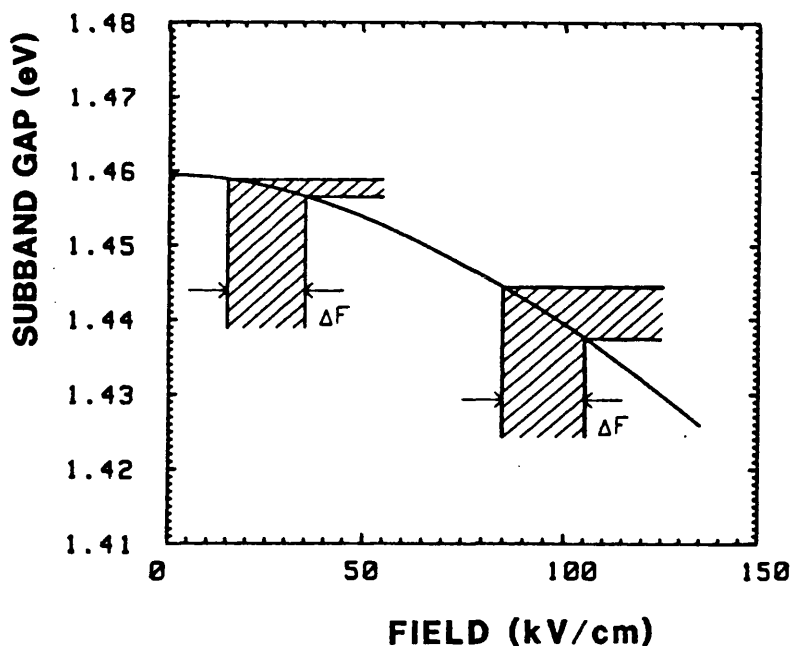


Figure 2.5.5 Graphical representation of the broadening caused by a variation of electric field across the quantum wells. The graph plots the $e1-hh1$ subband gap and shows the range of subband energies produced by a given variation in field with high and low average fields.

this variation in field at high average field gives a broader range of subband energies than the same variation at a lower average field. The broadening caused by this variation in field is proportional to the gradient of the Stark shift curve and increases strongly with the average electric field.

When the variation in field is small compared to the average field, broadening is well described as having a square lineshape of a width given by:

$$\Gamma_{sq}^{m,n} = \frac{\partial E_{cv}^{m,n}(F,W)}{\partial F} \Delta F \quad (2.5.4)$$

where ΔF is the electric field variation over the quantum wells which is given by

$$\Delta F = eN_b L_{qw} / \epsilon \quad (2.5.5)$$

where N_b is the background doping density and L_{qw} is the width of the MQW region.

This is essentially a small-signal analysis, used in our first calculations of absorption [Stevens et al., 1988], but it is not really correct for background doping levels such that the variation in electric field is of similar magnitude to the average electric field in the diode. The modulators modelled can be rather thick and hence this assumption is often invalid. Therefore we perform a more exact calculation so that the transmission through the wells is

$$T(E,V) = \exp - \int_0^{L_{qw}} \alpha(E,F) dx \quad (2.5.6)$$

where F is the field given by

$$F = (V + V_{bi}) / L_i + (N_b e / \epsilon) \cdot (x - L_{qw} / 2) \quad (2.5.7)$$

and x is the position within the intrinsic region, V the applied bias, V_{bi} the built-in voltage (assumed equal to the band-gap of the doped material to either side of the p-i-n), L_i the intrinsic region width, N_b the intrinsic region background doping, e the electronic charge and ϵ the dielectric constant of the MQWs.

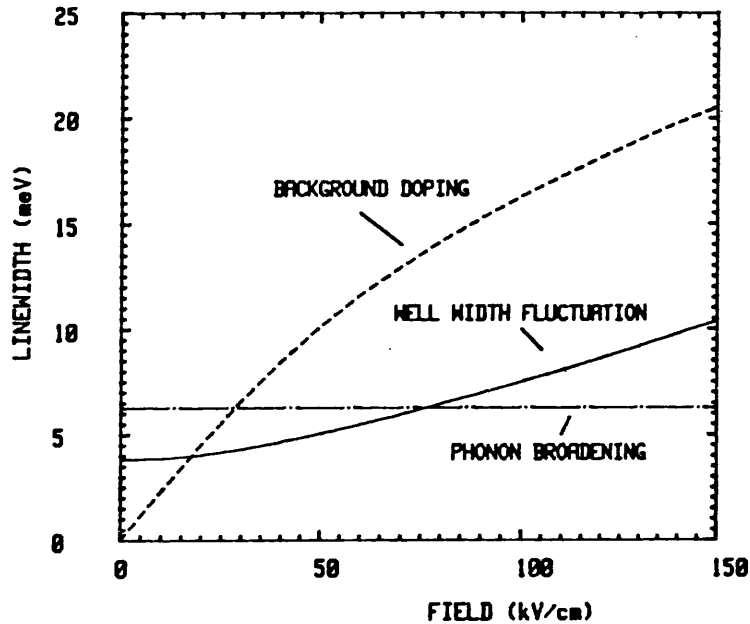


Figure 2.5.6 Full width half maximum linewidths for the dominant broadening mechanisms of the $n=1$ heavy hole to $n=1$ electron transition. The solid line is for broadening caused by an RMS well width fluctuation of 2.83 \AA . The dashed line is for broadening caused by background doping in the intrinsic region of $5.5 \times 10^{15} \text{ cm}^{-3}$ and an MQW region width of 0.511 \mu m . The dotted and dashed line is for the phonon broadening. These parameters are taken from experimental measurements on sample I.

The phonon, well width fluctuation and background doping broadening linewidths are plotted together in figure 2.5.6. The parameters used in the calculation are derived from experimental measurements on a sample that will be discussed in the next section (sample I). All three mechanisms are of the same order of magnitude, and thus all three need to be included in the calculation of the spectra.

We mention one further broadening mechanism, suggested by Miller, D.A.B. [private communication]. Ionised impurities in the sample introduce random electric fields that tend to break-up, and hence broaden, the exciton. The theory of Redfield suggests that an impurity density of $2 \times 10^{15} \text{ cm}^{-3}$ creates random electric fields of the order of 6 kV/cm which would only broaden the exciton by about 1 meV . Furthermore this form of broadening should be independent of the perpendicular field since the

exciton ionisation takes place in plane of the well. We therefore neglect it.

2.6 Comparison with Experimental Spectra

Photocurrent spectra have proved a relatively easy way of determining the energy of field dependent transitions in MQW devices [Collins et al., Viña et al., 1986, Yamanaka et al.] since it removes the necessity of etching through the GaAs substrate and applying an anti-reflection coating in order to make optical transmission measurements. In this section two photodiode samples with well widths close to 100 Å are used to compare theoretical results with experimental data.

Sample I

Sample I (KLB 461) is one of the earliest samples, and is probably the best characterised. It was used to measure the temperature dependent linewidth (figure 2.5.1) and hence used to derive the size of the phonon broadening. It was specified to include 25 quantum wells of 100 Å width with 100 Å barriers of 40 % aluminium concentration. Buffer regions of 0.05 µm were inserted between the MQWs and the doped regions to either side. Further details of the sample and the photocurrent measurement are given by Whitehead et al., 1988a. The heavy hole exciton peak position was used to estimate a well width of 98 Å, which we use in our calculations. X-ray diffraction (XRD) measurements were made on piece of the same layer and gave estimates of 209 Å for the periodicity and 105 Å for the well width. The periodicity is likely to be much more accurate than the well width estimate [Orton et al.]. Other transitions have also been used to estimate the well width and they give values ranging from 96 Å to 102.5 Å. Independent calculations produced a contour plot [Duggan et al., Orton et al.] using all of the visible transitions and assuming zero built-in field and suggested a well width of 100 Å [Duggan, G., private communication].

The barrier width (111 Å) was chosen to match the periodicity obtained from XRD analysis. The doping density in the intrinsic region ($5.5 \times 10^{15} \text{ cm}^{-3}$) was estimated from capacitance-voltage measurements on the same sample.

The photocurrent measurements were taken at a temperature of 295 K. Figure 2.6.1 plots the calculated and measured field-dependent heavy-hole

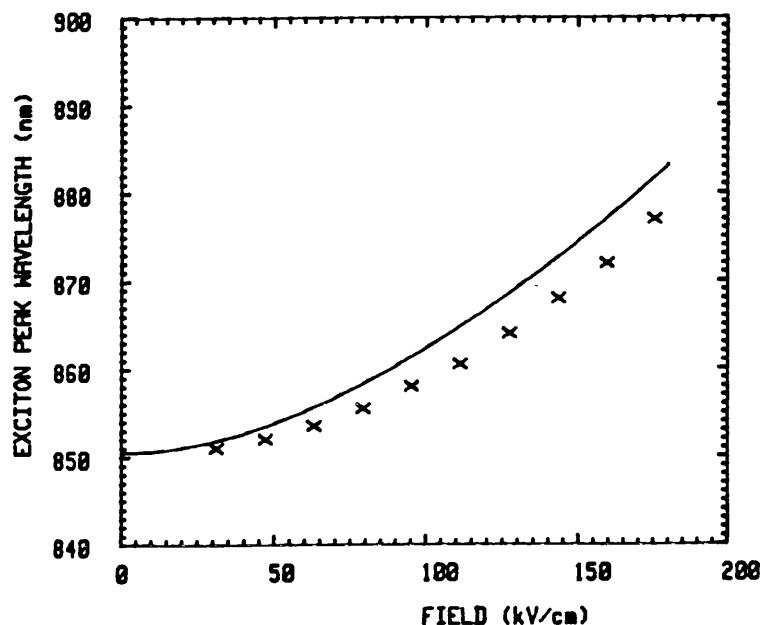


Figure 2.6.1 Wavelength of e1-hh1 exciton transition as a function of electric field for a well width of 98 Å. Plotted points are taken from photocurrent measurements on sample I.

exciton energy as a function of energy. To calculate the field for a given voltage we use the the following simple expression:

$$F = (V_{bi} + V)/L_i \quad (2.6.1)$$

It is clear that the theoretical shifts are larger than those seen in the photocurrent spectra. This discrepancy in the Stark shift is much greater than can be explained by the drop in the exciton's binding energy. A narrower well width would explain these smaller shifts but as pointed out in the previous section, XRD, growth rates and higher order transition energies point to a slightly higher well width giving a larger discrepancy in the shifts.

The basic theory for the Stark shift is supported by the fact that other authors have achieved good fits to experimental data [Miller,D.A.B. et al., 1985, Yamanaka et al., Viña et al.,1987, Collins et al.], and the fact that in later samples of our own, a much better agreement is obtained. However, other authors [Miller,D.A.B. et al.,1987, Islam et al.] have also reported that with some samples, a good fit can only be obtained by subtracting an offset

from the applied voltages. The size of this fitted potential drop varied from sample to sample and appeared correlated to the voltage at which the quantum efficiency of the photodiode levelled out. An explanation suggested for this behaviour was that a significant voltage was required to extend the depletion region over the wells. However, capacitance-voltage measurements indicated that the intrinsic region was fully depleted at zero bias and the argument is even less applicable in our case since the quantum wells cover the majority of the depletion region.

For sample I, evidence of a fixed voltage drop is seen in figure 2.5.1 because the experimental points seems to be translated horizontally with little change in shape. A voltage drop of 1.4 V brings much closer agreement between theory and experiment. It is interesting that this is much lower than the applied voltage (3V) at which the quantum efficiency saturates. Photocurrent measurements were made at different incident intensities, to determine whether the drop was dependent upon the current through the device, ie. resistive, but no change to the spectral shape was seen.

Part of the drop might be explained by the simplicity of model for the field in the diode. It is well known that when a doped region is placed near a quantum well, carriers from that doped region fall into the quantum well causing a voltage drop of the order of the band discontinuity. This is the principle of operation for the high electron mobility transistor. An analogous situation can be present at the edge of the quantum well region. However it is difficult to see how this could account for 1.4 V when the energy discontinuities between well and barrier are only of the order of 300 meV. A high density of deep traps within the material might cause a bigger drop.

Photocurrent data not only provides a means of determining subband energies, but also provide an estimate of the absorption spectra themselves [Whitehead et al., 1988a]. One assumes that the photocurrent has the following dependence:

$$i(\lambda) = \frac{(1-R_f)P(\lambda)e\eta_{\text{int}}}{E} [1-\exp(-\alpha(\lambda)L_{\text{qw}})] \quad (2.6.2)$$

and λ is the wavelength, P the incident light power, d the intrinsic region thickness, R_f is the front surface reflectivity, η_{int} is the internal quantum efficiency, defined as the ratio of carriers collected to photons absorbed. If we assume that R_f and η_{int} are wavelength independent, we can rearrange

(2.6.2) so that

$$\alpha(\lambda) = (1/L_{qw}) \ln[\lambda/(\lambda - \beta i(\lambda)/P(\lambda))] \quad (2.6.3)$$

where

$$\beta = hc/(1-R_f)\eta_{int}e \quad (2.6.4)$$

The conversion factor, β , depends upon the quantum efficiency. If the absorption at a given wavelength is known, β can be evaluated for a given spectrum. This is done in a field-invariant part of the spectrum at shorter wavelengths, using an absorption value taken from unbiased transmission measurement on the same layer.

Figures 2.6.2 shows the voltage-dependent absorption spectra derived from the photocurrent. Figure 2.6.3 shows the calculated spectra assuming the 1.4 V drop in the device. Parameters used in the calculation are listed in table 2.6.1. The spectra include the e1-hh1 and e1-lh1 transitions as well as the e1-hh2 forbidden transition. It is worth clarifying what are the fitted parameters: i) the *well width* so that the unbiased heavy hole exciton peak is lined up; ii) the *strain shift* of the light hole exciton peak; iii) the *broadening* (phonon and well width fluctuation) to obtain the correct linewidth in the unbiased spectra; and iv) the *voltage drop* of 1.4 V to achieve matched Stark shifts. Note that all but iv) are fits to the unbiased spectrum alone and are independent of the biased spectra. The rms well width fluctuation of 2.83 Å was estimated by deconvolving the background doping broadening from the low temperature (4.2 K) linewidth, and is equivalent to about a monolayer of material.

The agreement between figures 2.6.2 and 2.6.3 is generally very good for the e1-hh1 and e1-lh1 exciton peaks, but the trough between e1-lh1 and the forbidden e1-hh2 exciton transitions is deeper in the theory, and the forbidden transition itself is more prominent. The fit between experiment and theory can be expected to get worse the further into the band one goes as mixing between valence band states becomes more important [Weisbuch]. One other discrepancy between theory and experiment occurs in the bandtails where the value of the computed absorption is much higher than that experimentally measured. This difference arises from the use of Lorentzian lineshapes that have very wide "skirts" in contrast to experimental spectra that have exponential band-tails. This discrepancy will not effect the design of transverse electroabsorption modulators, which work close to the exciton peaks, but would be important in the design of waveguide modulators.

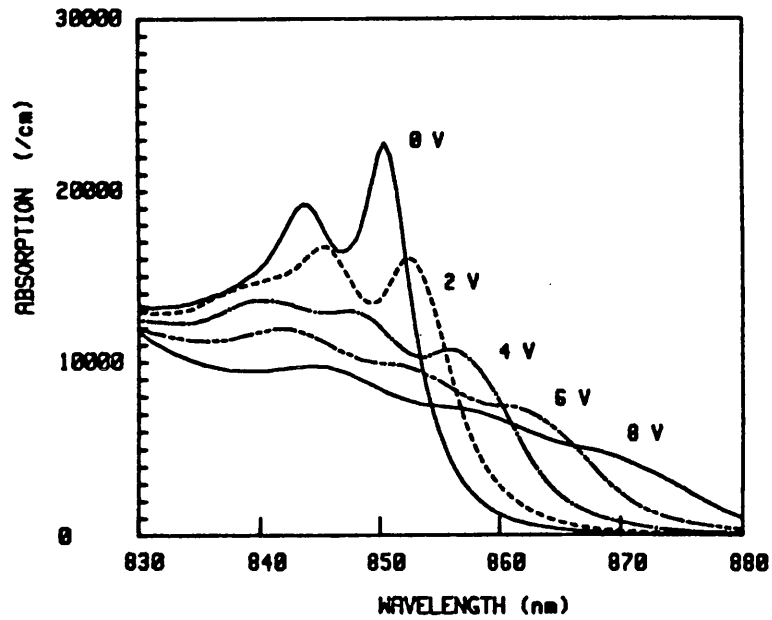


Figure 2.6.2 Bias-dependent absorption spectra for sample I derived from photocurrent measurements. Absorption is for the well only (α_{qw}). Measurement by M.Whitehead using samples grown by K.Woodbridge at Philips Research.

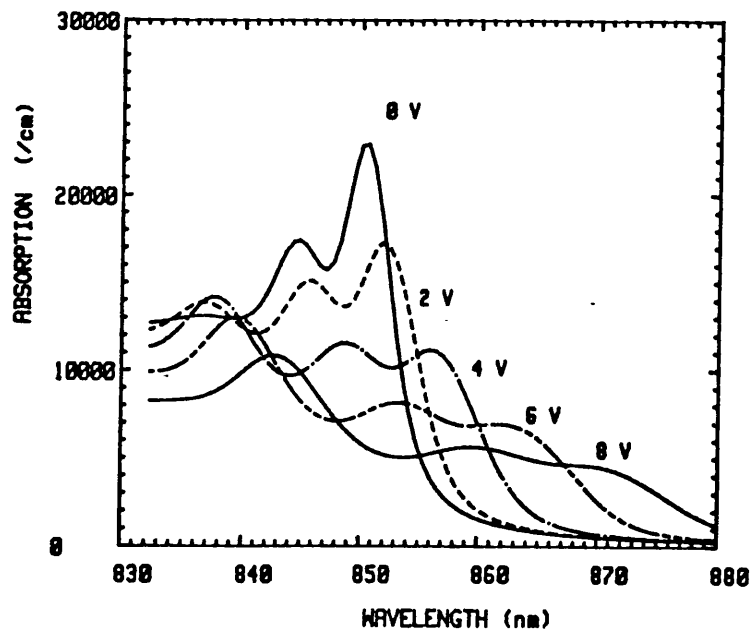


Figure 2.6.3 Calculated bias-dependent absorption spectra for sample I. A 1.4 volt drop is assumed when calculating the field in the device.

Sample	I	II
Well Width (Å)	98	97
Barrier Width (Å)	111	100
Number of Wells	25	20
Intrinsic Region Width (µm)	0.622	0.984
Barrier Aluminium Concentration (%)	40	30
RMS Well Width Fluctuation (Å)	2.83	2.12
Intrinsic Background Doping (cm ⁻³)	5.5x10 ¹⁵	6x10 ¹⁴
Measurement Temperature (K)	295	303

Table 2.6.1 Parameters assumed in calculation of absorption spectra for comparison with the experimental data from samples I and II

Sample II

Sample II is from a later layer (M33) that shows excellent material characteristics. It is grown as 20 wells of 100 Å with 100 Å barriers of 30 % aluminium concentration surrounded by buffer regions of 0.3 µm thickness and 16 % aluminium aluminium concentration, surrounded by buffer regions of 0.3 µm concentration. Capacitance-voltage measurements show an intrinsic doping density of around 6x10¹⁴ cm⁻¹.

From the heavy hole exciton wavelength we estimate the real well width to be 97 Å. As is shown in figure 2.6.4, excellent agreement for the Stark shift between theory and experiment is obtained with no voltage drop of the type required for sample I. In figure 2.6.5 we calculate the absorption from the photocurrent, and the spectra can be compared to the calculated spectra of figure 2.6.6. Because of the better quality of growth, notably the order of magnitude lowering of the intrinsic doping, the field enhancement of the broadening is reduced in sample II. Note that in this case, the experimental e1-hh1 exciton seems to decay more rapidly than the theory predicts, although at very high biases there was an unexpected increase in the exciton strength. The reason is unclear but this was probably not attributable to the quantum well absorption, but related to assumptions

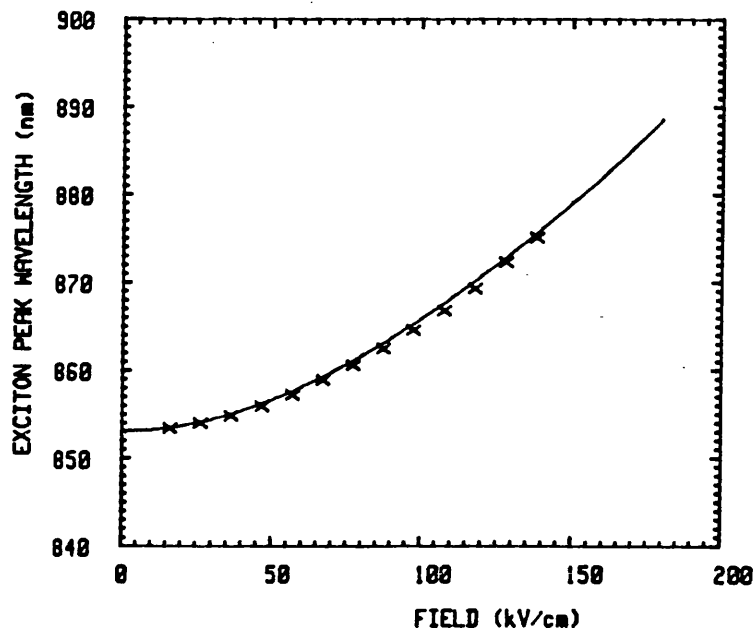


Figure 2.6.4 Wavelength of e1-hh1 exciton transition as a function of electric field for a well width of 97 Å. Plotted points are taken from photocurrent measurements on sample II.

made in the conversion of photocurrent to absorption. Although the conversion assumes a constant front surface reflectivity, the reflectivity in similar samples has been seen to vary over wavelength and a more complex analysis of layered surface is required. Close to the bandedge, dispersion of the refractive index occurs, worsening these effects.

In addition to the the above comparisons of the theory with spectra derived from photocurrent measurements, we have also compared our calculation to direct measurements of the absorption spectra carried out by Jelley et al. and Hsu et al. who have fabricated full modulators with high quality anti-reflection coatings. Good agreement for both the shifts, oscillator strengths and broadening of the heavy hole exciton was found in both cases, increasing further our confidence in the model. However, as for the samples presented here, the forbidden transition was always more prominent in the model than in the experimental spectra.

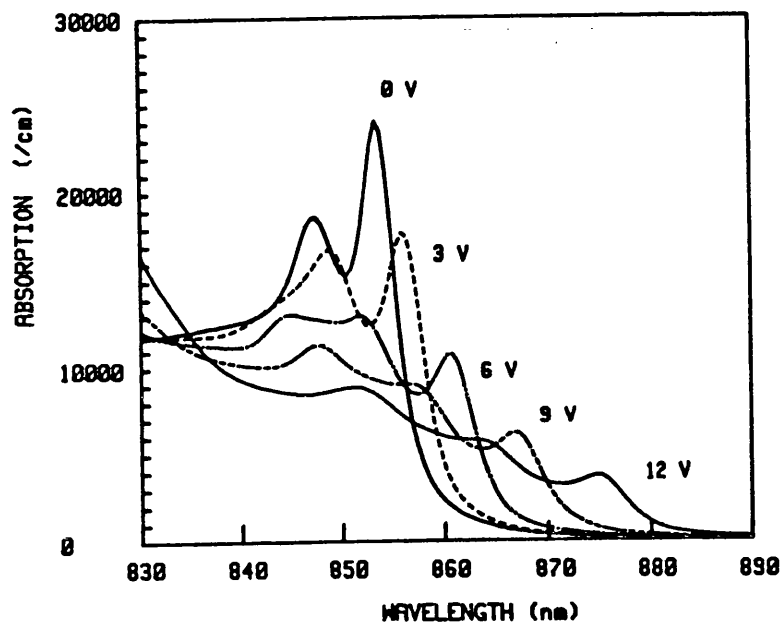


Figure 2.6.5 Bias-dependent absorption spectra for sample II derived from photocurrent measurements. Measurement by M.Whitehead using samples grown by K.Woodbridge at Philips Research.

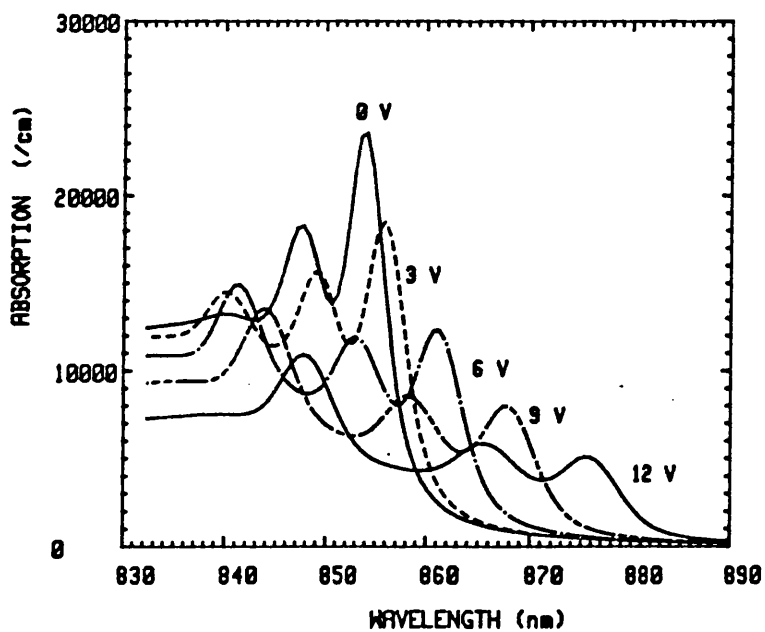


Figure 2.6.6 Calculated bias-dependent absorption spectra for sample II.

2.7 Effect of Well Width on Absorption Spectra

In figures 2.7.1, 2.7.2 and 2.7.3, we present the calculated absorption spectra for MQW diodes of approximately $1 \mu\text{m}$ thickness, one monolayer well width fluctuation and $2 \times 10^{15} \text{ cm}^{-3}$ background doping, but with well widths of 50, 100 and 150 Å respectively. The shape of the spectra demonstrate the same qualitative features as the measurements on modulators presented by Whitehead et al. [1988b] with well widths of 47, 87 and 147 Å.

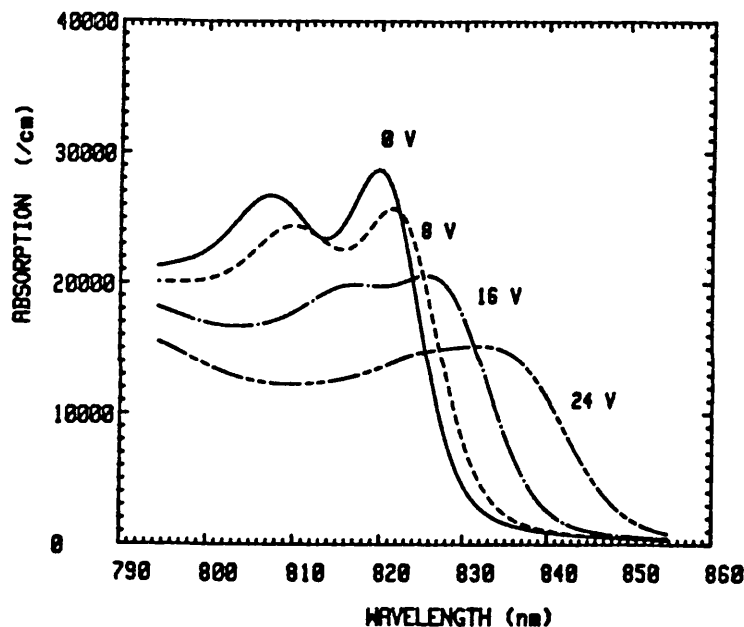


Figure 2.7.1 Calculated absorption spectrum for a MQW diode composed of 91 wells of 50 Å with barriers of 60 Å thickness, and 30 % aluminium concentration. The background doping is $2 \times 10^{15} \text{ cm}^{-1}$ and the rms well width fluctuation is one monolayer.

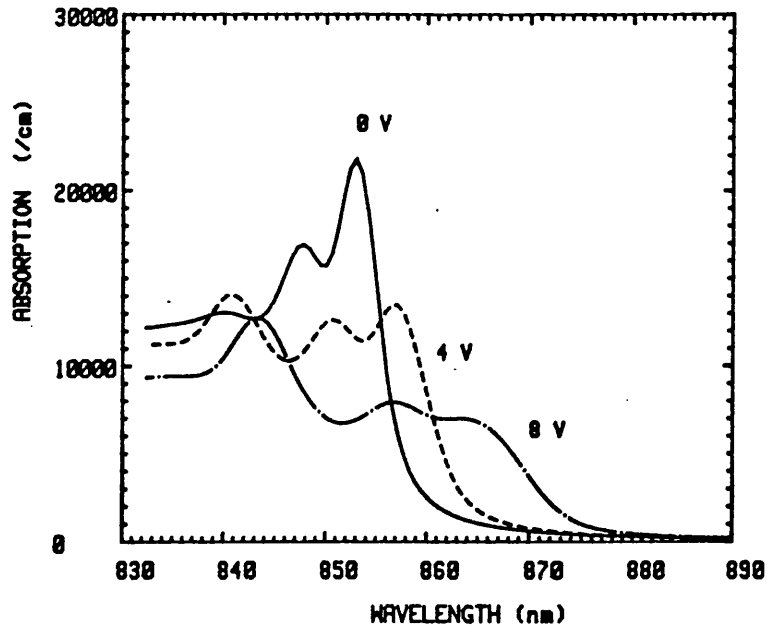


Figure 2.7.2 Calculated absorption spectrum for a MQW diode composed of 63 wells of 100 Å with barriers of 60 Å thickness, and 30 % aluminium concentration. The background doping is $2 \times 10^{15} \text{ cm}^{-1}$ and the rms well width fluctuation is one monolayer.

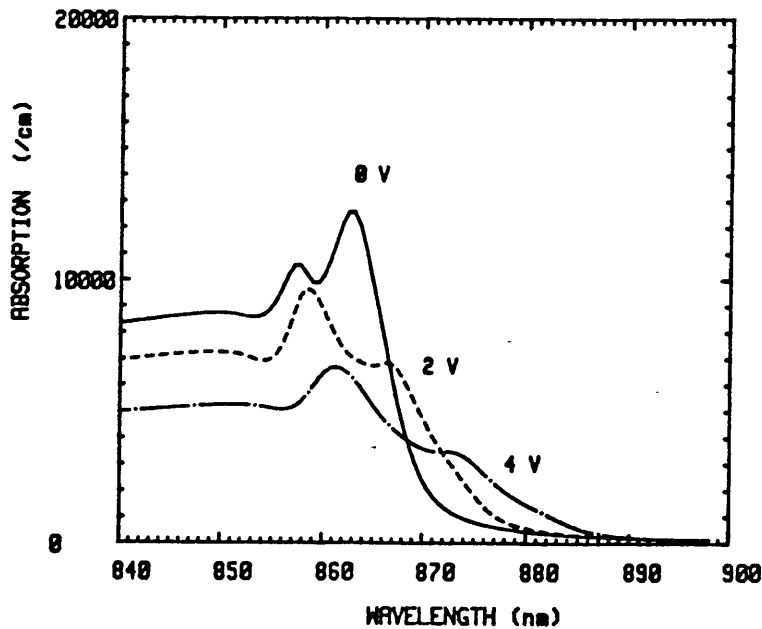


Figure 2.7.3 Calculated absorption spectrum for a MQW diode composed of 48 wells of 150 Å with barriers of 60 Å thickness, and 30 % aluminium concentration. The background doping is $2 \times 10^{15} \text{ cm}^{-1}$ and the rms well width fluctuation is one monolayer.

The most obvious conclusion which can be drawn from these results is that the exciton peaks in narrower wells shift slowly with field but retain more of their strength. The decreasing Stark shift in narrower wells is predicted by theory. In figure 2.7.4 we plot the field-dependent exciton wavelength as a function of well width. The physical picture is quite easy to understand. Under the electric field, the quantum well tilts and the particle move toward the bottom corner of the well. The energy level however is always relative to the centre of the well. In wider wells the bottom corner is a much lower energy to the centre of the well and hence larger shifts in the particle energy occur.

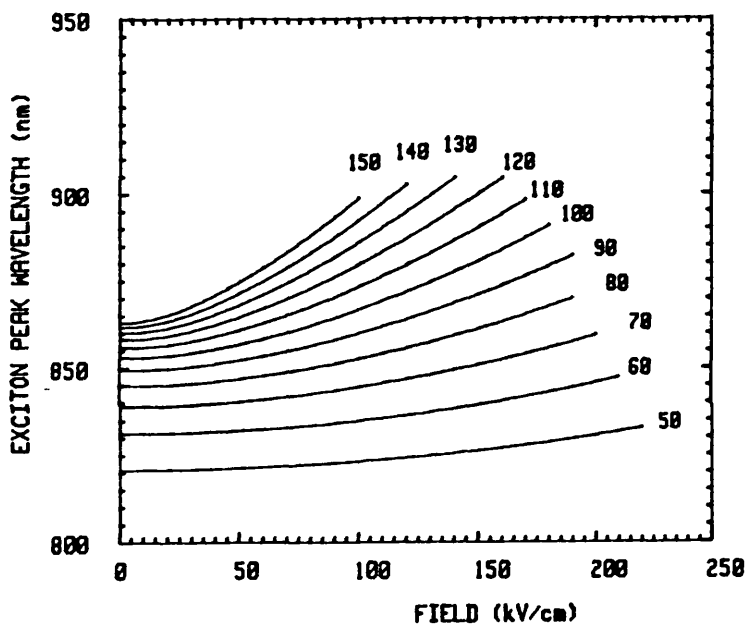


Figure 2.7.4 Wavelength of e1-hh1 exciton against electric field for well widths between 50 and 150 Å.

The retention of exciton's peak absorption by the narrow well exciton can be explained by the following:

- i) The exciton oscillator strength is dependent upon the overlap of the electron and hole wavefunctions, but in narrower wells spatial separation is much more difficult to achieve. Figure 2.7.5 plots the square of the overlap integral against Stark shift for different well widths. It is clear that at a given Stark shift the exciton in a narrower well retains a greater oscillator strength.

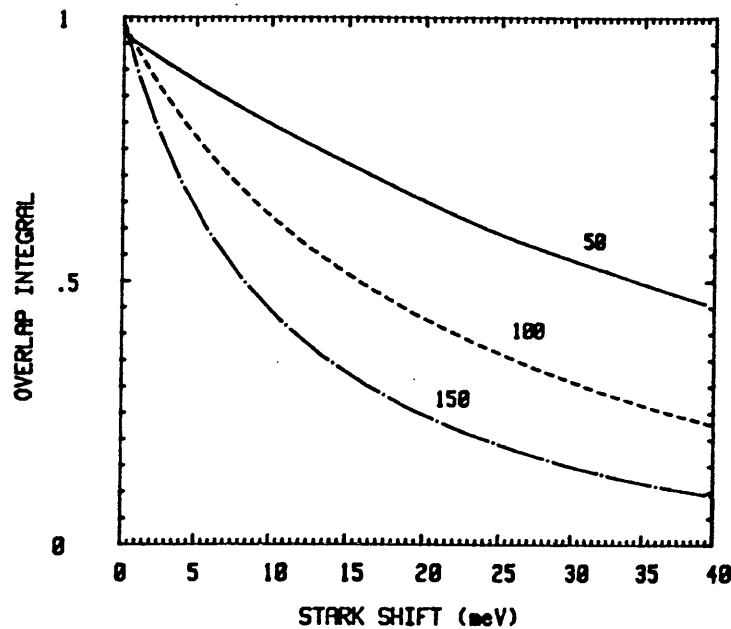


Figure 2.7.5 Square of e1-hh1 overlap integral against Stark shift for 50, 100 and 150 Å well widths

ii) The exciton peak height is not only dependent upon its oscillator strength but also its linewidth. Both well width fluctuation broadening and broadening due to background doping are both related to the Stark shift, and since the Stark shift is smaller for narrower well the broadening does not increase with field.

2.8 Summary

We have presented a relatively simple, but realistic, model for the field dependent absorption in MQW diodes. The model will calculate absorption for different well widths, and includes all the significant broadening mechanisms: phonon scattering, well width fluctuations and field variation due to background doping. The calculation has been compared to experimental absorption spectra derived from photocurrent measurements, and we find that in some samples a voltage drop within the diode must be assumed in order to achieve good fits between experimental and theoretical Stark shifts. The source of this drop is still unclear, but we find that no such

discrepancy occurs in samples of better quality. Finally we analyse the effect of well width on the absorption spectra, and explain why the Stark shift in narrower wells requires a higher electric field, but the exciton retains more of its strength.

Chapter 3

OPTIMISATION OF DEVICE MODULATION

3.1 Introduction

In chapter 2 we investigated the theory of quantum well electroabsorption and explained a model enabling us to calculate the absorption at a given electric field and wavelength. In this chapter we use the calculation of field-dependent absorption to calculate achievable modulation in devices. Section 3.2 covers the design of waveguide modulator, but the bulk of the chapter is concerned with transverse modulator design.

In this chapter we make use of this model to calculate the achievable modulation in devices.

3.2 Waveguide Devices

MQW waveguide modulators were proposed by Tarucha et al. [1985] as a means of increasing the optical interaction length and therefore obtaining much higher contrasts. In a waveguide device one has the freedom to choose device length independently of the p-i-n and waveguiding structure. Let us consider the optimum length of the device. If the device is too short, a given absorption change will only give a small contrast, whereas if too long, the zero bias absorption will lead to a large insertion loss. Neglecting coupling losses into the waveguide, the transmission through the modulator is solely determined by the absorption in the quantum wells and is given by

$$T = \exp[-\Gamma\alpha(V)l] \quad (3.2.1)$$

where Γ is the confinement factor, $\alpha(V)$ is the absorption in the quantum well at voltage V and l is the length of the device. The contrast ratio is then given by

$$K = T_{hi}/T_{lo} = \exp[\Gamma\Delta\alpha l] \quad (3.2.2)$$

where $\Delta\alpha = \alpha(V) - \alpha(0)$.

Thus the maximum *contrast* always increases with increased length and the optimum wavelength is that of maximum change in absorption. However with increasing length the *transmission change* will eventually

start decreasing because of an increasingly large insertion loss associated with the zero bias absorption. The optimum length is given by

$$l_{\text{opt}} = (1/\Gamma\Delta\alpha) \ln[\alpha(V)/\alpha(0)] \quad (3.2.3)$$

with the maximum transmission change

$$\Delta T_{\text{max}} = x.(1+x)^{-(1+x)/x} \quad (3.2.4)$$

where $x = \Delta\alpha/\alpha(0)$

One notes that the optimum length scales inversely with optical confinement factor and that it is $\Delta\alpha/\alpha(0)$ which determines the optimum transmission change. Measurements of $\Delta\alpha$ and $\Delta\alpha/\alpha(0)$ in (GaAl)As/GaAs quantum wells give typical values of 3000 cm^{-1} and 20 which give rise to a massive contrast of $>10^5$ in a $200 \mu\text{m}$ length, 20% confinement factor device, and an optimum transmission change of 80%. Similarly high performance can also be achieved with a bulk material intrinsic region using the Franz-Keldysh effect [Noda,S. et al.].

In practice however, many of the reported modulators have a high insertion loss arising from the difficulty of coupling into a narrow waveguide. It is for this reason that Koren et al. [1987b] have recently proposed and demonstrated the use of wider guides to ease coupling difficulties and hence achieve a much better insertion loss (2.9 dB).

The design of the p-i-n diode can be independent of the waveguide design, and here there is an obvious trade off between the operating voltage and the device speed. The narrower the p-i-n, the greater the electric field for a given voltage but the larger the device capacitance.

One further factor that is likely to dominate the design of waveguide modulators is that they will probably be used within an opto-electronic integrated circuit (OEIC) where coupling problems are eased because the surrounding devices are in waveguide form anyway. To prevent a separate stage of epitaxial growth in such an OEIC, the layer structure chosen should be multifunctional and the optimum design of the individual device might be compromised. One particularly interesting problem is the integration of a laser and a modulator. Tarucha et al. [1986] fabricated just such a combination with MQWs, but coupling losses between devices were large and further work on the joint optimisation of the laser and modulator is required.

Finally we mention the importance of chirping induced by changes in the refractive index accompanying the electroabsorption. This will be dealt with in section 5.2 on high speed fibre-optic links.

To conclude, we note that electroabsorption in waveguide modulators can be used for very good modulation, and their design does not so much depend upon the electro-absorption, but external concerns such as coupling to surrounding devices and integration with lasers. There is also no clearcut reason why QWs should give significantly better performance than bulk devices. In light of these considerations, we do not devote much effort to optimisation of waveguide devices for the modulation alone.

3.3 Transverse Modulator Optimisation Technique

There are two factors that make the design of transverse devices different from that of waveguide ones. The most important is that the absorbing thickness is limited by the need to keep the intrinsic region thin so that high fields can be applied over the wells at reasonable operating voltages. This restriction forces devices to operate at the exciton peaks where the largest changes in absorption occur. Secondly, one cannot define a fixed absorption coefficient at a given field/voltage like that shown in expression 3.2.1 because the average absorption coefficient in a given thickness is dependent upon that thickness because of the variations in field caused by background doping.

There are many variables affecting the modulation in a MQW diode. Firstly there is the structure of the MQWs, or more precisely, the well width, barrier width and the number of wells. Three well widths are considered in this work: 50, 100 and 150 Å. The barrier width is kept as small as possible so that the proportion of absorbing material in the intrinsic region is maximised and yet tunnelling induced broadening and interaction between the wells is unimportant. Experimental results show that 60 Å (30% aluminium) provides such isolation. Then there is the quality of the growth, characterised by the background doping in the intrinsic region and the RMS well width fluctuation. For the optimisation these are initially fixed at typical values for present-day MOCVD technology, and then the effects of improvements are investigated. The final variables are the operating wavelength and voltage.

Figure 3.3.1 shows the calculated bias dependent transmission through

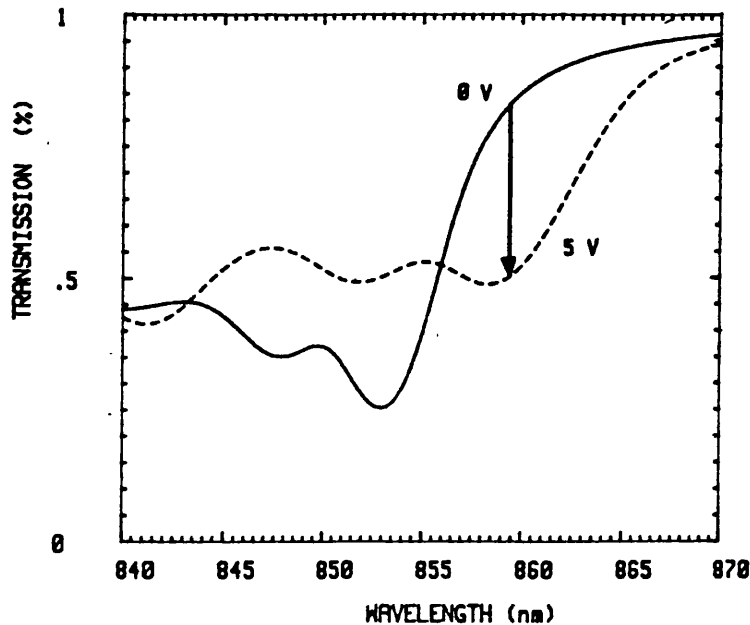


Figure 3.3.1 Calculation of the bias dependent transmission through a GaAs/(GaAl)As MQW diode of 63 periods of 100 Å wells and 60 Å barriers. The best operating wavelength is at the biased heavy hole exciton peak as indicated. The background doping is $2 \times 10^{15} \text{ cm}^{-3}$ and the rms well width fluctuation is 1 monolayer.

MQWs and it is obvious that the greatest modulation is achieved at the exciton peaks where the largest changes in absorption occur. However there is a choice of setting the wavelength to that of the unbiased exciton peak, in a bias-transmitting mode, or choosing the biased peak in a bias-absorbing mode. Initially we shall consider the first of these: the bias absorbing mode.

Of the foregoing list of parameters, only two are still free ones: the number of wells and the operating voltage. These are intimately related to one another since the thicker the intrinsic region, the greater the voltage that is required to achieve a given exciton shift. The optimum structure one designs is therefore dependent upon what voltage one is willing to use.

Device optimisation therefore needs to be carried out at a fixed voltage by varying the number of wells. In figure 3.3.2 we do this by plotting the transmission change at the exciton peak as a function of the number of wells at a given, fixed, operating voltage. We call this graph a *voltage invariant*

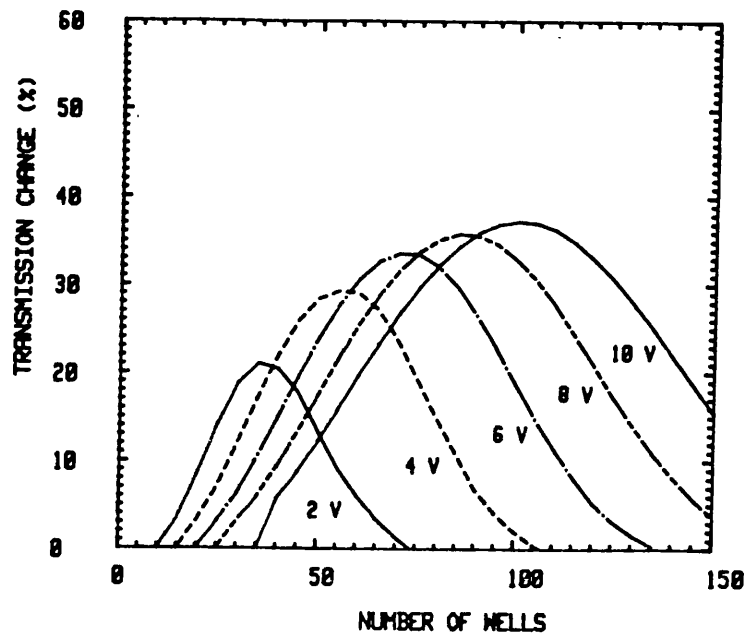


Figure 3.3.2 Voltage invariant optimisation (VIO) curves for a non-resonant bias-absorbing transmission modulator with well width of 100 \AA . The transmission change is plotted for several design voltages as the number of wells is varied. The background doping is $2 \times 10^{15} \text{ cm}^{-3}$ and the rms well width fluctuation is 1 monolayer.

optimisation (VIO) plot, and it forms the basic step in all the optimisation. Note that because the device thickness is varied while keeping the voltages constant, the field within the device changes, and with it the operating wavelength. The transmission change is evaluated just from the field dependent absorption in the quantum wells and hence assumes perfect anti-reflection coatings are applied to *both* the front and back surfaces. With a low number of wells the thickness of absorbing material is small and hence the transmission change is low. For large numbers of wells at the fixed operating voltage, the electric field is small and the Stark shifts are insufficient to achieve a sizeable transmission change. In between there is a maximum : at the optimum number of wells for a given design voltage.

The same optimisation technique is applicable for any chosen figure merit to describe the modulation, and any model for the field dependent absorption.

3.4 Bias Absorbing, 100 Å Well Width Performance

In figure 3.4.1 we have plotted the optimum transmission change against the design voltage for the standard device with 100 Å wells, $2 \times 10^{15} \text{ cm}^{-3}$ background doping and 1 monolayer RMS well width fluctuation (curve a). We also show results for devices with background dopings of 10^{14} cm^{-3} (curve b), 0.5 monolayer well width fluctuation (curve c) and a double pass reflection modulator (curve d). The optimum number of wells at which those transmission changes occur is plotted in figure 3.4.2.

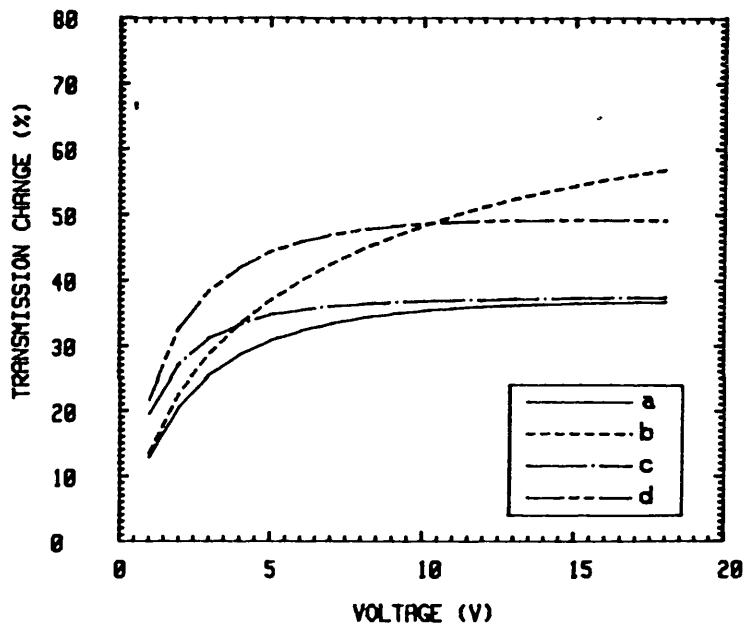


Figure 3.4.1 Optimum transmission change against operating voltage for 100 Å well width non-resonant bias-absorbing modulators. Curves a) to d) represent modulator with differing material characteristics (table 3.4.1).

DEVICE	WELL WIDTH (Å)	BACKGROUND DOPING (cm^{-3})	RMS WELL WIDTH FLUCTUATION	SINGLE/DOUBLE PASS
a)	100	2×10^{15}	1 monolayer	single
b)	100	10^{14}	1 monolayer	single
c)	100	2×10^{15}	1/2 monolayer	single
d)	100	2×10^{15}	1 monolayer	double

Table 3.4.1 Device parameters for modulators investigated.

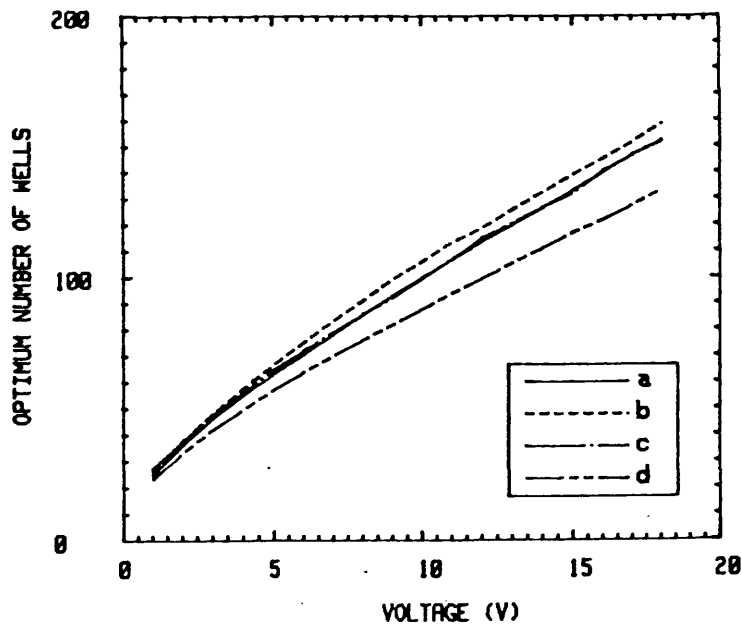


Figure 3.4.2 Graph of the number of wells required to give the optimum transmission change (figure 3.4.1), against operating voltage for devices with a well width of 100 Å.

Several conclusions can be drawn from these results:

- i) The variation of the optimum number of wells against design voltage is close to linear with the electric field staying almost constant.
- ii) With higher design voltages, after a certain point there seems to be little subsequent improvement in attainable transmission change. For the devices with a background doping of $2 \times 10^{15} \text{ cm}^{-3}$ doping, this limitation is imposed by the resultant field variation from well to well. The wider the intrinsic region the greater this form of broadening becomes, cancelling out the increase in the amount of absorbing material.
- iii) The improvement in the interface quality makes little difference to the attainable transmission change since the well width fluctuation broadening in the biased state is eclipsed by the broadening caused by the background doping.
- iv) Double pass modulators are able to achieve higher transmission changes with fewer wells and hence lower voltages because of the doubling of the optical interaction length.

Exactly the same procedure is applicable to the optimisation of contrast as opposed to the transmission change. Figure 3.4.3 shows the plot of optimum contrast against operating voltage. The number of wells in a contrast-optimised device is greater than that in the transmission change-optimised one. This has two effects: both the optical interaction length is increased and a lower field is present at a given bias and hence the wavelength selected is closer to the zero-bias exciton peak. Both of these lead to high insertion losses, as shown in figure 3.4.4. The large number of wells also makes the achievable contrast at larger voltages very sensitive to the background doping. The contrast of the double pass modulator (in dB) is exactly twice that of the equivalent single pass one and has the same optimum number of wells.

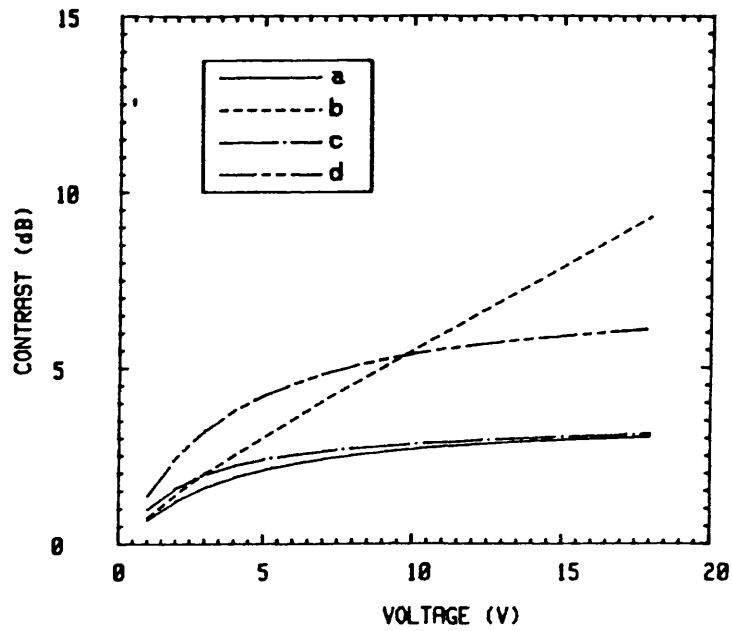


Figure 3.4.3 Optimum contrast ratio against operating voltage for 100 Å well width non-resonant bias-absorbing modulators. Curve a) to d) represent modulators with differing material characteristics, as listed in table 3.4.1.

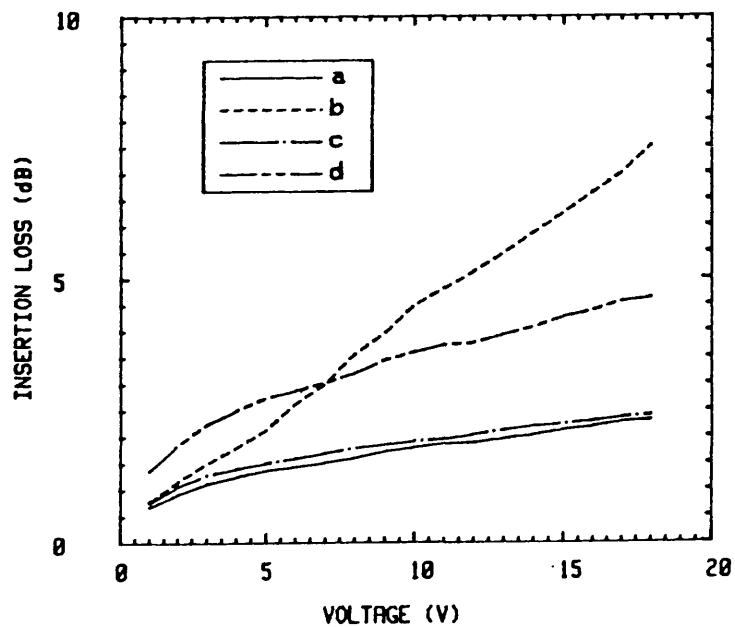


Figure 3.4.4 Insertion loss due to zero bias absorption for the optimum contrast devices of figure 3.4.3.

3.5 Effect of Well Width on Modulation

In section 2.7 we have already shown that the well width has a profound effect upon the characteristics of the absorption spectrum. In figure 3.5.1 we plot the optimum transmission change as a function of voltage for well widths of 50, 100 and 150 Å. In narrower wells, the increased fields required to give a significant Stark shift, increase the device operating voltage. It is thus only with voltages of > 18 V that the performance of the 50 Å device exceeds that of the 100 Å, reflecting the fact that while it takes a higher field to shift the exciton, it retains more of its oscillator strength. The 150 Å device performance is poor because of the faster loss in the exciton's oscillator strength with field and the large field-enhanced broadening caused by background doping in the intrinsic region.

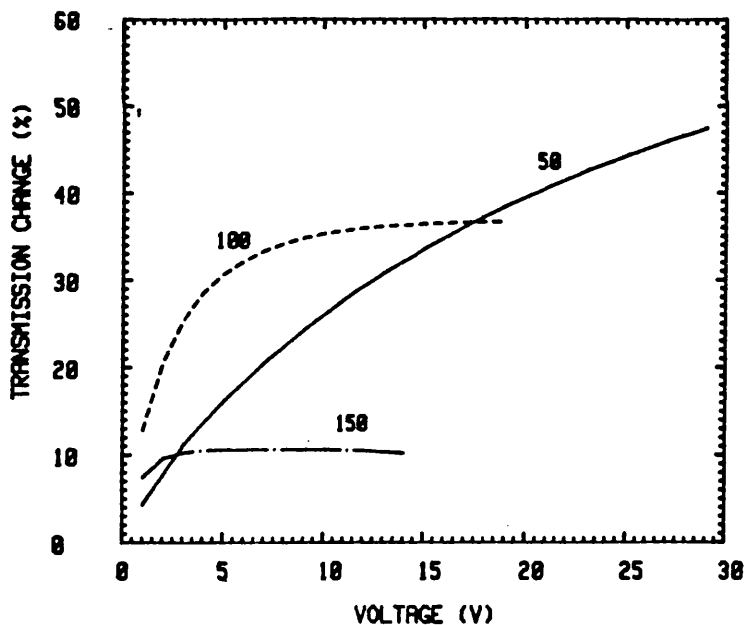


Figure 3.5.1 Optimum transmission change against operating voltage for non-resonant bias-absorbing transmission modulators with well widths of 50, 100 and 150 Å. The background doping is $2 \times 10^{15} \text{ cm}^{-3}$ and the rms well width fluctuation is 1 monolayer.

The comparative effect of intrinsic background doping on devices of different well width operating at 5 V is shown in figure 3.5.2. Substantial improvements of the achievable modulation in the 150 Å device are possible with lower doping, but almost no improvement is seen for the 50 Å device. This is because the broadening in wide wells is dominated by the background doping, while in narrow well it is dominated by the well width fluctuations. Figure 3.5.3 shows the comparative effect of well width fluctuation on the modulation performance. Here it is the narrow well width device that is most affected, since a given well width fluctuation is a greater fraction of the overall well width.

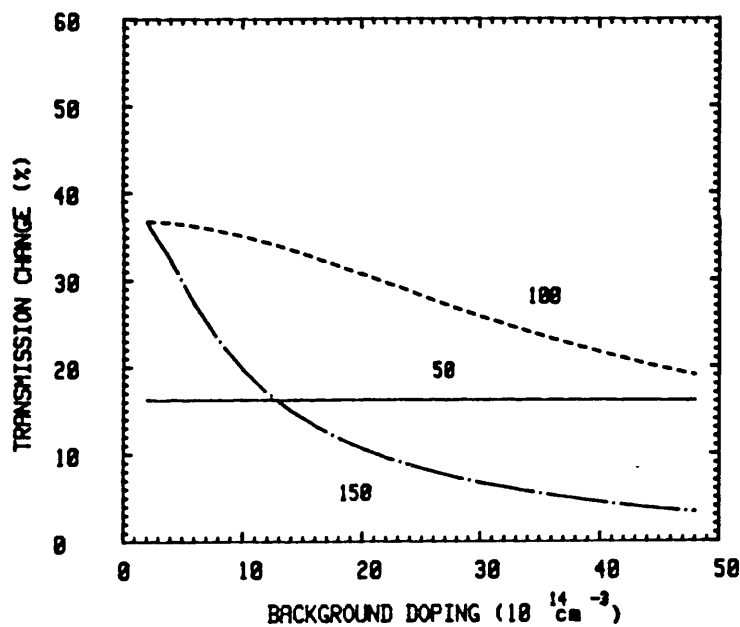


Figure 3.5.2 Effect of background doping upon transmission change in optimum 5 V non-resonant bias-absorbing modulator with well widths of 50, 100 and 150 Å. The rms well width fluctuation is 1 monolayer.

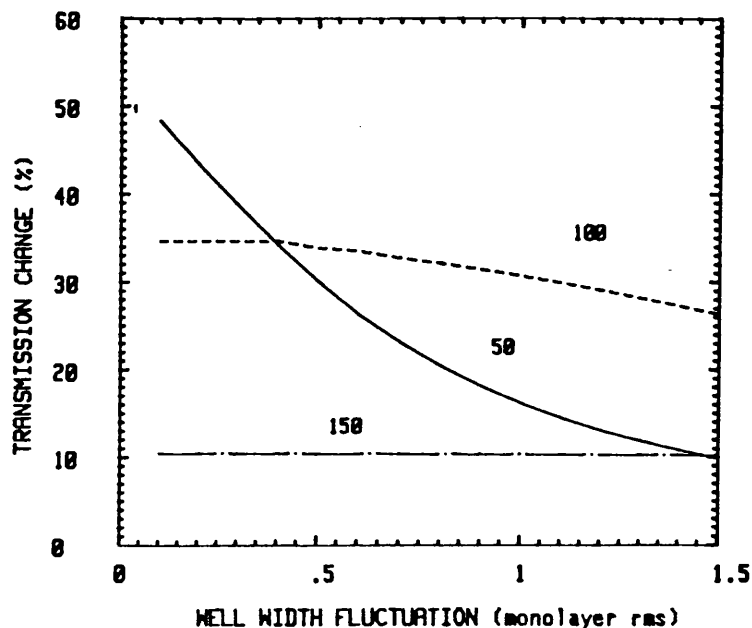


Figure 3.5.3 Effect of well width fluctuation upon transmission change in optimum 5 V non-resonant bias-absorbing modulator with well widths of 50, 100 and 150 Å. The background doping is $2 \times 10^{15} \text{ cm}^{-3}$.

3.6 Bias Transmitting Mode

In the previous calculations, the chosen wavelength was that of the biased exciton peak, and the absorption is dominated by the heavy hole exciton alone. The alternative, bias-transmitting mode, selects the unbiased exciton peak, which shifts and subsides upon the application of the field. The residual biased absorption is now made up of contributions due to the heavy hole, light hole and forbidden transitions. The optimisation of the bias-transmitting mode can proceed in the same way, but the VIO plot has more features than the single maximum for the bias-absorbing mode, because of the other participating transitions. Figure 3.6.1 shows the VIO plot for a 100 Å device. The shape is best explained as the same sort of peak as for the bias absorbing mode, but superimposed is a depression at fields where the biased absorption is at the light hole exciton peak. This leads to a twined-peak VIO

plot. Note that the peak at fewer wells is less reliable because our model for the field dependent absorption becomes less accurate for wavelengths below the light hole exciton (see section 2.6). The transmission changes shown in

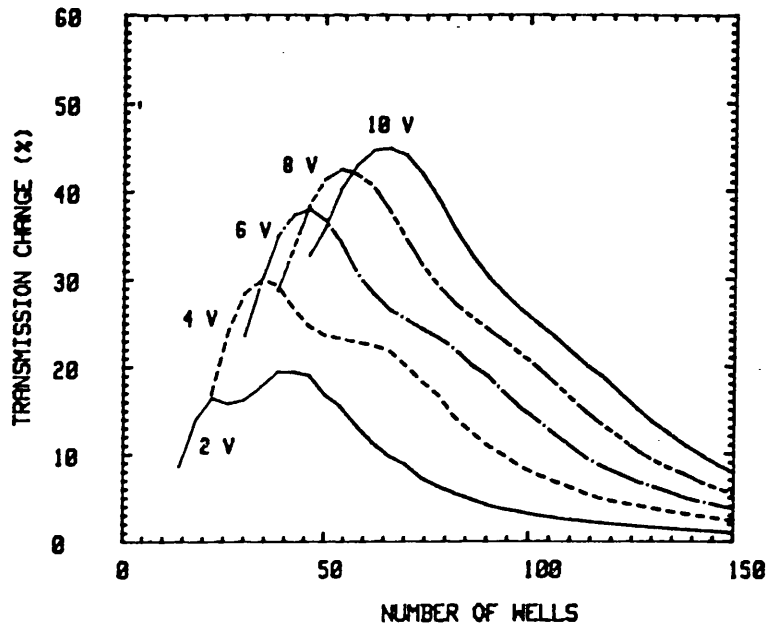


Figure 3.6.1 Voltage invariant optimisation (VIO) curves for non-resonant bias-transmitting transmission modulator with well width of 100 Å. Background doping is $2 \times 10^{15} \text{ cm}^{-3}$ and the rms well width fluctuation is 1 monolayer.

figure 3.6.1 are not very different to those for the bias-absorbing mode (figure 3.3.2), although it is found that the high state transmission (ie. the insertion loss) is lower and the associated contrast is higher.

Figure 3.6.2 shows the VIO plot for a modulator with a 150 Å well width, and this time the the bias-transmitting mode does offer a substantial improvement in transmission change over the bias-absorbing mode (from 10.5 to 26% at 5 V). Here both the sensitive Stark shift and the rapid loss of exciton oscillator strength improve the device performance. However it still does not offer a significant improvement over either the 100 Å bias-absorbing or bias-transmitting modulators. Note that the twinned peak nature of the plot is now not related to the light hole exciton peak, but rather the e1-hh2 forbidden transition which is prominent at low electric fields.

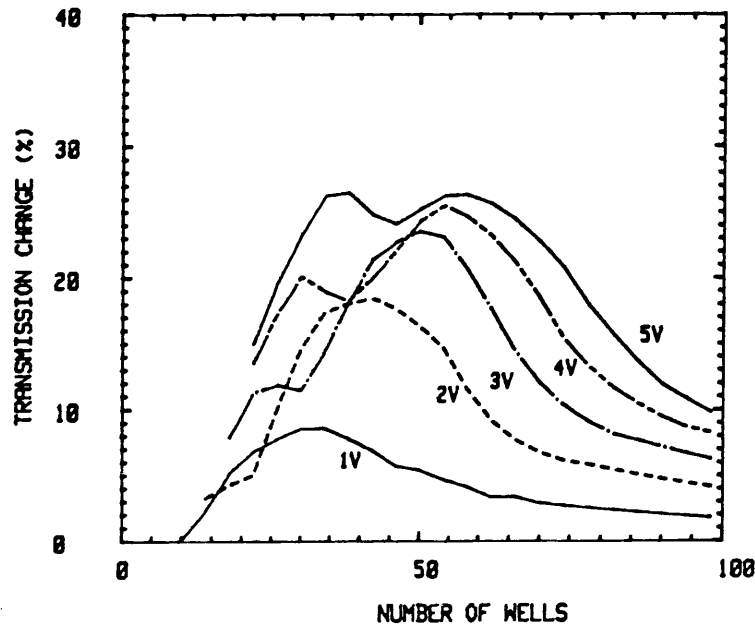


Figure 3.6.2 Voltage invariant optimisation (VIO) curves for non-resonant bias-transmitting transmission modulator with well width of 150 Å. Background doping is $2 \times 10^{15} \text{ cm}^{-3}$ and the rms well width fluctuation is 1 monolayer.

3.7 Resonant Devices

The above work modelling non-resonant devices is easily extended to analyse the performance of resonant modulators such as the asymmetric Fabry-Perot modulator (AFPM). The resonant wavelength condition of such modulators is

$$\lambda_r = 2n_{in}L_{cav}/m \quad (3.7.1)$$

where n_{in} is the mean refractive index in the cavity, L_{cav} is the cavity width, and m is an integer.

At this resonant wavelength the transmission and reflection are given by

[Whitehead et al., 1989a]:

$$T_r = \frac{T_{nr}(1-R_f)(1-R_b)}{(1-R_\alpha)^2} \quad (3.7.2)$$

$$R_r = \frac{R_f[1-(R_\alpha/R_f)]^2}{(1-R_\alpha)^2} \quad (3.7.3)$$

where $R_\alpha = \sqrt{(R_f R_b) T_{nr}}$, T_{nr} is the single pass transmission through the quantum wells alone), and R_f and R_b are the front and back reflectivities. The operation of the AFPM can be explained in the above expressions by seeing the reflection from a resonant device is zero under the condition that $R_\alpha = R_f$ or

$$T_{nr} = \sqrt{(R_f/R_b)} \quad (3.7.4)$$

When one of the states has zero reflectivity, one can achieve an infinite contrast. Figure 3.7.1 shows the contrast-VIO plot for a bias absorbing device

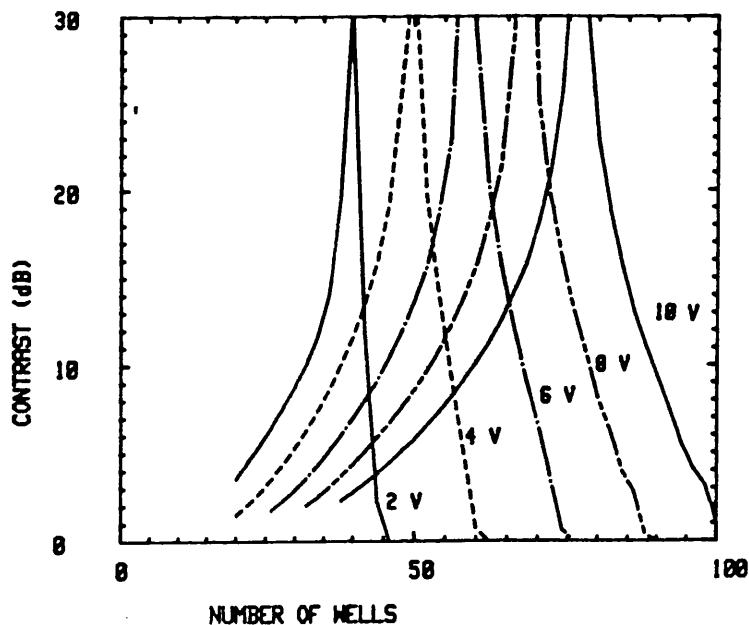


Figure 3.7.1 Voltage invariant optimisation curves for contrast in an AFPM. The modulator has 100 Å wells, a well width fluctuation of 1 monolayer rms and background doping of $2 \times 10^{15} \text{ cm}^{-3}$. Front and back reflectivities are 30 and 95 % respectively.

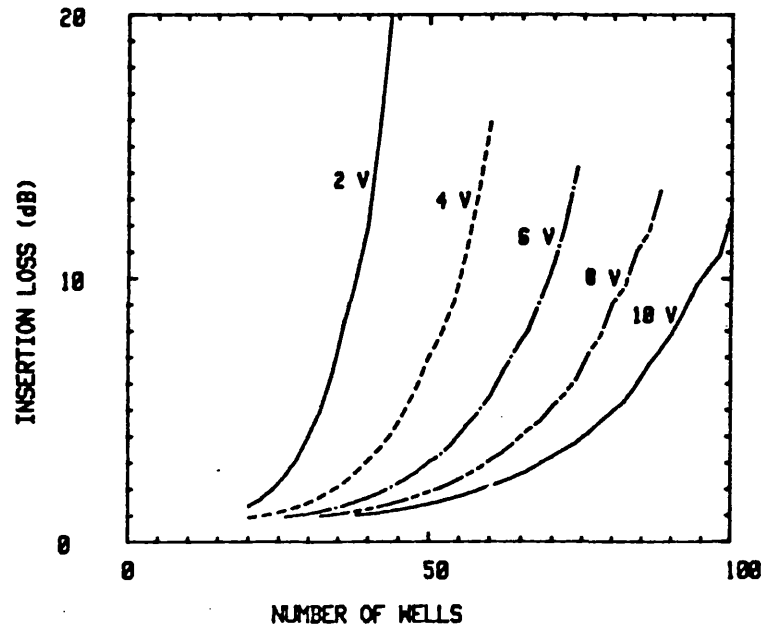


Figure 3.7.2 Insertion loss associated with the contrast-VIO curves of figure 3.7.1.

with 100 Å well width, and at all voltages there is this point of infinite contrast. However, at low voltages this point is achieved with very little shift in the exciton peak position, and hence the unbiased absorption is high. This unbiased absorption leads to a high insertion loss, as shown in figure 3.7.2. An operating voltage of ≈ 10 V is required to achieve the zero reflectivity in the off state while maintaining a insertion loss of less than 3 dB. However one need not work exactly at the infinite contrast peak, but with a reduced number of wells in the cavity. With only 2 V operating voltage and 28 wells it is possible to get 7 dB of contrast with an insertion loss of 3 dB.

In figure 3.7.3 instead of a contrast-VIO plot, we show the equivalent VIO plot for reflection change. Reflection changes approaching and exceeding 50 % are possible even at voltages as low as 2 V.

The bias-transmitting mode is not so effective as the bias absorbing one because the large residual absorption in the biased state leads to a large insertion loss.

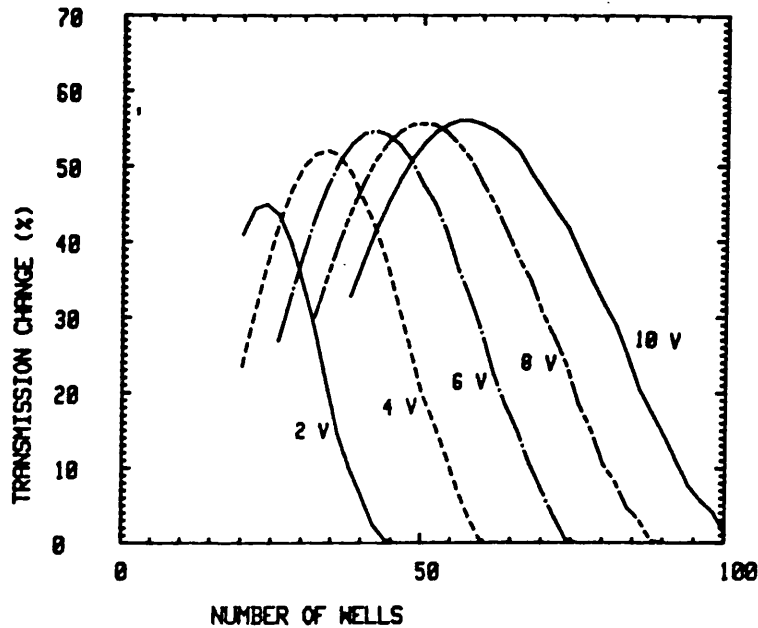


Figure 3.7.3 Voltage invariant optimisation curves for reflection change in an AFPM. The modulator has 100 Å wells, a well width fluctuation of 1 monolayer rms and a background doping of $2 \times 10^{15} \text{ cm}^{-3}$. The front and back reflectivities are 30 and 95 % respectively.

3.8 Comparison with Experimental Results

The results presented in this chapter all show broad agreement with published modulator results, although certain differences between the devices modelled and the real ones need to be accounted for. The most significant point to be stressed is in the non-resonant calculations for transmission modulators, no reflection is assumed on *either* the front or back (excluding reflection modulators) surfaces. Most of the published transmission modulators have uncoated back surfaces with 30 % reflectivity, and also some have residual reflectivity on the front surface. The 30 % reflection contributes to a larger insertion loss, but the residual front surface reflectivity adds Fabry-Perot oscillations which can enhance or degrade the modulation. In addition to the above considerations, different barrier widths alter the voltage required to produce a given field over a given number of wells. There are three published devices of differing well widths with good

antireflection coatings, with which it is worth making a quantitative comparison.

The 50 Å well width results can be compared to experimental data on a device of 75 wells of 47 Å width with 60 Å barriers [Stevens et al. 1988a], with a background doping close to $2 \times 10^{15} \text{ cm}^{-3}$. With 75 wells the modulator was an optimum one at a operating voltage of 16 V, with an accompanying transmission change of 35%. After dividing the experimental transmission change by 0.7 to account for the back surface reflection we find that the value of 34.3% compares very favourably with the theory.

Hsu et al. [1988a] have published results on a modulator with 200 periods of 100 Å wells and 100 Å barriers. The increase in barrier width from our value of 60 Å means that our equivalent voltages are 0.8 times smaller. Our calculations suggest that the background doping in that sample is about $6 \times 10^{14} \text{ cm}^{-3}$, and using this value we predict their device is an optimum one (for contrast) at 20 V where they obtain a contrast of 7 dB and an insertion loss of 5 dB in the bias absorbing mode (excluding back surface reflections). For the equivalent 16 V in figures 2.4.3 and 2.4.4, contrasts of 3 and 8.2 dB and insertion losses of 2.6 and 6.6 dB are found for doping levels of 2×10^{15} and 10^{14} cm^{-3} respectively. The experimental results, as expected, lie comfortably between the calculated ones.

Finally we compare the 150 Å well width results for the bias-transmitting mode with those of Whitehead et al. [1988b], a device with good anti-reflection coatings and composed of 45 periods of 145 Å wells and 60 Å barriers. With 2 V applied bias our model predicts that the transmission change should be 18.5%. After adjustment for back surface reflection the measured transmission change is 17 %.

3.9 Summary

The chapter started with a investigation of potential waveguide performance, and we showed that very good modulation is possible, but that the design was not so much dictated by the electroabsorption in the quantum wells, but external consideration such as coupling and compatibility with surrounding integrated components.

The physics of the electroabsorption plays a much more dominant role in the design of transverse devices, because of the conflicting requirements of

low operating voltage and long optical interaction length. We introduced the VIO plot as a means of choosing optimum device thickness for a given operating voltage. This technique forms the basis of a survey of achievable modulation in MQW diodes.

Initially non-resonant, bias-absorbing, 100 Å well width modulators were optimised for both greatest transmission change and greatest contrast. The effects of improvements in background doping (from 2×10^{15}) and well width fluctuations (from 1 monolayer rms) were then considered. Substantial improvements in modulation were only achieved in thick high contrast devices which required low background doping. As well as needing low doped material non resonant devices with high contrast (>10dB) also require high operating voltages and are necessarily associated with a high insertion loss.

The effect of different well widths was then considered. Narrower wells (50 Å) require greater operating voltages, although at these operating voltages a better modulation is achieved because the exciton retains its oscillator strength as it shifts. Lower well width fluctuation improves the narrow well width performance. In wells of 150 Å the bias-absorbing mode, while giving low operating voltages, does not provide good modulation, in part because of the rapid loss in oscillator strength with field, and also because of large field-enhanced broadening due to background doping.

The bias-transmitting mode has also been analysed, and with a well width 100 Å, achievable modulation is similar to that of bias-absorbing mode. For 150 Å well widths, the bias transmitting mode offers substantial improvements over the bias absorbing case, although the achievable transmission change is still similar to that for the 100 Å device.

Finally we have considered resonant designs such as the AFPM. This reflection device does provide significantly better modulation at lower voltage than non-resonant ones. In particular it can offer very high contrast operation at reasonable insertion losses.

The results presented are in good general agreement with the published experimental results, and in particular close quantitative agreement is found with three devices of 47, 100, 145 Å well width.

The model used and the results given in this chapter should enable the potential device user to see what design of MQW modulator might be suitable in a given application. However, many applications insist on low driving voltages and in table 3.9.1 we specify the expected performance of

both a non-resonant transmission modulator and and AFPM operating at 5V.

	Non-Resonant Transmission	AFPM
Well Width (Å)	100	100
Number of Wells	63	42
Well Width Fluctuation	1 monolayer	1 monolayer
Intrinsic Background Doping (cm ⁻³)	2x10 ¹⁵	2x10 ¹⁵
Operating Wavelength (nm)	860	860
Voltage (V)	5	5
Transmission Change (%)	31	53
Contrast (dB)	2.0	10
Capacitance (pf) {100 μm sq.}	1.1	1.7
Frequency (GHz) {50 Ω}	2.9	1.9
Optical Bandwidth (nm)	8	8

Table 3.9.1 Performance of a GaAs/(GaAl)As non-resonant transmission modulator and the AFPM at a 5V operating voltage.

Chapter 4

MODELLING FOR (GaIn)As/InP MATERIAL

4.1 Introduction

(GaIn)As/InP is the most developed alternative material system to GaAs/(GaAl)As for the growth of MQWs and it is likely to be important for long distance communications because its operating wavelength ($\approx 1.6 \mu\text{m}$) is close to that of the low loss window of optical fibres. Furthermore it is generally grown on InP substrates, the barrier rather than the well material, which is transparent at the modulator's operating wavelength. There is therefore no need to etch off the substrate in a transmission modulator, and any integrated electronics will not be affected by stray light directed at the modulator. In this chapter we extend the modelling carried out for GaAs/(GaAl)As to cover this material system.

4.2 Physical Modelling

We use (GaIn)As to mean $\text{Ga}_{0.47}\text{In}_{0.53}\text{As}$, the alloy composition lattice-matched to InP. However one of the most significant differences between (GaIn)As and GaAs quantum wells is the fact that the latter is a binary well material, whereas the former is ternary. This has two major effects: the average composition might vary from the lattice-matched composition, and hence QWs of the same well width can have different exciton wavelengths; and compositional fluctuations can occur within the device, giving a further inhomogeneous broadening mechanism.

For the above reasons the characterisation of (GaIn)As/InP is less developed than that of GaAs/(GaAl)As and there are many conflicting values reported for the band offset, effective masses and band non-parabolicities. We use a 40:60 conduction to valence band offset ratio, electron, heavy and light hole masses of 0.041, 0.377 and 0.085 for (GaIn)As and 0.079, 0.56 and 0.08 for InP [Bar Joseph et al. 1987, and Sauer et al.], and conduction band non-parabolicities of 3.96×10^{-18} and $3.43 \times 10^{-19} \text{ m}^2$ [Nelson et al., 1987a] for (GaIn)As and InP respectively. The heavy hole mass is the most important parameter since this dominates the size of the Stark shift and we choose the same values used by Bar-Joseph et al. [1987] who obtains reasonable agreement between experimental and theoretical shifts.

The binding energy as a function of well width is fitted from Hong and

Singh:

$$E_b^{hh} = 5.9 - 0.014 L_w \quad (4.2.1)$$

$$E_b^{lh} = 7.5 - 0.01 L_w \quad (4.2.2)$$

Figure 4.2.1 shows the zero field position of the heavy hole exciton as a function of well width assuming a perfect lattice match between well and barrier material. But as we have already pointed out, compositional variations in the quantum well can shift the exciton peak wavelengths. For instance, in the spectra of Bar Joseph et al., the unbiased exciton peak position for nominally 100 Å well is 1607 nm, leading to a well width estimate of around 150 Å by figure 4.2.1. The composition of the well is obviously Indium-rich. For this reason, rather than relying upon a single exciton wavelength of the $n=1$ subband transition, the characterisation of the well width is best done by measuring the energy difference between the $e1-hh1$ and $e2-hh2$ exciton transitions, dependent only on the difference in subband energies and not on the well material bandgap. Figure 4.2.2 plots this energy splitting against well width. The energy splitting of 123 meV in Bar-Joseph's spectra leads to the more realistic well width estimate of 94 Å.

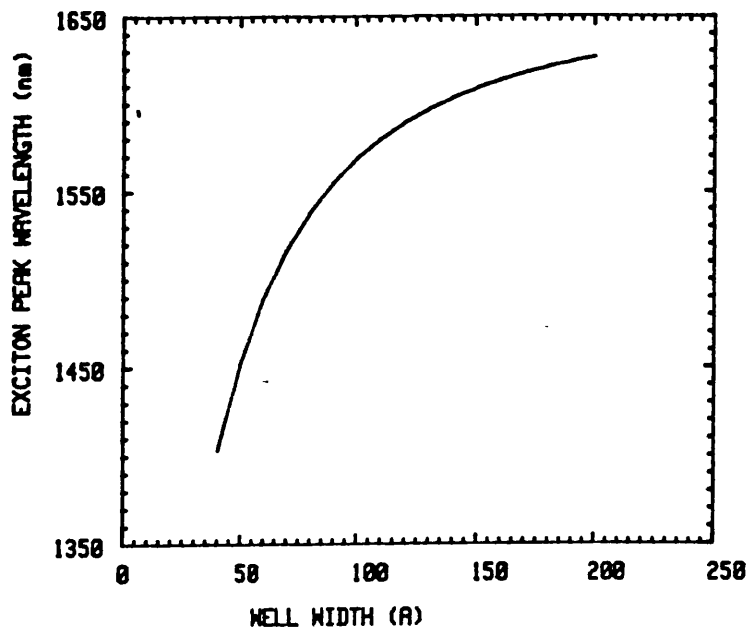


Figure 4.2.1 Wavelength of $e1-hh1$ exciton peak at zero field as a function of well width for the lattice-matched (GaIn)As/InP material system.

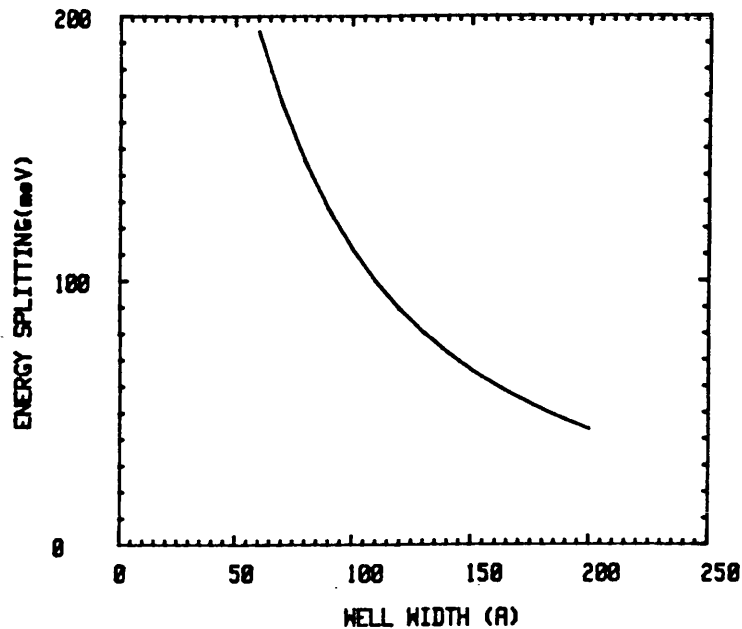


Figure 4.2.2 Energy splitting between e1-hh1 and e2-hh2 exciton peaks at zero field as a function of well width for the (GaIn)As/InP material system.

The absorption spectra are then calculated in the same way as for GaAs/(GaAl)As. The values for the absolute absorption in the continuum (α_{∞}) and the relative strength of the exciton (f_{ex}) are obtained by fitting to, and then averaging over, a number of published experimental results for well widths around 100 Å, as shown in table 4.2.1. In fitting these spectra it was found that some samples did not show as prominent a light hole exciton as predicted. This might be related to high values of strain within the samples.

A room temperature phonon broadening linewidth of 7.96 meV is derived from the temperature-dependent linewidth measurements by Weiner et al.. In addition to the phonon scattering, well width fluctuation and intrinsic background doping broadening mechanisms already described for GaAs/(GaAl)As, we add broadening caused by compositional fluctuations in the ternary well material. Assuming the same RMS well width fluctuation as that found in typical GaAs/(GaAl)As samples (1 monolayer) we estimate from published spectra [Bar Joseph et al. 1987, Shorthose et al., Tai et al.] that there is an additional compositional

GROUP	ABSORPTION OF CONTINUUM (α_{∞}) in cm^{-1}	RELATIVE AREA OF EXCITON (f_{ex})
Shorthose et al. [5]	6000	11 R_y
Tai et al. [6]	4300	12 R_y
Bar Joseph et al. [2]	3500	12 R_y
AVERAGE	4600	11.7 R_y

Table 4.2.1 Values of absorption of continuum level and relative area of exciton fitted to various experimental spectra with 100 Å well widths.

broadening of 7 meV which is significantly more than the theoretical minimum value of around 2 meV [Hong and Singh].

In figure 4.2.3 we plot the absorption spectrum for (GaIn)As/InP equivalent to figure 2.7.2 for GaAs/(GaAl)As, ie. for a diode with about 1 μm of intrinsic region with 100 Å wells and 60 Å barriers, 1 monolayer well width fluctuation, $2 \times 10^{15} \text{ cm}^{-3}$ background doping and a further 7 meV of compositional broadening. Note that while the absorption coefficient in the continuum behind the exciton peak is somewhat lower than that for the GaAs well material ($10,000 \text{ cm}^{-1}$ as opposed to 13000 cm^{-1}), the absorption at the heavy hole exciton peak is much lower ($10,000 \text{ cm}^{-1}$ as opposed to $22,300 \text{ cm}^{-1}$). The reduced prominence of heavy hole exciton is seen in most experimental spectra as well. The reasons are firstly that the relative area (f_{ex}) of the exciton is proportional to the Rydberg constant, which is reduced because of the lower effective masses in (GaIn)As. Secondly there is the additional 7 meV of compositional broadening. Furthermore in the (GaIn)As/InP material higher voltages are required to shift the exciton, because of the lower electron effective mass.

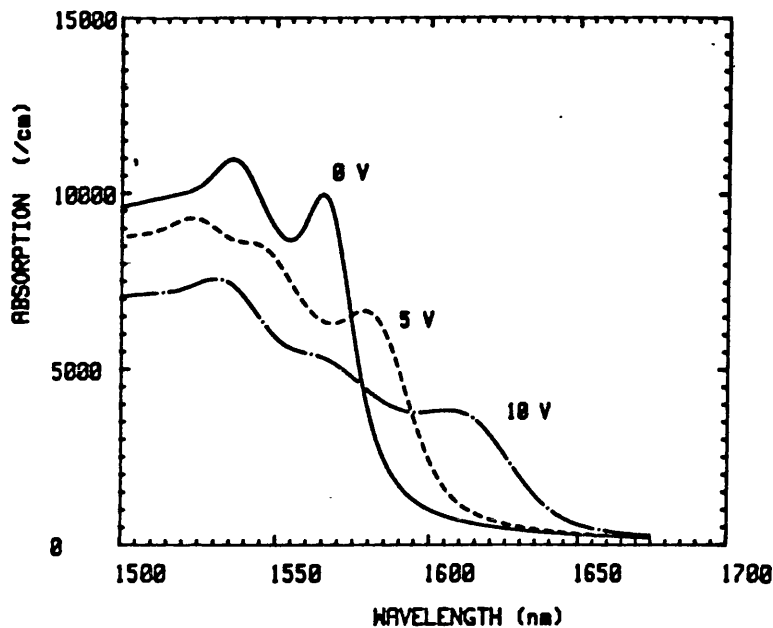


Figure 4.2.3 Calculated absorption spectrum for GaInAs/InP MQW diode composed of 63 wells of 100 Å with barriers of 60 Å thickness. The background doping is $2 \times 10^{15} \text{ cm}^{-3}$, the rms well width fluctuation 1 monolayer and compositional fluctuation broadening 7 meV.

4.3 Non-Resonant Modulator Modelling

For the (GaIn)As/InP device modelling we use exactly the same optimisation procedure as for GaAs/(GaAl)As. We use the calculation of absorption to evaluate the transmission through the device assuming perfect anti-reflection coatings on both sides of the device. We assume that a barrier of 60 Å is enough to keep the quantum wells isolated. In figure 4.3.1 we plot the VIO curves for the bias-absorbing mode. Note that 30 V is required to get the 30% transmission change typical of GaAs modulators with only 5 V operating voltages. This is because the lower absorption coefficient of GaInAs necessitates much thicker devices, with larger field variations due to background doping, and much larger voltages.

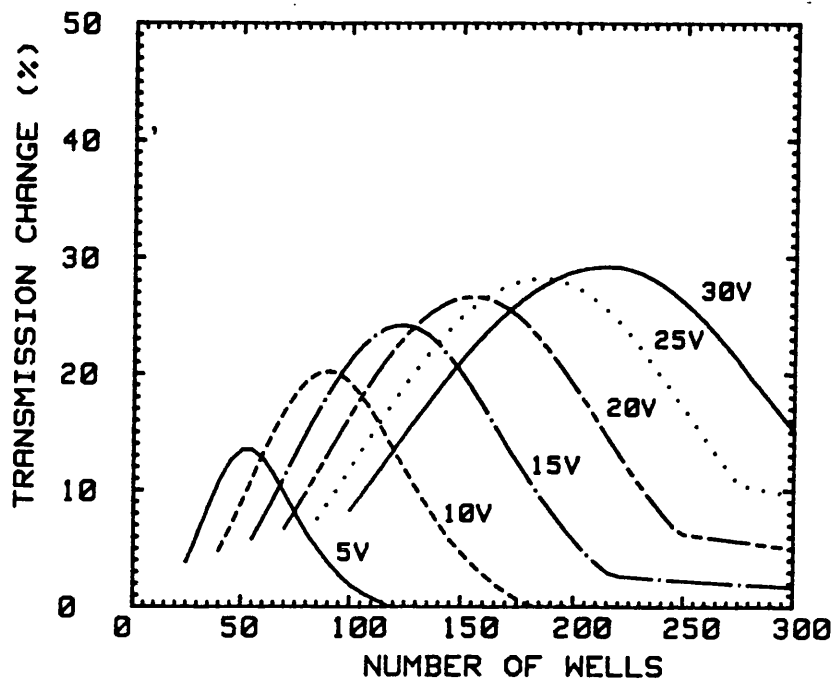


Figure 4.3.1 Voltage invariant optimisation curves for (GaIn)As/InP non-resonant bias-absorbing transmission modulator with a well width of 100 Å. Well width fluctuation is 1 monolayer rms, background doping is $2 \times 10^{15} \text{ cm}^{-3}$ and compositional fluctuation broadening is 7 meV.

In figure 4.3.2 we plot the optimum transmission change against design voltage for devices a) to e), as listed in table 4.3.1. Device a) has device parameters typical of what might be achieved with present day growth while devices b) to d) show the effects of improvements to the background doping, well width fluctuation and compositional broadening respectively. Device e) is for a non-resonant double pass reflection modulator.

We can compare these results with recent experimental results obtained by Guy et al. [1989] on a device with 150 wells of 100 Å with 100 Å barriers. To account for the different barrier sizes used in the modelling and the experiment one needs to scale voltages by 0.8. From figure 4.3.1, we predict his 150 Å device should be an optimum one at an operating voltage of 20 V, or 25 V with 100 Å barriers., and a transmission change of 33 % is expected. The measured value, after division by the back surface reflection, is 40 %. The difference can be explained by the presence of a slight Fabry Perot enhancement, and well as the seemingly better quality of material.

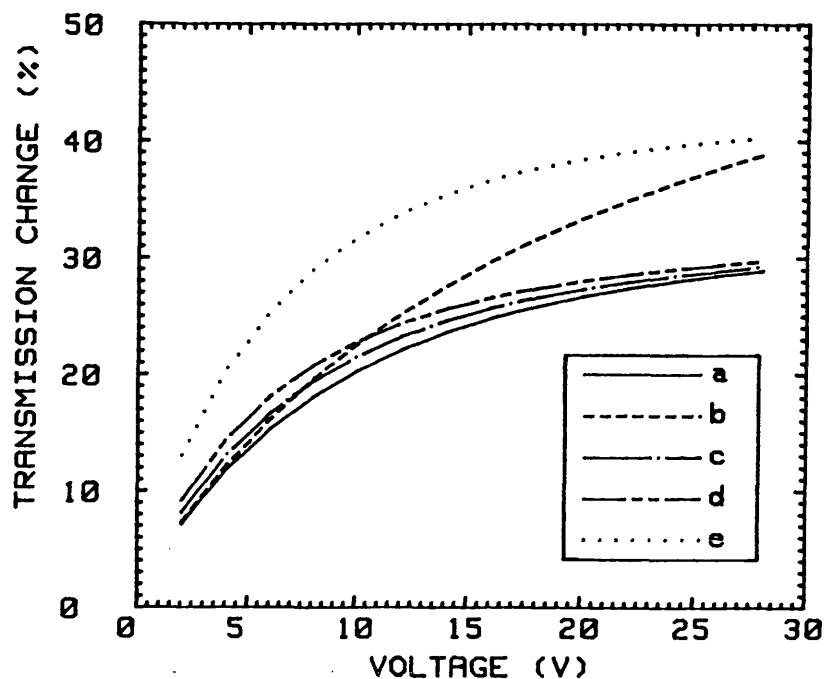


Figure 4.3.2 Optimum transmission change against operating voltage for (GaIn)As/InP non-resonant bias-absorbing modulators with 100 Å. Curves a) to e) represent modulators with differing material characteristics, as listed in Table 4.3.1

DEVICE	COMPOSITIONAL BROADENING	BACKGROUND DOPING (cm^{-3})	RMS WELL WIDTH FLUCTUATION	SINGLE/DOUBLE PASS
a)	7 meV	2×10^{16}	1 monolayer	single
b)	7 meV	10^{14}	1 monolayer	single
c)	7 meV	2×10^{15}	1/2 monolayer	single
d)	2 meV	2×10^{15}	1 monolayer	single
e)	7 meV	2×10^{15}	1 monolayer	double

Table 4.3.1 Device parameters for modulators investigated.

The bias-transmitting mode is expected to be less effective for (GaIn)As/InP MQWs since the heavy hole exciton is less prominent with respect to the continuum.

4.4 Resonant Modulators

AFPMs are being developed in the (GaIn)As/InP material, but it is still unestablished what performance they might provide. In figure 4.4.1 we plot the contrast-VIO plot for an AFPM in (GaIn)As/InP in the same way as we did for the GaAs/(GaAl)As material. Points of infinite contrast do appear, but they require more wells because the absolute absorption coefficient at the exciton peak is lower.

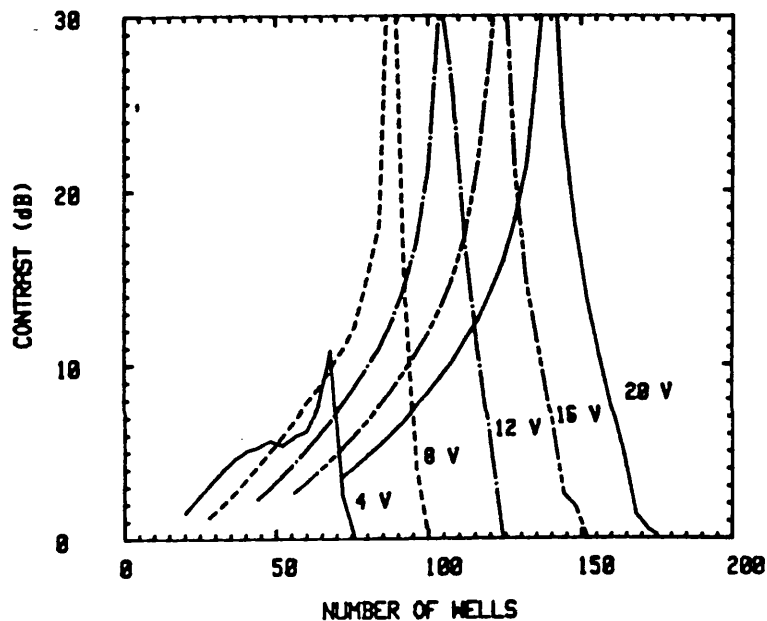


Figure 4.4.1 Voltage invariant optimisation curves for reflection change in an (GaIn)As/InP AFPM. The modulator has 100 Å wells, well width fluctuation of 1 monolayer rms, intrinsic background doping of $2 \times 10^{15} \text{ cm}^{-3}$ and compositional broadening of 7 meV. Front and back reflectivities are 30 and 95 % respectively.

Figure 4.4.2 show the associated insertion loss for the AFPM contrast shown in figure 4.4.1. These result show that low insertion loss operation of (GaIn)As based modulators do require much larger operating voltages than GaAs based ones. For instance to provide 10 dB of contrast with insertion loss of 3 dB one needs to operate device at 16 V rather than 5 V.

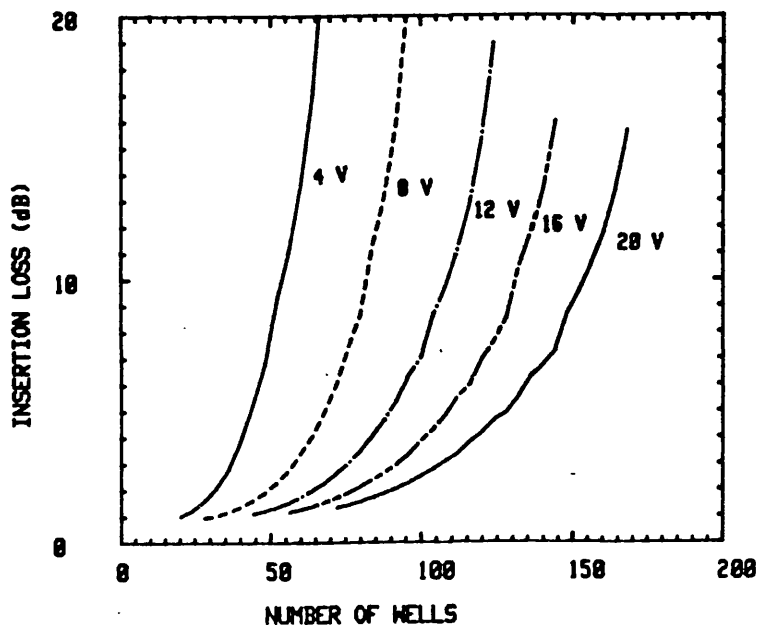


Figure 4.4.2 Insertion loss associated with the contrast-VIO curves of figure 4.4.1

4.5 Summary

The modelling of (GaIn)As/InP material is very similar to that of GaAs/(GaAl)As except the well material is ternary and thus there is both an uncertainty in its average composition and fluctuations in composition, which provide an additional inhomogeneous broadening mechanism. (GaIn)As/InP modulators seem to require significantly larger operating voltages than GaAs/(GaAl)As ones for a number of reasons: i) the absolute value of continuum absorption coefficient is slightly lower; ii) the relative magnitude of exciton area to continuum is lower; iii) additional broadening is caused by compositional fluctuations, and iv) smaller Stark shifts. Reasons ii) and iv) are both related to the lower electron effective mass. Typical performance of a (GaIn)As/InP non-resonant transmission modulator and AFPM are shown in table 4.5.1 below.

	Non-Resonant Transmission	AFPM
Well Width (Å)	100	100
Number of Wells	135	95
Well Width Fluctuation	1 monolayer	1 monolayer
Intrinsic Background Doping (cm ⁻³)	2x10 ¹⁵	2x10 ¹⁵
Operating Wavelength (nm)	1593	1610
Voltage (V)	15	16
Transmission Change (%)	26	45
Contrast (dB)	1.7	10
Capacitance (pf) {100 μm sq.}	0.56	0.8
Frequency (GHz) {50 Ω}	5.8	4.0
Optical Bandwidth (nm)	20	20

Table 4.5.1 Performance of (GaIn)As/InP non-resonant transmission modulator and AFPM.

The conclusions above suggest that a key parameter of interest in choosing a material system is the effective mass. Ideally for fibre-optic applications, one would like a well material of high effective masses, but with a band gap of around 0.8 eV. The only other suitable binary/ternary material system with such a well material bandgap is GaSb/(GaAl)Sb, and the effective masses for GaSb are very close to those of (GaIn)As [Carr et al.]. However, slight improvements in modulation should be possible through the use of quaternary material such as (GaIn)(AsP) [Zucker et al.] which do have higher masses and also give added flexibility of being able to shift the wavelength to 1.55 or 1.3 μm without narrowing the well width.

Chapter 5

APPLICATIONS IN FIBRE OPTICS

5.1 Introduction

In preceding chapters we have modelled the physics of the MQW electroabsorption effect, and gone on to analyse the optimum design of the modulator. Now an understanding of its operation and its likely performance has been achieved, we now go on to consider some of its potential applications.

In this chapter we consider the use of MQW modulators in fibre-optics. Optical fibres have already become the most effective means of communication over long distances, and yet we are still not utilizing the enormous communications bandwidth that they offer. Present limitations to the speed arise from linewidth broadening due to relaxation oscillations in lasers. If electroabsorption modulators offer 'cleaner' (lower chirp) modulation than lasers, and they can be integrated with CW lasers, they might be part of the transmitter of tomorrow's data links operating within the GBit/s regime. This possibility is explored in the first section of this chapter.

In the second section, we are no longer so concerned with obtaining the ultimate performance from the fibre. Instead we consider the use of the modulator in simple, but cheap architectures that utilise the functional duality of the MQW diode as both a modulator and a detector.

5.2 High Speed Fibre Optic Links

The response of all MQW electroabsorption modulators at low intensities has been limited by the capacitance of the devices and not by any fundamental physical mechanism which will remain when device dimensions are scaled down. It is hoped that this intrinsic speed can be used in a very high data rate fibre-optic link.

Direct modulation of a semiconductor laser's bias current is used in most present day fibre optic links, but at bit rates higher than 1 Gbits/s several advantages might arise from moving to an external modulator [Okiyama et al., 1987] : the potentially higher speed, the reduction of frequency chirp [Linke 1984,1987] and the possible increased cw power achievable when the modulation requirements on the laser are relaxed. The chirp is caused by the relaxation oscillations in the carrier density which consequently alter the

refractive index of the lasing material and hence the frequency of the mode. This linewidth broadening brings about significant dispersion in 1.55 μm low loss fibres [Nakagawa] and also excludes the use of direct modulation in amplitude and phase modulated coherent links. Dispersion shifted fibres would reduce the dispersion, but at increased cost.

The most developed form of external modulators are lithium niobate electro-optic ones that have recently been introduced commercially. An intensity modulator is implemented using a Mach-Zehnder arrangement and can exhibit very high speeds of up to 40 GHz when in a travelling wave form with an operating voltage of 7.5 V [Dolfi et al.]. However, the large length of these devices and the need for titanium diffusion to define the waveguide make it difficult to manufacture them reproducibly. Recently there has been a drive to develop modulators in III-V materials, both for greater ease of manufacturing and, perhaps more significantly, the possibility of monolithically integrating them with laser sources, photodetectors and associated electronics.

Intensity modulators in III-V materials can be realised in two forms : through the use of a phase modulator in a Mach-Zehnder or coupler configuration or through electroabsorption. The phase modulation of the first of these can be achieved either through the electro-optic effect [Walker] or the larger electrorefractive effect closer to the bandgap [Alping et al. 1986a,1986b]. The electroabsorption modulator is a simpler alternative and the waveguide geometry is preferred because it offers integration with normal laser types. The monolithic integration of the modulator with a laser has already been achieved by Tarucha and Okamoto who used the same MQW layers for both devices. The lasing wavelength is shifted past the zero bias exciton peak in the modulator by the band gap shrinkage caused by the high carrier density in the laser's active region.

Unfortunately the electroabsorption effect is accompanied by an electrorefractive effect which also gives rise to chirp. The instantaneous frequency of the output signal from the modulator is [Koyama and Iga, 1988]

$$f = f_0 + (\alpha/2)(1/I) dI/dt \quad (5.2.1)$$

where α is often referred to as the alpha-parameter:

$$\alpha = \Delta n / \Delta k \quad (5.2.2)$$

and f_0 is the input frequency, I the output intensity, Δn the field-dependent change in refractive index and Δk the change in extinction coefficient.

It should be noted that the frequency changes only while the output intensity is also changing and therefore with a square waveform little chirp will be present. Mozer reached similar conclusions when considering the drive for a semiconductor laser but the absence of relaxation oscillations in electroabsorption modulators makes these ideas more realisable.

One further point to make is that α changes with wavelength and at one particular wavelength is zero. This is true for both bulk [Bennett and Soref] and quantum well [Nagai et al., Yamamoto et al.] materials and it is thought that very low chirp will be seen at this wavelength. However this wavelength is very close to the exciton peaks and it might not be possible to achieve practical low insertion loss devices here.

Practical demonstration of low chirp in a bulk material electroabsorption modulator integrated with a laser have been demonstrated by Okiyama et al. [1989] who, using a bulk material modulator integrated to a DFB laser, succeed in showing that the allowable dispersion (230 ps/nm) is 5 times greater than for the direct drive of DFB laser in a 10 GBit/s link.

5.3 Novel Fibre-optic Architectures

All commercial fibre-optic systems installed to date are simple one-directional links with an LED or laser source at one end and a photodetector at the other. However the fact that the MQW modulators also act as photodetectors lends one to consider its application in novel architectures that use this functional duality.

i) *Bidirectional Link*

The main costs of a fibre-optic link are the physical laying of the cable, the cable itself and its splicing and connection costs. There are obviously major savings to be made if one can use the same cable for transmission in both directions. The length of this type of link is restricted by the backscatter and reflections from the fibre and thus they will probably be limited to short-distance links, where cost is likely to be the most important concern. The requirements for such a link would typically be a length of less than 5 km

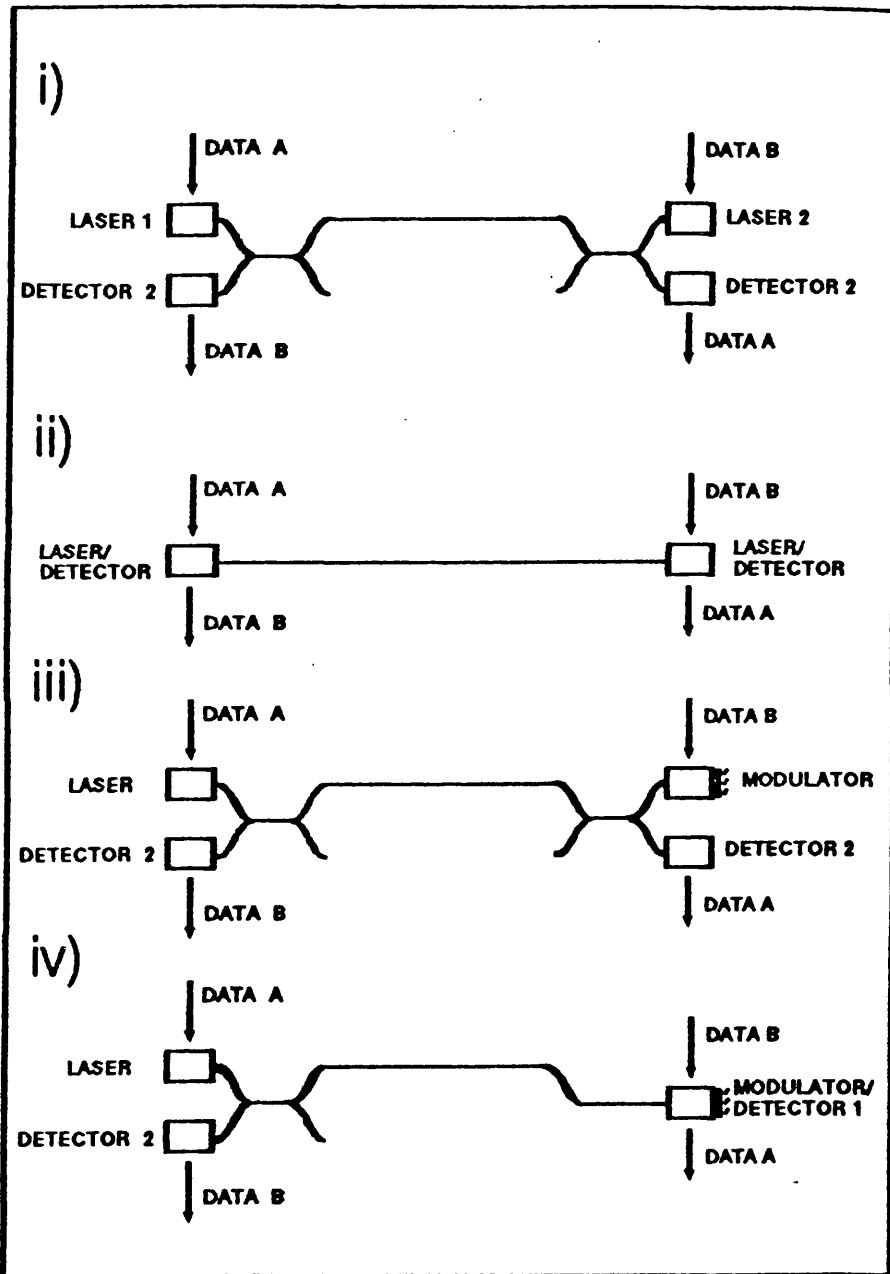


Figure 5.3.1 Bidirectional fibre-optic architectures

and a data rate of 100 Mbits/s, such that compressed and coded high definition television transmission [Gaggione and Le Gall, Ninomiya et al.] would be feasible.

Several other bidirectional architectures have been suggested and these are summarised in figure 5.2.1. The most obvious architecture is system i) which has a transmitter and a detector attached to the fibre at each end. Either a coupler or a filter (for WDM) splits/directs the light at each end. This form of link has been demonstrated for both analogue [Ozeki et al.] and digital transmission [Kawasaki et al., Coombes 1987, Westlake and O'Mahoney].

The large number of components can be reduced by utilising the dual functionality of laser/LED structures as both optical sources and detectors [d'Auria et al., Alping and Tell 1984] as shown in system ii). No couplers or beamsplitters are required. This type of link can only operate in a half-duplex mode with information being transmitted in one direction only. Furthermore it is inevitable the performance of the laser/photodetector will be compromised compared to the single function devices.

System iii) is a reflective-modulator link which dispenses of the requirement of having a laser at each end of the link [Wale et al.]. Indeed it is even conceivable that the same laser might be used to supply power to several such links. System iv) is the architecture of Wood et al. and is really a hybrid of ii) and iii) in that both functional duality and reflective modulation are used. In place of the MQW modulator the use of an optical amplifier has also been used for modulation by Olsson and Buhl. However the transverse MQW modulator is still attractive because of the ease of coupling into it and the fact that no polarization control is necessary.

Wood's bidirectional architecture is almost ideally suited to the AFPM, which not only modulates well at low biases, but also makes a very high quantum efficiency photodetector.

A typical power budget for a MQW modulator link is shown in table 5.3.1. Typical PINFET receivers have a bit error rate of 10^{-9} with a -40 dBm input power at 100 Mbit/s and thus on these considerations alone there is an adequate system margin at both of the considered wavelengths. Note that the use of the 1550 nm saves 14 dB in signal power over the 5 km distance, outweighing any lowering of the achievable modulation in the longer wavelength materials. Indeed the performance of the system is not

Power Budget	1550 nm	850 nm
Laser Power	3 dBm	
Laser to Fibre Coupling	3 dB	
Coupler	3 dB	
Fiber losses (5 km)	1 dB	(8 dB)
Fibre to Modulator Coupling	1 dB	
Splicing etc.	1 dB	
	-6 dBm	(-13 dBm)
Transmission Change in Modulator	3 dB	
Modulator to Fibre Coupling	3 dB	
Fiber losses (5 km)	1 dB	(8 dB)
Coupler	3 dB	
Fibre to Detector Coupling	1 dB	
Splicing etc.	1 dB	
	-18 dBm	(-32 dBm)

Table 5.3.1 Power budget for bidirectional link using reflective MQW modulator/detector.

sensitively dependent upon the modulator performance, but rather determined by the coupling losses from fibre to device and from device back to fibre. There is however one other limitation to the system: Wood et al. [1986] has found that the performance was limited by noise resulting from coherent interference between the light from the modulator and light backscattered and reflected from other parts of the link. This noise has been named coherent Rayleigh noise (CRN) and the amount of noise current

generated in the receiver is [Wood et al 1988a]

$$\langle \delta i^2_{\text{CRN}} \rangle = \left(\frac{\eta e \lambda}{hc} \right)^2 \frac{P_{\text{bs}} P_s}{8\pi} \tan^{-1}(B_w / \Delta f) \quad (5.3.1)$$

where P_{bs} is the backscattered light, P_s the signal reflected from modulator and received at the source end, η the quantum efficiency of the photodiode, B_w the bandwidth of the receiver and Δf the linewidth of the laser. The rms signal to noise ratio is thus given by

$$K_{s/n} = \frac{[8\pi P_s]^{1/2}}{[P_{\text{bs}} \tan^{-1}(B_w / \Delta f)]^{1/2}} \quad (5.3.2)$$

Assuming a signal to noise ratio of 20 is required [Gowar: for Gaussian signal independent noise] we can calculate a limit to the backscattered light:

$$P_{\text{bs}} < \frac{0.063}{\tan^{-1}(B_w / \Delta f)} P_s \quad (5.3.3)$$

Given typical values for a single-mode non-DFB laser of $\Delta f = 100$ MHz and $B_w = 50$ MHz, the expression shows that the backscattered light must be at least 8.6 dB down upon the signal power. This requirement is relaxed if one can broaden the laser linewidth. Wood et al. [1986b] did precisely this by adding a small amplitude, high frequency dither signal to the drive of the source laser.

ii) Fibre Optic Chain

MQW diodes can also be used in the design of more extended networks. The application is a similar one to that described above: a cheap local area network operating at about 100 Mbits/s. Consider a chain of modulators linked by optical fibres with lasers at either end as shown in figure 5.3.2. Any one modulator can send information to any of the others acting as photodetectors. Lasers at either end of the chain source the light and, depending upon the direction of information flow, only one of them is on at a given point in time.

The worst case is when the diode at the end of the chain wants to receive a signal derived from the laser at the opposite end of the chain. The 'AC'

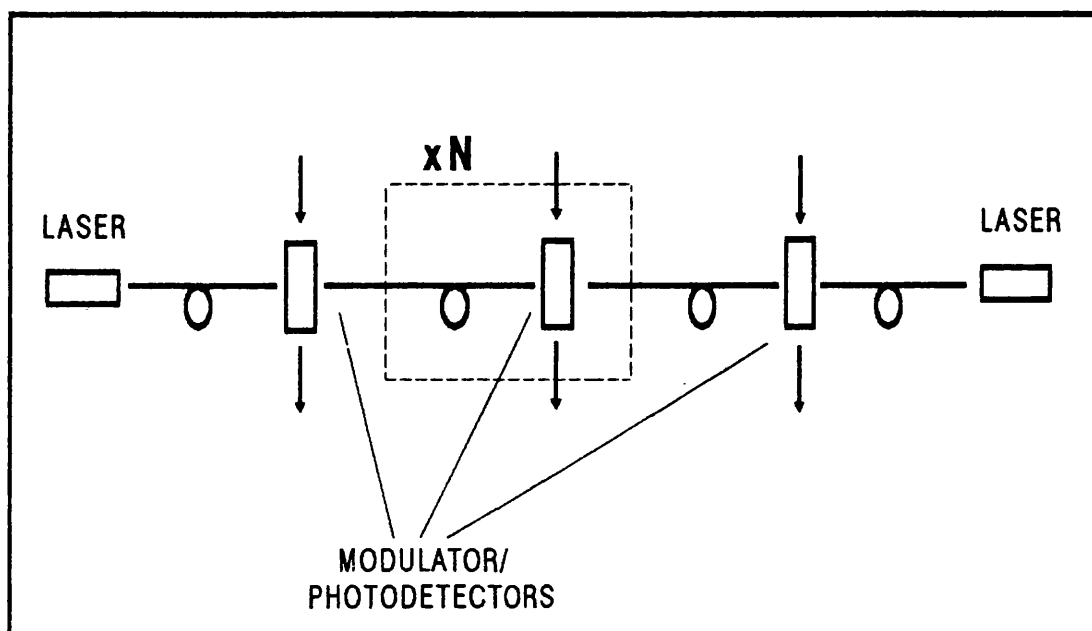


Figure 5.3.2 Fibre-optic chain network using MQW diodes as modulators/photodetectors.

signal reaching the end diode is

$$P_s = P_{\text{las}} \Delta T C_{\text{fm}}^N T_{\text{HI}}^{N-2} C_{\text{mf}}^{N-1} \exp(-\alpha_f l_f) \quad (5.3.4)$$

where C_{fm} and C_{mf} are the coupling losses from fibre to modulator and modulator to fibre respectively, T_{HI} is the basic insertion loss of the modulator due to residual absorption in the MQWs, α_f is the absorption in the fibre and l_f is the total length of fibre.

If we assume that all of the absorbed photons generate a photocurrent then the quantum efficiency of the MQW diode as a detector is $1-T_{\text{LO}}$ then the received signal is proportional to $\Delta T T_{\text{HI}}^{N-2} (1-T_{\text{LO}})$. Since the insertion loss is raised to the power of $N-2$, the principal requirement of the modulator in this application is a low insertion loss.

The number of nodes that can be inserted into the chain is limited by the total fibre-modulator-fibre insertion loss ($C_{\text{fm}} T_{\text{HI}} C_{\text{mf}}$). In most cases this total loss is likely to be dominated by the coupling losses. Transverse modulators offer easier coupling and so are preferred to waveguide ones for this type of application. In principle either transmission or reflection modulators could

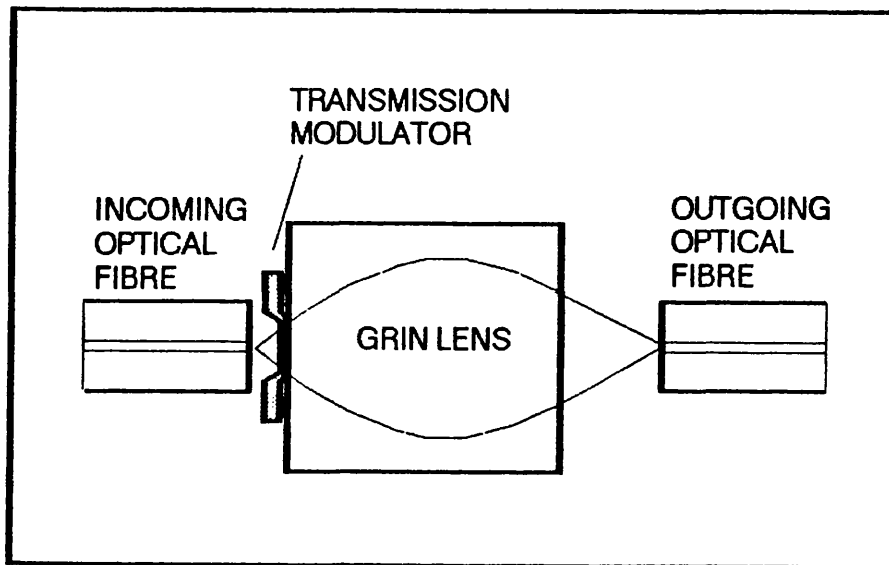


Figure 5.3.3 Grin lens mount for modulator for coupling MQW transmission modulator to fibres.

be used. In *transmission* modulators the incoming and outgoing fibres are positioned on either side of the device. To couple the light into the fibres, we propose two novel techniques: i) the mounting of the modulator on a GRIN lens in the way shown in figure 5.3.3. The only high precision adjustment needed is therefore the positioning of the output fibre in the focus of the grin; and ii) the use of optical fibre up-tapers. These up-tapers [Presby et al.] have been recently developed and are expansions of single mode fibres to core diameters of around $100\ \mu\text{m}$ so that the beam divergence at the output is reduced to a few degrees. Such a beam might readily pass through the modulator and enter the other fibre with relatively little insertion loss.

One advantage to using *reflection* modulators is that there is no need to provide optical access to the back surface. Thus temperature control and mounting the device closer to the electronic circuitry will be much easier. On the other hand, this is balanced by a more difficult optical design. Various methods of coupling are possible: i) off-perpendicular incident fibres and separate small focusing lenses; ii) a corner reflector (or back to back beamsplitters) and lens arrangement as shown in figure 5.3.4; iii) a polarization beamsplitter and quarter wave plate similar to the optics

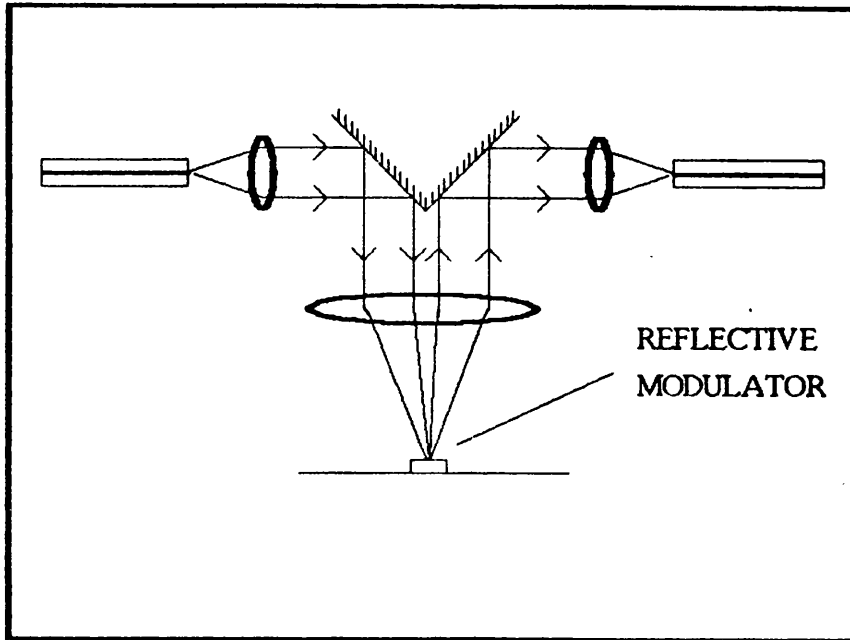


Figure 5.3.4 *Method of coupling light into MQW reflective modulator through the use of a corner reflector*

used in a compact disc optics (requires polarization control on input); and iv) the use of a fibre coupler to split light after it has entered the fibre. The coupler would introduce an unavoidable 6 dB insertion loss, and multiple reflections might become a problem.

With $T^{\text{HI}} = 1$ dB and taking other values from table 5.3.1 for the bidirectional link, one finds that with seven modulators and a total of 30 km of fibre the received power at 1550 nm is still detectable at -36 dBm. The total fibre-modulator-fibre insertion loss of 5 dB is probably an overestimate of what is feasible and hence there is scope for a greater number of modulators.

Finally we briefly mention that in the applications envisaged here, temperature stabilisation probably will be required since the modulators might be in differing environments. The temperature sensitivity of the MQW modulator will be discussed in chapter 6.

5.4 Summary

The electroabsorption mechanism offers relatively clean high speed modulation when compared to direct modulation of laser diodes, because of the absence of relaxation oscillations. Thus the smaller linewidth enhancement enables data to be sent further before significant dispersion takes place. Major goals needing to be attained before practical realisation of this application include the integration with a laser source and increasing the device saturation power.

Alternative novel architectures for the MQW modulator rely upon a remote, perhaps distributed, laser source. The dual functionality of the MQW diode as modulator and detector reduces the number of components required, and hence the device might play an important role in a local area network. A bidirectional loop is assessed, and we calculate limits for the back-reflected light that coherently interferes with the signal. Then we propose a fibre-optic chain architecture. In both instances, the use of long wavelengths is beneficial despite lower achievable modulation in the devices. In fact the device modulation in general plays a relatively minor role in defining system performance, with coupling losses likely to dominate the design. To this end, several different methods of mounting the modulator have been proposed.

Chapter 6

MQW MODULATORS FOR OPTICAL INTERCONNECTS

6.1 Introduction

The interest in optical interconnects has arisen from a growing awareness of the importance of communication between devices in limiting the overall performance of electronic circuits and the realisation that this limitation is unlikely to be overcome by purely electronic means. Optics has already demonstrated its superiority over electronics in long distance communications where the low loss and dispersion of optical fibres have led to their introduction in most long haul links. It is the purpose of this work to investigate the practicalities of using optics for much shorter interconnections deep within the fabric of electronic circuitry.

Electronic interconnection can be broken into three types: intrachip, interchip over a printed circuit board (PCBs) and from board to board over the backplane. In all cases these consist of a metallic track or link with an associated capacitance and resistance. In lines of relatively small length the driver resistance exceeds the line resistance and the rise time is proportional to the length of the line through the increasing capacitance. But in longer lines, the line resistance starts to exceed the driver resistance, and the delay becomes a diffusive one proportional to the square of the length [Mead and Conway]. This becomes a serious limitation to the link length. The capacitance not only limits the speed but requires a significant amount of energy which can be as large as the switching energy of the devices used [Goodman et al., Miller, D.A.B., 1989]. The bandwidth of the link can be increased by using a transmission line, but in this case matching to the line characteristic impedance must be carried out at each termination. Since characteristic impedances are unchanged when shrinking the geometry and are generally in the range 10-100 Ω , considerable power is dissipated in these matching resistances. Furthermore, while the transmission line increases the bandwidth, there is always a data delay associated with the finite speed of propagation of the electromagnetic field.

An optical interconnect potentially offers the following features [Goodman et al., Wu et al.]: i) The bandwidth of optical media is enormous and the data rate of a link will be determined by the electronic/optical transducers and not the medium itself, ii) the data delay might be improved although long free space paths would introduce significant delays, iii) a reduction of the pinout required for each chip, iv) access to the centre of the chip, v) the transmitter and receiver circuit are electrically isolated and vi) a reduction in

the power and space devoted to driver and receiver circuits. This final point relies upon the efficient transfer of charge that an optical medium can provide. Quantum well modulators can modulate an optical beam with low currents (a photon absorbed produces one electron in photocurrent), while p-i-n detectors efficiently convert the optical signal back into electrons. Optical fibre or even a simple lens can guide the light over large distances without large losses. This contrasts with electrical links where one either needs to charge up the line capacitance, or one needs to dump large amounts of charge into matching impedances for the transmission lines [Miller, D.A.B., 1989].

There are other more 'philosophical' advantages of free space optics: an extremely large number of different signals can pass through a small volume without interacting with one another, and the two dimensional nature of the information flow. This suggests that a very large degree of connectivity is possible giving rise to new 'highly parallel' architecture that might, for instance, overcome the Von Neumann bottleneck between the central processor and memory. However, practical realisation of such a high level of connectivity will be dependent upon the prior introduction of more limited interconnects, primarily high bandwidth links, and it is this type that shall be investigated in this chapter. A circuit well suited to the implementation of such an optical interconnect is a telecommunications switch. Within the switching fabric high bandwidth optical signals need to be routed to different ports, with the interconnections tending to be very regular and symmetric [Midwinter].

Practical demonstrations of optical interconnect technology are still at an early stage. Kostuk et al and Wu et al. have both investigated the use of reflective holograms for optical imaging, with diffraction efficiencies of 20% and spot sizes of $\approx 75 \mu\text{m}$. Brenner and Sauer suggest that more flexible connections are possible with two-tiered diffractive-reflective holograms. Wu et al. have demonstrated an array of detectors and associated simple receivers compatible with CMOS. Tsang has demonstrated the direct drive of a laser from GaAs logic at 1 Gbit/s, and efficient transfer to a simple receiver using a compact disc lens.

Comparisons of electrical and optical interconnects using LEDs and lasers have already been presented by Kostuk et al. and Feldman et al.. Kostuk et al. conclude that for intrachip distances of around 1 mm, the line capacitance is low enough (70 fF) that an optical link is uncompetitive in terms of power

dissipated. On the other hand, for an interchip link, the main contribution towards the capacitance is from the bonding pads (0.4 pF each), large enough to bring the electrical and optical link into much closer competition. Feldman et al. have considered the design of an intrachip link in greater detail, taking both the capacitance and resistance of the metallic line into account, as well as considering different bandwidths, fanout and scaling down effects. They demonstrate that above a certain break-even line length the optical link uses less power, and this line length is of the order of 1 mm at 1 Gbit/s and decreases with increasing bandwidth and fanout. Feldman et al. also briefly consider the use of MQW modulators in optical interconnects and show that they offer smaller break-even line lengths than a laser, especially at the smaller bandwidths (<500 MB/s) where the laser threshold power tends to dominate the power dissipated in the optical interconnect.

For the type of comparisons described above the authors make certain assumptions such as the size of detector, the optical path losses, the threshold current and efficiencies of the laser source. Perhaps most significantly they chose to assume no signal gain in the receiver circuit. The purposes of this chapter is to clarify certain trade-offs in the design of the optical link and to point out the practicalities that need to be addressed in implementing the designs.

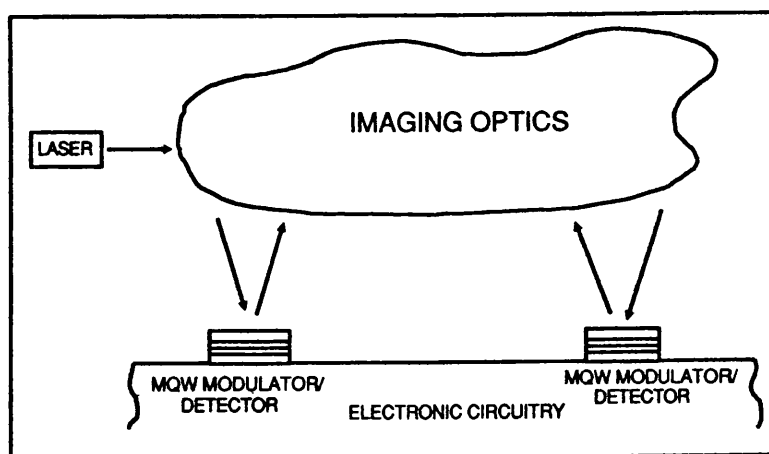


Figure 6.1.1 Schematic diagram of optical interconnect showing MQW modulators/detectors integrated with electronic circuitry.

The sort of optical link we shall consider is shown in figure 6.1.1. An off-chip laser source is imaged onto a reflective modulator. The reflected signal from the modulator is then imaged onto a detector. The detectors can be MQW modulators acting in their detector mode, although it would be equally feasible to have dedicated photodiodes. The concern of this document lies in the design of the optical/electronic interfaces and not with the optical path itself. Furthermore, we make the a priori assumption that the integration of the MQW modulator and electronic circuitry, by monolithic integration or flipchip technology, is both possible and economic.

6.2 Transmitter Design

In this work we have chosen to concentrate upon the use of MQW modulators in the optical interconnect. There are two main advantages of using modulators in preference to directly modulated lasers: i) a single laser can drive several modulators and hence the power needed to achieve the lasing threshold is spread out between several links; ii) the power required to generate the optical signal is kept off the chip. However let us briefly consider the option of using a laser in more detail.

The lasers which could be used for direct modulation in this case would need to be surface emitting ones, either with vertical cavities [Kinoshita and Iga, Koyama et al.], or waveguide lasers with slanted mirrors or gratings [Noda, S. et al.]. The main disadvantage with the use of on-chip lasers is that of providing the power to take the laser above threshold. The power required is:

$$P_I = V_{fb}(I_{th} + eP_{las}/\eta_{dif}E) \quad (6.2.1)$$

where V_{fb} is the forward bias voltage, I_{th} is the laser threshold current, e is the electronic charge, P_{las} is the optical power emitted, η_{dif} is the laser differential quantum efficiency, and E is the photon energy. When this power is a similar order of magnitude to the optical power signal required, the laser starts to appear a more attractive transmitter. With $V_{fb} = 1$ V and $I_{th} = 30$ mA, there is a power loss of 30mW before any signal is sent. However, Jewell et al. have recently reported optically pumped lasing in single quantum well vertical high finesse cavities, and predicted electrically

pumped threshold current is $<10 \mu\text{A}$ for a $1 \mu\text{m}$ device. With thresholds below 1 mA , the surface emitting laser would start to look an attractive option.

The MQW electroabsorption modulators on the other hand already appears well suited to the transmitter: they can be made to be high speed, their optical bandwidths are compatible with semiconductor lasers, the normal incidence devices are easy to couple into and they can be made in a reflective form so that transmission through the substrate can be avoided. The low voltage operation and the high modulation of the AFPD makes it an attractive device for this application. Since optical fibres, if used at all, will be of short length, there is little advantage in using the longer wavelength materials, and GaAs/(GaAl)As will be the preferred material system.

However, there are two problems that must be addressed before the AFPD can be used. The first is its temperature sensitivity. As the Fabry Perot resonant wavelength and the bandedge shift by different amounts with temperature, resonant modulators only function within a limited temperature region. This will be considered in the next section. Secondly the modulation becomes dependent upon the incident angle.

We briefly address the effect of incident angle by calculating the shift in the cavity resonance wavelength with angle, ignoring effects of the angle upon the reflector stack. This should be an acceptable approximation since the bandwidth of the stack reflectivity is much larger than that of the Fabry-Perot resonance.

Figure 6.2.1 shows light at incident angle θ_i on the modulator. In order to be in its resonant state the path length difference between the back and front surface reflections (shown by bold lines) needs to be an integral number (m) of wavelengths:

$$2t n_2 \sec\theta_t - 2n_1 t \tan\theta_t \sin\theta_i = m\lambda \quad (6.2.2)$$

where n_1 and n_2 are the refractive indices of the two materials, and t is the thickness of the cavity.

The normal incidence resonant wavelength is determined by

$$2t n_2 = m\lambda_0 \quad (6.2.3)$$

Using the above expression together with Snell's law we can rearrange

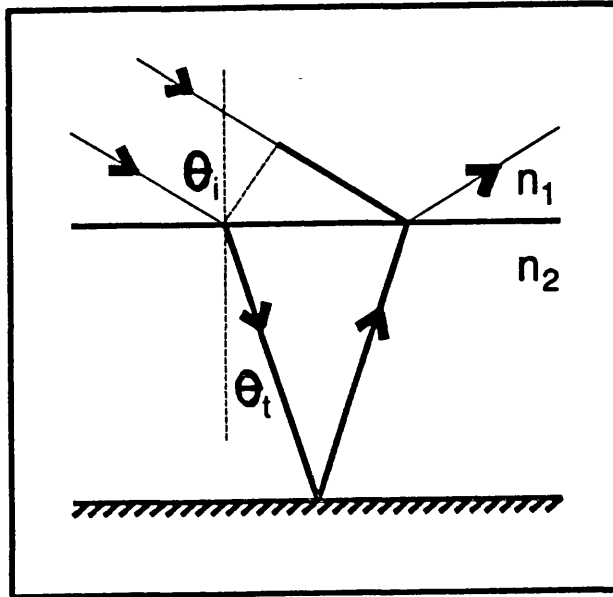


Figure 6.2.1 Back- and front-reflected rays in a AFPM structure. At the resonant wavelength, the path difference between them must be an integral number of wavelengths.

expression (6.2.2) to find that

$$\lambda/\lambda_0 = \{1 - (n_1/n_2)^2 \sin^2 \theta_i\}^{1/2} \quad (6.2.4)$$

We plot this function in figure 6.2.2, assuming a normal incidence resonant wavelength of 860 nm. The variation, while significant, is not so large as one might initially expect because at large incident angles, the angle of the transmitted ray is smaller because of the high refractive index of the cavity material. The tolerance to changes in incident angle will depend upon whether one wants to maintain the contrast, or the reflectivity change, since the contrast is sensitive to relative changes in the low reflectivity state, while the reflectivity change depends only upon its absolute difference with the high-reflectivity state. Thus to maintain a contrast of 10, the resonant wavelength should shift less than about 1/10 of the resonant linewidth, whereas to maintain the reflectivity change the equivalent shift is about 1/2 of the linewidth. If we allow a change of $\pm 1/6$ of the resonance linewidth (≈ 20 nm), we calculate a range of 0 to 25° can be tolerated. The modulator can be design to work at a specific angle off normal incidence, but the

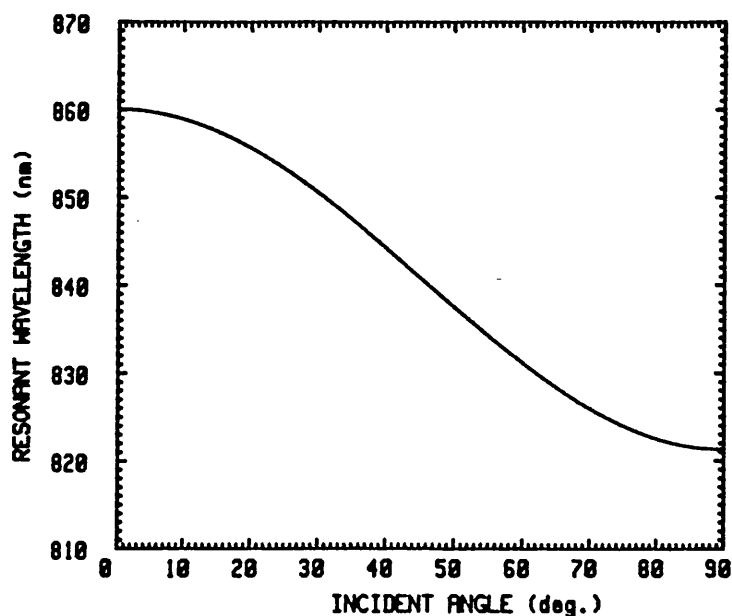


Figure 6.2.2 Resonant wavelength against incident angle for Fabry-Perot modulator. Note that a given change of angle well off normal incidence can shift the resonance much more than the same angular change near normal resonance.

modulator becomes more sensitive to angular changes: at 45° the range is only $\pm 5^\circ$.

Finally lets us consider what requirements there are for the driving circuitry for the modulator. Not only must it provide the correct voltage swing, but also current for i) charging and discharging the capacitance of the modulator, and ii) the photocurrent generated by the absorbed photons in the biased state. Thus the saturation current of the driving transistor should be at least

$$I_{\text{sat}} > 2BC_m V_m + e(1-T_{LO})P_m/E \quad (6.2.5)$$

where B is the bit rate, C_m is the modulator capacitance and V_m is modulator voltage, e is the electronic charge, T_B is the transmission in the biased state, P_m is the optical power incident upon the modulator and E is the photon energy.

6.3 Temperature Sensitivity of Modulators

One of the main practical considerations in using an MQW modulator in a real system is its sensitivity to changes of temperature. In this section we quantify this sensitivity and draw conclusions for the integration of the device with electronic circuitry.

The temperature range specified for electronic components is generally -20 °C to 80 °C with military requirements being even more stringent (-50 °C to 125 °C). Optoelectronic components are unlikely to match these specifications and it is therefore very important to account for thermal effects when designing an integrated opto-electronic circuit.

In the case of the electroabsorption modulator one of main effects of temperature is the shift of the subband edge with temperature [Iwamura et al.]. This tends to shift the optimum operating wavelength of the modulator. The fixed wavelength temperature variation (FWTV) gives the tolerable temperature range when the source wavelength is fixed. The scanning wavelength temperature variation (SWTV) is the working temperature range when the source's wavelength tracks that of the modulator.

We consider separately the temperature response of the non-resonant modulators and the resonant ones such as the AFPM.

Non-resonant Modulator

In a non-resonant electro-absorption modulator the temperature dependence of the refractive index is unimportant. Hence the sensitivity of the absorption spectrum is the only temperature dependent effect.

The effective masses and hence the subband energies of the quantum well material are relatively insensitive to temperature [Sarkar et al.], and hence temperature dependence of the absorption spectrum arises from two sources: i) the variation of the well material bandgap, and ii) a change in the phonon broadening. The former just shifts the wavelength of optimum operation of the device, defining the FWTV, while the latter degrades the modulation performance (at a changing wavelength) with increasing temperature, defining the SWTV. Let us quantify these two effects for GaAs.

i) Variation of Well Material Bandgap

The dependence of the GaAs bandgap with temperature is [Casey and Panish]

$$E_g = E_{g0} - aT^2/(T+b) \quad (6.3.1)$$

with values $E_{g0}=1.519$ eV, $a=5.405 \times 10^{-4}$ eV/K and $b=204$ K.

Therefore

$$\begin{aligned} dE_g/dT &= -aT(2b+T)/(T+b)^2 \\ &= -0.452 \text{ meV/K at } 300 \text{ K.} \end{aligned} \quad (6.3.2)$$

If we assume that the FWTV is such as to allow a wavelength shift of one third of the exciton linewidth (of order 10 meV) we can estimate the FWTV to be ± 7 K.

ii) Variation of Phonon Broadening

The phonon broadening linewidth (FWHM) has already been given chapter 2 (2.5.1).

$$\Gamma_T = \Gamma_{ph} / [\exp(h\Omega_{LO}/kT)-1] \quad (6.3.3)$$

with values $\Gamma_{ph} = 20.5$ meV and $h\Omega_{LO} = 37$ meV.

Hence

$$\frac{d\Gamma_T}{dT} = \frac{\Gamma_{ph} h\Omega_{lo}}{kT^2} \frac{X}{(X-1)^2} \quad (6.3.4)$$

where $X = \exp(h\Omega_{LO}/kT)$

At room temperature

$$d\Gamma_T/dT = 0.038 \text{ eV/K.} \quad (6.3.5)$$

This acts to increase the exciton linewidth from its initial value at room temperature of around 10 meV. With the modulator operating in a bias-absorbing mode, this broadening will not only decrease the height of the

biased exciton peak, it will also broaden the zero bias absorption edge, increasing the low transmission state. Bearing this in mind we assume that a significant loss in performance takes place when the exciton linewidth increases by 25%. This leads to a SWTV at room temperature of +65 K. Note that a reduction in temperature improves achievable modulation, albeit with reduced linewidths [Bailey et al.].

Resonant Fabry-Perot Modulator

The operation of a resonant modulator such as the asymmetric Fabry-Perot modulator (AFPM) [Whitehead and Parry], depends upon large absorption changes at the resonant wavelength. A change in temperature not only affects the absorption spectrum but also changes the refractive index, and hence the resonant wavelength can shift away from the wavelength of large absorption change.

Experimental data for the temperature dependent modulation of resonant devices is still lacking and here we only outline our expectations as to what might happen. We assume that there are two causes for the change in refractive index: the wavelength-dependent change in refractive index related to the shift of the absorption edge and quantitatively described by the Kramers-Kronig integral, and the wavelength-independent change in refractive index seen far from the absorption edge [Wherrett et al.]. Now if we are only interested in the refractive index at the wavelength of maximum absorption change, this remains a fixed energy difference from the bandgap, and hence the wavelength-dependent refractive index change is negligible. At this variable wavelength the refractive index will be governed by the other wavelength-independent effect.

The refractive index of GaAs far from the absorption edge changes as [Blakemore]

$$n = n_0(1+cT) \quad (6.3.6)$$

with $n_0 = 3.255$ and $c = 4.5 \times 10^{-5} \text{ K}^{-1}$

The associated change in resonant wavelength accompanying this

refractive index change is

$$\begin{aligned}
 d\lambda_r/dT &= c\lambda_r \\
 &= 0.038 \text{ nm/K at } 850 \text{ nm} \\
 &= -0.065 \text{ meV/K}
 \end{aligned}
 \tag{6.3.7}$$

where λ_r is the resonant wavelength.

The important point to note is that this is an order of magnitude less than the shift of the absorption peak, and hence it is impossible for the resonant wavelength to track with the wavelength of maximum absorption change. As a result the AFPM needs to be operated at a fixed temperature with a fixed operating wavelength. Detailed experimental measurements of the temperature sensitivities of AFPMs are underway, but it seems likely that the SWTV will not be significantly greater than the FWTV and will be of order ± 10 K.

6.4 Implications for System Architectures of Temperature Sensitivity

High speed circuitry is generally power-greedy. In emitter coupled logic (ECL) the transistors are kept out of saturation, but at the price of having large quiescent currents flowing. In CMOS, the input gate capacitances need to be charged for each bit sent, and as the bit rate is increased the current required increases proportionally. The result is heavy power consumption and if the heat sinking is non-uniform there will be large variations in temperature throughout the circuit. Furthermore when starting up one needs to be able to manage the temperature rise from ambient to the steady state condition. An optical interconnect should cope with these in the simplest way possible.

As the temperature increases we have seen that the modulator's performance changes. In the case of the AFPM, both the laser and the modulator temperature need to be fixed to within the FWTV. However if a non-resonant modulator is being used, one has the added flexibility of allowing the operating wavelength to change, hence removing the need for control of *either* the laser or the modulator. A temperature control loop will comprise the following elements: a sensor to indicate what wavelength

discrepancy exists between laser and modulator, a control circuit, and a heater/cooler for the laser/modulator.

The design of the above control loop must depend upon the physical positions of the laser and modulator. However it would seem to be advantageous to control the laser temperature since it will probably be a discrete device separate from the electronic chip. Sensor information would need to be sent from the modulator back to the laser, either optically or by a low bandwidth electronic link. A Peltier cooler could be used as the heater/cooler and if the modulators are closely spaced, the temperature variation between them will be small and one should be able to use the same laser as a source for all of them. For the sensor it might be possible to use the photocurrent or modulated light output from an extra modulator in the same array.

The temperature control of the modulators seems a tougher proposition. The modulator will probably be intimately linked to the electronic chip. Since no integratable cooler would be available the modulator might need to be kept at higher than ambient temperature with a dissipative resistor forming the heater.

The above discussion has focussed upon the modulator. However it should be noted that an added complication arises when the same MQW diodes are used as both detectors and modulators. If the modulator temperature is higher than that of the photodetector, the modulator's operating wavelength may be longer than that of the band-edge of the detector. Temperature control of the detector might be required.

6.5 Receiver Design

The receiver is a key part in an optical interconnect. Fibre-optic receivers typically detect signal powers of -30 dBm at a data rate of 2.4 Gbit/s [Smyth and Hunkin], but to do this dedicated chips are designed around the detector. In an interconnect situation many optical links might be required upon the same chip, and the overall area devoted to the receivers must be a sensibly small fraction of the chip area (<10%). Their power dissipation must also be low. Hence one must trade sensitivity for simplicity and efficiency.

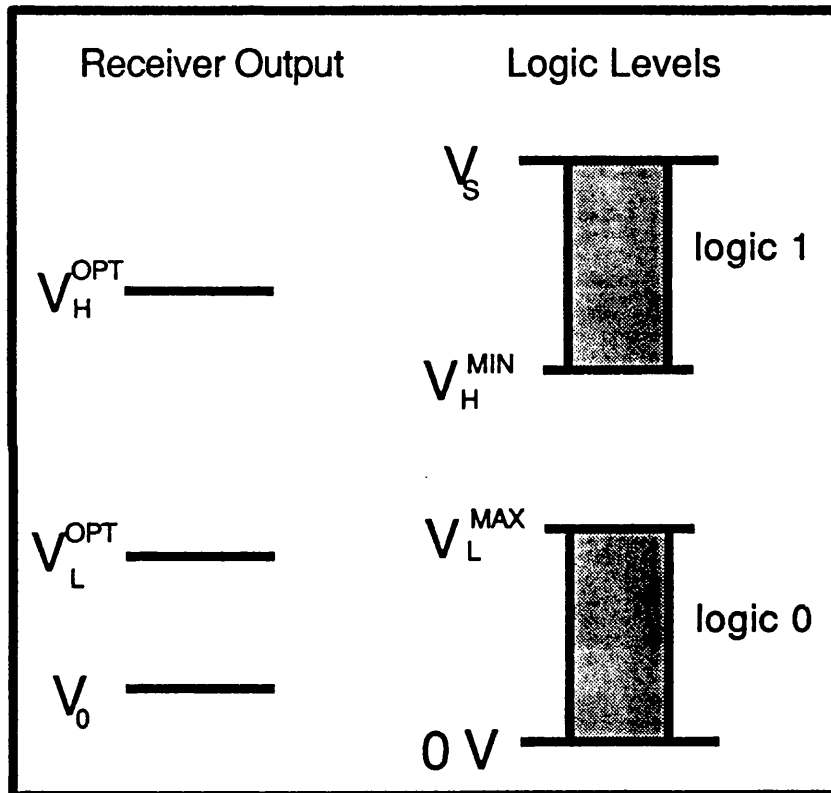


Figure 6.5.1 Voltage levels produced by the optical signal and the input levels required by the logic gate. The optical modulation must be high enough to allow high and low signal to be well within logic signal ranges.

The optical signal incident upon the receiver's detector is converted to an electrical one that will form the input to a logic gate or comparator. The voltages produced by the optical signal must be compatible with the voltages required by the logic gate/comparator. Figure 6.5.1 shows the allowable ranges for the logic levels together with the signal voltages. V_H^{MIN} and the V_L^{MAX} are the minimum and maximum voltages for the high and low logic

levels respectively, V_H^{OPT} and V_L^{OPT} are the high and low voltage derived from the optical signal and V_0 is the voltage given by the receiver when no light is incident. For correct logic operation $V_H^{\text{OPT}} > V_H^{\text{MIN}}$ and $V_L^{\text{OPT}} < V_L^{\text{MAX}}$.

There are several reasons for the optical signal levels to vary: power variation in the source laser output, different path losses and stray light levels. It should be realised that when laser light is used, the stray light can interfere with the signal light, and hence produce greater output changes than its power alone would suggest (similar to coherent detection). The optical signal must have sufficient contrast to outweigh all of the above fluctuations, unless AC coupling, automatic gain/threshold control (AGC) or the use of differential signals are used. Both AC coupling and an AGC require a changing received signal, and hence signal coding would be required to avoid problems when a long string of ones or zeroes is sent continuously. The use of a differential signal requires twice as many modulators, optical pathways and detectors, and will be investigated later.

The above solutions all bring in significant additional complexity to the receiver which should be avoided if possible. Let us consider a simple receiver in which the optical signal is linearly converted to a voltage so that V_L^{OPT} and V_H^{OPT} are given by

$$V^{\text{OPT}} = \Omega P + V_0 \quad (6.5.1)$$

where P is the incident optical power, and Ω is the voltage responsivity.

Let us define T_{pv} as the tolerance required to cope with variations of power reaching the receivers (defined here as the ratio between the maximum and minimum received signal levels, ie. the fractional change in laser output power or path loss). One finds that

$$K > T_{pv} (V_H^{\text{MIN}} - V_0) / (V_L^{\text{MAX}} - V_0) \quad (6.5.2)$$

where K is the contrast of the optical signal. In CMOS, V_H^{MIN} , V_L^{MAX} and V_0 are 3.5, 1.5 and 0V respectively, and hence a contrast of 6.7 dB is required to give a power variation tolerance of 3 dB. For safest operation the high optical

signal level onto the device should be

$$P_H = T_{pv}^{1/2} (V_H^{MIN} - V_0) / \Omega \quad (6.5.3)$$

The equation above can be used to determine the optical power required for a given linear receiver. We now consider two linear designs, the simplest possible one with a resistor in series with the photodiode, and one with a transimpedance amplifier to boost the voltage levels.

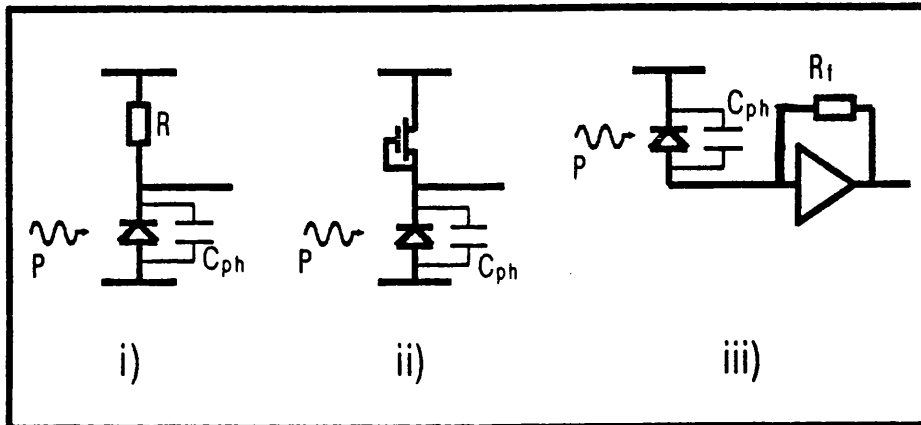


Figure 6.5.2 Simple receiver designs for optical interconnect. Receiver i) is the series bias resistor design where the photocurrent generates a voltage drop across the receiver. The use of a resistor can be avoided in an integrated circuit by using a depletion mode transistor instead of the resistor as shown in receiver ii). Receiver iii) is a transimpedance amplifier design which reduces the required incident energy.

i) Series Bias Resistor

This is the simplest conceivable circuit and employs a resistor to derive a voltage from the photocurrent generated by the diode. The circuit diagram is shown in figure 6.5.2i), also showing the equivalent capacitance in parallel with the photodiode. In integrated circuits resistors can take up a lot of chip area and hence Wu et al. have substituted a depletion mode MOSFET with the gate connected to the source (figure 6.5.2ii)). The same receiver circuit is used by Feldman et al. in the previously mentioned comparison of the speed and power consumption of optical and electrical interconnects. In most fibre

optic receivers the noise is lowest with very high series resistances, but then the RC time constant is so large that equalisation is required afterwards. Equalisation is obviously far too complex to realise in an optical interconnect situation and the resistor should be chosen such that the RC time constant is the maximum allowed for the designated bandwidth:

$$R = 1/2B(C_{ph}+C_{in}) \quad (6.5.4)$$

C_{ph} is the photodiode capacitance and C_{in} is the input capacitance of the following gate. The voltage responsivity is given by

$$\Omega = e\eta_{ph}R/E \quad (6.5.5)$$

where η_{ph} is the photodiode quantum efficiency.

Substituting equations (6.5.4) and (6.5.5) into (6.5.3) we calculate the high level optical power incident to be

$$P_H = T_{pv}^{1/2} 2(V_H^{MIN}-V_0)BE(C_{ph}+C_{in})/e\eta_{ph} \quad (6.5.6)$$

We can draw several conclusions from this. While the bandwidth of the optical medium is very large, to realise it practically one needs to provide a high optical power incident upon the receiver in order to charge the capacitance of the detector and that of the following logic gate. The optical power can be lowered by reducing the detector size, and hence its capacitance, but at the expense of having greater alignment tolerances.

One method of reducing this optical power would be to provide electronic gain between the photodiode and logic. An amplifier of voltage gain A would reduce the optical power required by A .

2) Transimpedance Amplifier

Electronic gain improves the sensitivity of the receiver, and it can be applied in two ways: direct amplification after the series resistor circuit described above, or a transimpedance design as shown in figure 6.5.2iii). As we shall see there is little difference between these two techniques since they both act so as to reduce the voltages that the detector capacitance needs to be charged to and hence both reduce the amount of charge needed to be

generated from the incident light.

The simple circuit of figure 6.5.2iii) can readily be analysed and it is found that the maximum resistance to provide a given bit rate is

$$R_f = (A+1)/2B(C_{ph}+C_{in}) \quad (6.5.7)$$

where A is the gain of the amplifier and C_{in} is now the input capacitance of the amplifier. The voltage responsivity is

$$\Omega = -R_f A e \eta_{ph} / (A+1) E \quad (6.5.8)$$

and hence we get

$$P_H = T_{pv}^{1/2} 2(V_H^{MIN} - V_0) B E (C_{ph} + C_{in}) / A e \eta_{ph} \quad (6.5.9)$$

Compared to (6.5.6) for the series bias resistor, the transimpedance amplifier has reduced the optical signal power required by its own gain value, and hence its effect is the same as having an amplifier placed directly after the traditional series bias resistor circuit.

Differential Signals

We have already shown that a reasonable contrast is required for the optical signal in order to ensure that a low state derived from a source of higher than average power and travelling through a path of lower than average loss will not be received as a high one (and similarly a high state derived from a lower power laser and a high loss path should not be received as a low). One method of overcoming this contrast requirement will be to use two differential signals derived from the same laser and travelling down the same path. The power and loss variation can then only reduce the strength of both signals but never reverse the polarity of the difference. Note that coherent stray light can change the polarity: the stray signals on to the two detectors can be out of phase with one another, hence producing a significant error signal.

Differential optical signals were first suggested by Lentine et al. who demonstrated their advantages in the symmetric self-electrooptic effect device (S-SEED), an optically bistable logic element. More recently

Dickenson and Prise have suggested the use of differential signals for an optical interconnect.

Two different differential receiver circuits are shown in figure 6.5.3. Figure 6.5.3i) is the same circuit as a S-SEED, which in addition to being an optical logic element, also provides an electrical output which can be used as a receiver. As a receiver however, no bistability need be present and normal photodiodes can be used.

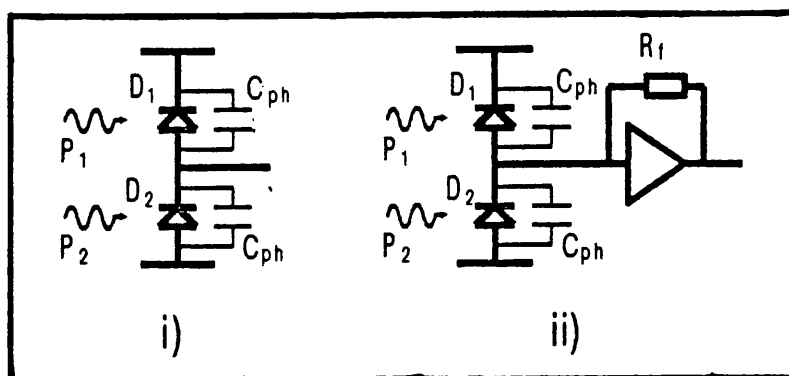


Figure 6.5.3 Receivers for differential signals. Receiver i) is similar to the symmetric SEED, whereas receiver ii) is the differential equivalent of the transimpedance receiver.

Let us consider its operation in detail. If both D1 and D2 are initially in reverse bias and the optical power incident upon D1 exceeds that upon D2, the photocurrents passing through each will be different. Therefore to maintain Kirchoff's current conservation, charge must build up upon D2. This reduces the voltage over D1 until the quantum efficiency is lowered so that the photocurrents are equal and an equilibrium is achieved.

The voltage output thus moves between the supply voltages. This is no longer a linear receiver as the voltage output levels are no longer dependent on the absolute power incident upon the receiver. But the speed of the symmetric SEED is determined by the time required to charge up the photodiodes' capacitances. This is numerically given by

$$\tau_{ch} = (2C_{ph} + C_{in})V_{ss}E/\eta_{ph}e(P_1 - P_2) \quad (6.5.10)$$

where P_1 and P_2 are the incident optical powers on the two detectors. If we

assume that this rise time must be less than half the bit period, we get

$$P_H - P_L = 2V_{ss}BE(2C_{ph} + C_{in})/\eta_{ph}e$$

or

$$P_H = 2V_{ss}BE(2C_{ph} + C_{in})K/(K-1)\eta_{ph}e \quad (6.5.11)$$

This expression takes a similar form to (6.5.6) for the series bias resistor case, because the speed is still limited by the need to charge up both the detector's and gate's input capacitance with the photocurrent.

6.6 Optical Power Budget

From the optical power level incident upon the receiver, knowing the various losses in the optical imaging, the optical powers elsewhere in the link can be evaluated according to table 1.

Location	Optical Power
Received Power (high level)	P_H
Modulator Output (high level)	FP_H/η_{m-r}
Modulator Input	$P_m = FP_H/\eta_{m-r}T_{HI}$
Off-chip Laser Source	$P_{las} = FP_H/\eta_{m-r}T_{HI}\eta_{s-m}$

Table 6.6.1 Power levels in the optical interconnect. η_{s-m} is the loss from source to modulator, T_{HI} the modulator insertion loss, F the fanout and η_{m-r} the loss from modulator to receiver.

6.7 Causes of Power Dissipation

We have already cited lower power dissipation as being of considerable importance in an optical interconnect. But what is the dissipation of an optical link and where does it occur? Let us examine each contribution to the power dissipation in turn. The laser source must convert electrical power to optical power to provide the light to drive the link. The modulator sinks two sorts of current: a bandwidth dependent current to charge its capacitance,

and a steady-state photocurrent when in its biased state. In the receiver, since the photocurrent itself charges the photodiode capacitance, the photocurrent is the only current drain from the power supply. Finally there is the power dissipated in the receiver amplifier (if one is used). In table 2 below we list and quantify these contributions. Note that for fanouts of more than 1, we calculate the dissipation of an individual link by dividing the modulator and laser dissipations by the fanout.

Contribution	Total	On Chip
Source Laser	$P_{\text{las}}/(\eta_{\text{las}}F)$	P_m/F
Modulator Capacitance	$BC_m V_m^2/2F$	$BC_m V_m^2/2F$
Modulator Photocurrent	$V_m(1-T_B)eP_m/2EF$	$V_m(1-T_B)eP_m/2EF$
Receiver	$V_{ss}\eta_{\text{ph}}eP_H(1+1/K)/2E$	$V_{ss}\eta_{\text{ph}}eP_H(1+1/K)/2E$
Receiver Amplifier	P_{amp}	P_{amp}

Table 6.7.1 Contributions to the power dissipation for an individual link in an optical interconnect. η_{las} is the efficiency of the laser.

The sum of the above terms gives the total power dissipated for one link. Often however, one is not so much concerned with this total power, but rather the amount dissipated where it is difficult to get rid of: on the chip. All the terms except the power required to drive the laser directly add to the on-chip power dissipation. The laser power can be supplied remotely, perhaps through a fibre optic-distribution network, and hence only that proportion of the light absorbed near the chip would increase the on-chip power dissipation. Thus in the on-chip dissipation we include only the optical power incident on the modulator, P_m/F , as well as the other four electrical terms.

We are now in a position to calculate total and on-chip power dissipations for different bit rates, modulator and detector capacitances, optical path losses, fanouts and bandwidths.

6.8 Calculation of Power Dissipation

For our calculations of power dissipation in an optical link we use parameter values in table 6.8.1, unless explicitly stated otherwise. The voltages and logic gate input capacitance are taken for a 5 μm , 5 V CMOS process, the major technology of today's integrated circuits. It is particularly suited to the use of MQW modulators, since the logic level voltages are those of the supply voltage. ECL, on the other hand, uses smaller voltage swings within the same 5 V supply.

Parameter	Value
Bit Rate (B)	500 MBit/s
Wavelength (λ)	860 μm
Optical Imaging Loss ($\eta_{\text{op}}=\eta_{\text{s-m}}=\eta_{\text{m-r}}$)	3 dB
Fanout (F)	1
Power Variation Tolerance	3 dB
Modulator Contrast (K)	10 dB
Modulator Insertion Loss (T_{HI})	3 dB
Modulator Voltage	5 V
Modulator Intrinsic Region Width (L_i)	1 μm
Modulator/Detector Size (L_m)	10 μm
Receiver Supply Voltage (V_{ss})	5 V
Detector Quantum Efficiency (η_{ph})	80 %
Receiver Amplifier Gain (A)	10
Receiver Amplifier Power Dissipation	10 mW
Receiver/Logic Gate Input Capacitance (C_{in})	10 fF
Laser Power Efficiency (η_{las})	30 %

Table 6.8.1 Values of parameters used for calculation of link power dissipation.

We assume the modulator and detector to be of the same size. Their

capacitance is given by the simple parallel plate equation:

$$C_m = \epsilon L_m^2 / L_i \quad (6.8.1)$$

Additional edge capacitance caused by field fringing will start to become important in devices where the modulator width is similar to the modulator thickness. Note that the optical window of the modulator will be smaller than the device size and the optical spot size will be even smaller still. But the modulator/detector size not only defines the necessary spot size, it also determines the allowable mechanical alignment required of the optical system (say 20% of the device size).

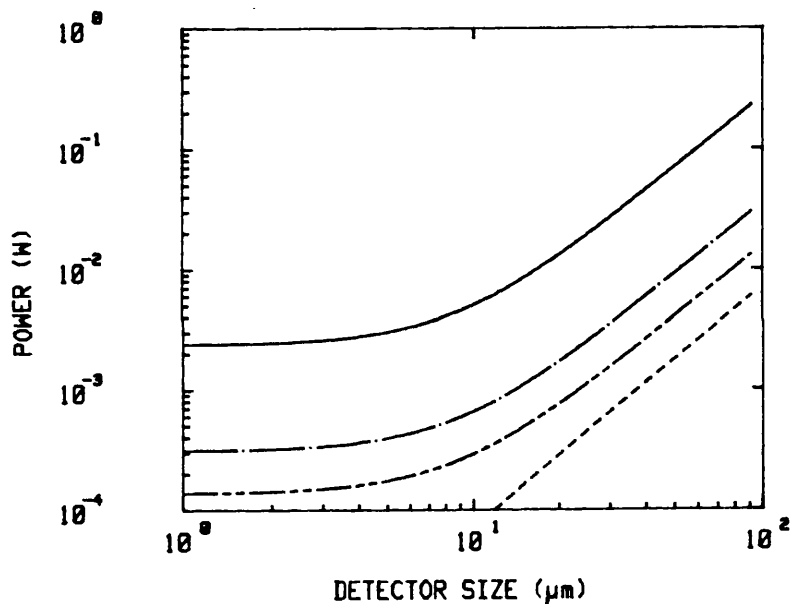


Figure 6.8.1 Sources of power dissipation in a optical link as a function of the modulator/detector size. Contributions to the dissipation are from: driving the laser source (solid), charging up modulator capacitance (dashed), provision of modulator photocurrent (dotted and dashed) and the provision of detector photocurrent (1 long, 2 short dashes). Values of parameters used are in table 6.8.1.

In figure 6.8.1 we plot the different contribution to the dissipation as a function of detector/modulator size. Note that the largest source of power is the laser itself, preferably kept off the chip. The dissipation arising from the detector and modulator photocurrents is more significant than that of

charging up the modulator. Since charging the modulator capacitance is the only power loss unrelated to the optical power, its insignificance means that when fanning out from one transmitter to several receivers, the effect of the the fanout on the dissipation in each individual link is negligible.

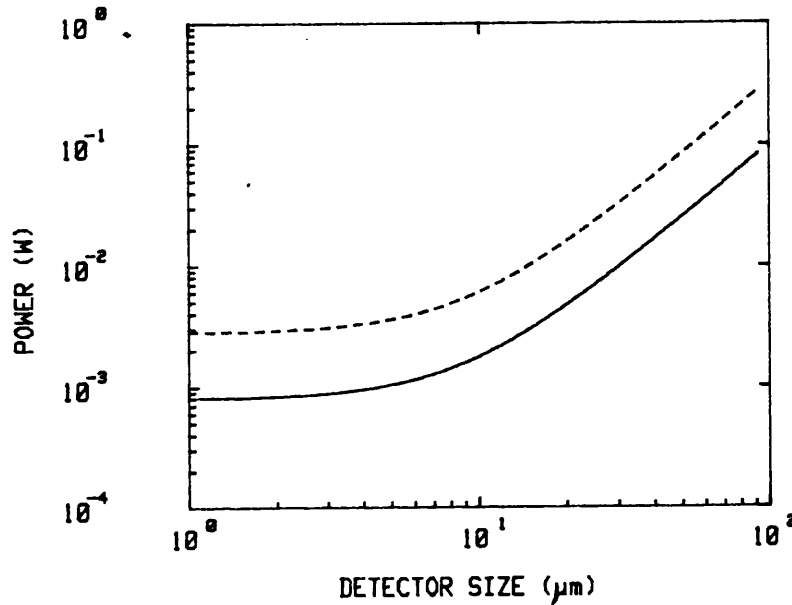


Figure 6.8.2 Total (dotted) and on-chip (solid) power dissipation against modulator/detector size. Of the power used by the laser, only the optical power incident upon the modulator is considered part of the on-chip dissipation.

In figure 6.8.2 we plot the total and on-chip dissipation as a function of detector size. With the detector size below $10 \mu\text{m}$, the gate input capacitance dominates the detector capacitance and the power is independent of detector size. However for larger sizes the power become proportional to the square of the detector size, and there is an obvious trade-off to be made between the power used and the alignment tolerance.

In figures 6.8.3 and 6.8.4 we plot the dependence of the on-chip dissipation as a function of optical path loss and bit rate respectively. All of the dissipative mechanisms are proportional to the bit rate. In figure 6.8.5 we compare receivers with and without an amplifier, whose gain and dissipation are 10 and 10 mW respectively. With a small detector, the amplifier power dissipation dominates the overall dissipation, whereas with

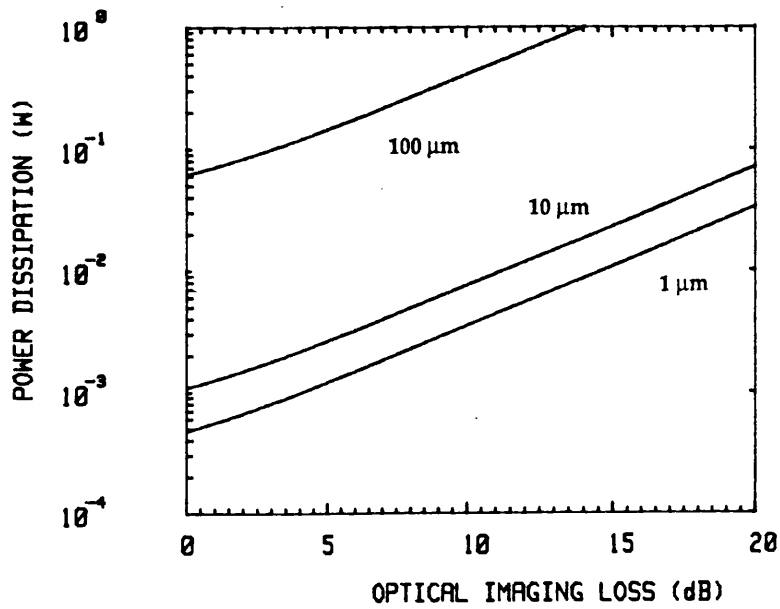


Figure 6.8.3 On-chip power dissipation against optical imaging loss ($\eta_{\text{op}} = \eta_{\text{m}} = \eta_{\text{m-r}}$) for modulator/detector sizes of 1, 10 and 100 μm .

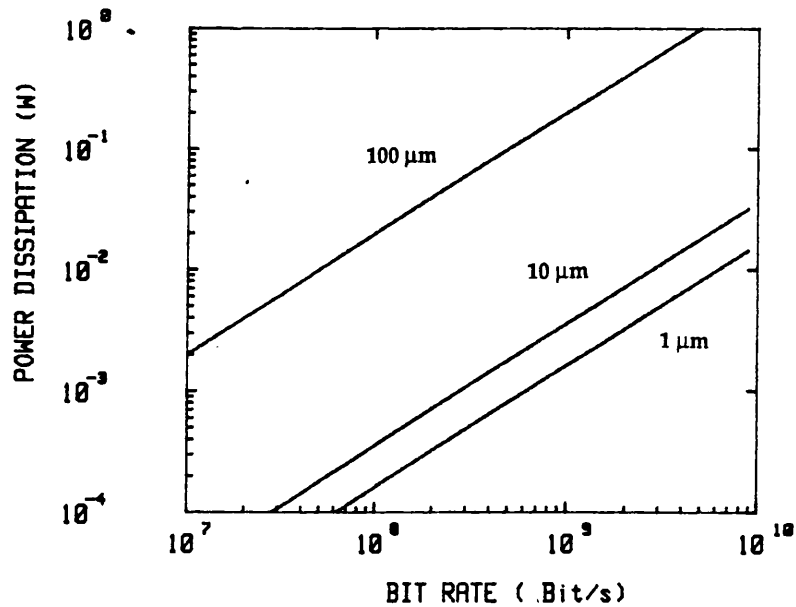


Figure 6.8.4 On-chip power dissipation against bit rate for modulator/detector sizes of 1, 10 and 100 μm .

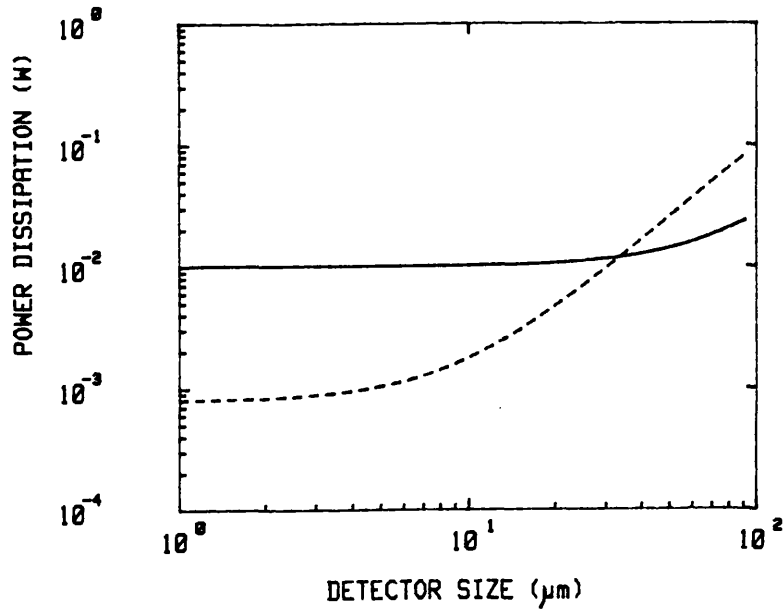


Figure 6.8.5 On-chip power dissipation with (dotted) and without (solid) an amplifier in the receiver. The amplifier has a voltage gain of 10 and an additional dissipation of 10 mW.

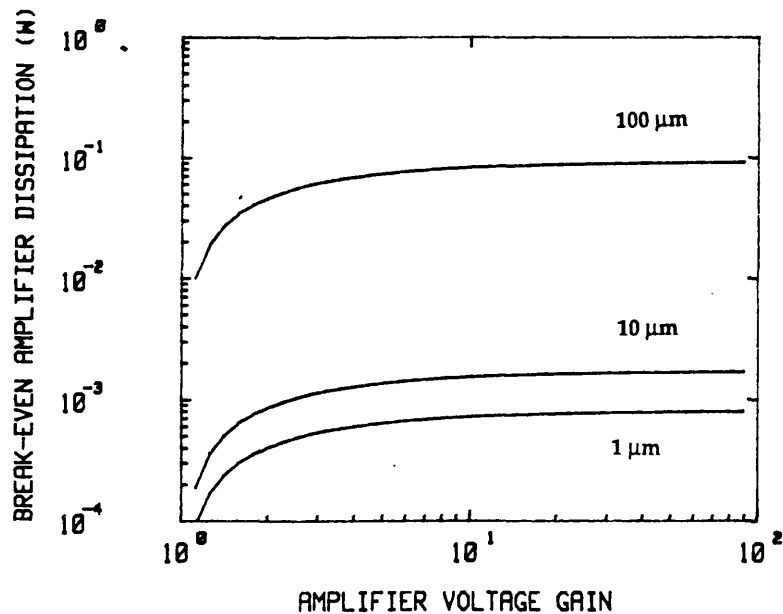


Figure 6.8.6 Break-even power dissipation against amplifier gain for modulator/detector sizes of 1, 10 and 100 μm . The breakeven power dissipation is the minimum dissipation required in order for the amplifier to reduce the overall on-chip dissipation.

the larger devices the amplifier reduces the amount of optical power required, and the power dissipation reduced. For any detector size at a given amplifier gain one can define a break-even amplifier dissipation above which the use of an amplifier increases the overall dissipation. The breakeven power dissipation is plotted against amplifier gain in figure 6.8.6 and it can be seen that above a certain gain, additional gain is only useful if accompanied by small additional amplifier dissipation.

6.9 Comparison with Electrical Interconnects

A full and fair comparison between optical and electronic interconnects involving cost, reliability, connectivity, delay, etc. is impossible until both an application is fixed and a practical optical technology has been developed. However, we have seen in the above section that one property, the power dissipation, is relatively easily determined from the properties of the transmitter and receiver. As a result, several authors have used the power dissipation for a comparison with electronic interconnect [Kostuk et al., Feldman et al.]. Is this reasonable? We believe it is. There are other important properties, but these are difficult to determine and in general are related to the power dissipation. Take the data delay, generally caused by RC time constant in charging up metal lines. It is the same provision of charge that causes the dissipation of power. Note that whereas the power dissipation in charging up a given length of track is fixed, the data delay is changeable by varying the size of the driving transistor. The same argument is applicable to chip area. The more charge one needs to provide, the greater the size of transistors needed to provide it. To summarise, provided the technological problems can be overcome, it will be the ability of a given technique to provide a given bit rate over a given length at low powers that will determine its worth.

To model an electrical link we consider a intrachip link using a metal track for a 5 V, 5 μm CMOS process, of capacitance per unit length (C_l) of 0.225 pF/mm [Pucknell and Estraghian]. The power required to charge it up is given by

$$\begin{aligned} P_{\text{elec}} &= B C_l V^2 / 2 \\ &= 1.4 \text{ mW/mm @ 500 MBit/s} \end{aligned} \quad (6.9.1)$$

where l is the length of the line.

Feldman et al. introduced the concept of the break-even line length [Feldman et al.] above which the dissipation in the optical link is greater than that of the electrical one. This generally presupposes a given optical imaging loss to be independent of link length. However, the assumption of length-independent optical losses is probably a misleading one. Reflection holograms become less and less efficient as the angle becomes more and more oblique, and the need to keep the optical imaging compact and stable will limit the distance of the optics for the chip. Therefore, instead of defining a break-even line length in figure 6.9.1 we plot the break-even optical loss ($\eta_{op} = \eta_{s-m} = \eta_{m-r}$) as a function of length.

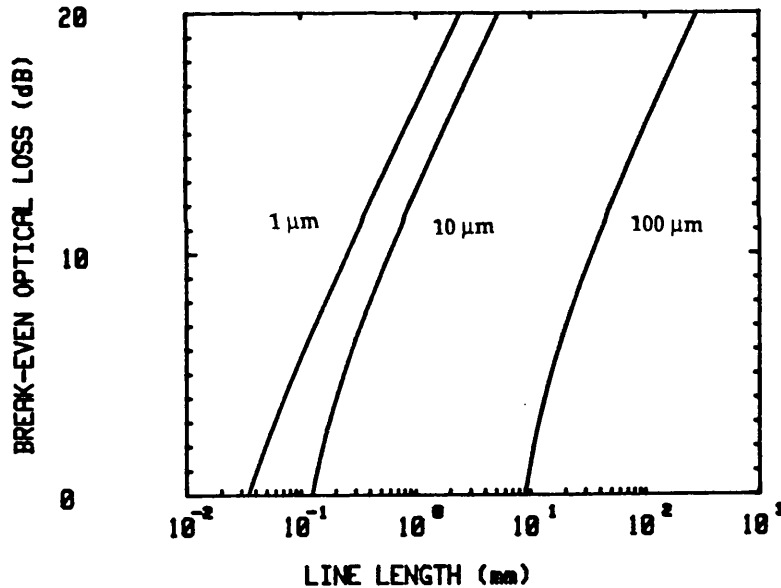


Figure 6.9.1 Break-even optical imaging loss against link length for modulator/detector sizes of 1, 10, and 100 μm . The break-even optical imaging loss is the maximum acceptable imaging loss before the optical interconnect (amplifier included if advantageous) dissipation exceeds that of charging up the length of metal track.

Finally let us consider the effects of scaling down the feature size on the chip. The reduction in the track width is compensated for by the reduction in track thickness and the capacitance per unit length of the electrical line will

remain the same. At first sight then, little change can be expected in the electrical dissipation. However, some scaling schemes also reduce the voltage, and at the reduced voltages, the modulators will not provide such good modulation and their capacitance will be increased (since the optimum number of wells is reduced). It is therefore in the interests of the optical link not to scale the voltages too drastically.

6.10 Summary

In this chapter we have addressed and analysed the practical considerations needed for the development of optical interconnects, utilising MQW modulators. We have shown that in simple receivers the modulator must have a certain contrast (typically 7 dB) in order to overcome fluctuations in path losses and source power variation. If this is not possible differential signals, or techniques such as ac coupling or an AGC (with accompanying signal coding) are required. AFPMs look promising devices in providing these contrasts, but the design must carefully consider their sensitivity to both incident angle and temperature. The temperature tolerance of MQW modulators has been defined in terms of the fixed wavelength temperature variation (FWTV) and the scanning wavelength temperature variation (SWTV). In non-resonant modulators the SWTV is much larger than the FWTV, and this makes it possible to allow the modulator temperature to vary depending upon its environment, provides the laser source scans with the modulator wavelength.

We analyse the expected power dissipation in a typical link, and find one of the most important trade-offs concerns the device size chosen. Small devices with small capacitances require less power, but better quality and tighter alignment of the optics is required. We analyse the use of an amplifier in the receiver, which can reduce the optical power required incident upon the receiver but contributes its own dissipation. We find there is a break-even power dissipation, above which the amplifier increases the overall power dissipation. For devices of less than 10 μm size, this break-even power dissipation is only a few mW, even with high gains. Thus amplifiers only seem likely to be useful with large detectors, and they should have a low dissipation rather than high gain.

Finally we have compared the dissipation with that of charging up a

metal track on a chip. We define and calculate a break-even optical imaging loss below which the optical interconnect dissipates less power, as a function of line length.

CONCLUSIONS

The MQW electroabsorption modulator is attractive in many respects. Its growth and fabrication is relatively simple and the use of III-V material should enable future integration with other components. Its speed is limited by its capacitance, and by scaling the device dimension down operation well into the GHz region should be possible. The operating voltage of less than 10 V relaxes the requirements of the driving circuitry and its optical bandwidth is large enough to be compatible with semiconductor lasers. It can be made in either a transverse or waveguide form, although this thesis has been principally concerned with the former because of the relative ease of coupling into the device.

The physical effect used by the modulator is electroabsorption, and its modelling in GaAs/(GaAl)As MQWs forms the basis for much of the work. The model for the field-dependent absorption that includes not just the shift of the exciton peaks, but also their loss in oscillator strength and their broadening. The importance of three broadening mechanisms has been stressed: phonon broadening, well width fluctuation broadening, and broadening due to electric field variations within the p-i-n caused by background doping in the intrinsic region. The calculation has been compared with experimental spectra to good agreement. An investigation of differing well widths has shown for narrower wells that the Stark shift is less sensitive to field, but given a particular shift, the exciton retains more of its oscillator strength.

The model for the electroabsorption has then been used to evaluate the limits to modulation in devices. The degree of modulation is often considered in terms of contrast ratio and it was typically thought that this should be greater than 10 before a modulator became useful. In this work we have challenged this assumption. We have introduced the transmission change as an important figure of merit, especially for simple communications applications where it is proportional to the modulated 'AC' signal output. A high contrast is required in certain applications, typically when optical signals are merged, but it should always be quoted with the accompanying insertion loss.

Waveguide devices potentially offer very good modulation because of the long optical interaction length, but their design is likely to be dominated by external factors such as coupling into the device, and compatibility with surrounding integrated components. However, in transverse modulators the number of wells is limited by the need to keep the intrinsic region thin so

that high fields can be applied at reasonable voltages. To design the device, we propose the use of voltage invariant optimisation (VIO) curves in deducing the optimum number of wells for a given design voltage, and use the technique to investigate the limitations to device modulation. Well widths of around 50 Å require high operating voltages, but potentially offer the best modulation. A well width of 100 Å offers good low voltage performance in both bias transmitting and bias-absorbing modes, while 150 Å offer good, low voltage modulation only in its bias-transmitting mode. In a non-resonant transmission modulator, a transmission change of 30 % is typical for 5 V operation, with small improvements possible with better material. The VIO technique can be applied to resonant modulators such as the AFPM, which should provide a contrast of 13 dB with an insertion loss of 3 dB at only 5 V.

The model for GaAs/(GaAl)As MQWs has been extended to cover the (GaIn)As/InP material system whose operating wavelength is close to that of the low loss window of optical fibres. Unfortunately, the lower absolute absorption coefficient at the exciton peak means that transverse devices need to be thicker, and require correspondingly higher operating voltages. To achieve the equivalent performance of a GaAs/(GaAl)As device operating at 5 V, a (GaIn)As/InP modulator requires at least 15 V.

In fibre-optics, several applications have been considered. Higher bit rate transmission without significant dispersion should be possible using MQW modulators because of the absence of the relaxation oscillations that create chirp in diode lasers. In this role one would like an integrated laser-waveguide modulator combination. The other fibre-optic uses rely upon the dual functionality of the MQW diode as both modulator and detector, in both a bidirectional link, and in a fibre-optic chain. Simple architectures like these are aimed at lower speed and lower cost links, and could be implemented in the short term. The principal limitation to system performance does not appear to be achievable modulation, but back reflections and the need to efficiently couple light from fibre to device and back to the fibre.

Finally we have investigated the use of MQW modulator in an optical interconnect. A certain modulator contrast is useful (≈ 7 dB) to allow for fluctuations in the average received signal power while providing compatible voltages to the following logic gate. An AFPM can readily provide this contrast, but careful consideration must be given to its angular and temperature sensitivity. The power dissipation of a

link is calculated and a clear trade-off is presented between that power and the size of the modulator and detectors. Only with large devices does an amplifier in the receiver lower the dissipation. A comparison of the dissipations in optical and electronic interconnections is made and we calculate the maximum optical imaging loss required for the optical link to dissipate less power.

To conclude, the operation of the MQW modulator is now well understood and its potential performance has been assessed. We have shown that the modulation it provides is good enough to be useful in a variety of applications. In fact the performance of the systems study seem more constrained by such practical considerations as efficient optical coupling, and temperature control. Future work should concentrate upon the integration of the modulator with the adjacent optical and electronics systems, rather than the development of the isolated device.

LIST OF PUBLICATIONS

Stevens,P.J. and Parry,G., "A Model for the electric field dependence of the absorption spectrum of quantum well material", 8th National Quantum Electronics Conference, St. Andrews, Sept. 1987.

Whitehead,M., Stevens,P.J., Rivers,A., Parry,G., Roberts,J.S., Mistry,P., Pate,M.A., Hill,G., "The effects of well width on the characteristics of GaAs/GaAlAs multiple quantum well electro-absorption modulators", Appl. Phys. Lett., 53, pp. 956-958, 1988.

Stevens,P.J., Whitehead,M., Bradley,,P.J., Rivers,A.W., Parry,G., Roberts,J.S., Mistry,P., Pate,M.A., and Hill,G. "Limits to the performance of transverse and waveguide electroabsorption and electrorefraction modulators", European Conference on Optical Communications, pp. 33-36, Brighton, Sept. 1988.

Stevens,P.J., Whitehead,M., Parry,G. and Woodbridge,K., "Computer modeling of the electric field dependent absorption spectrum of multiple quantum well material", IEEE J. Quant. Elect., 24, pp. 2007-2016, 1988.

Stevens,P.J., and Parry,G., "Limits to electroabsorption modulation in GaAs/(GaAl)As multiple quantum well diodes", J. Light. Tech., 7, pp. 1101-1108, 1989.

Stevens,P.J., and Parry,G., "Limits to normal incidence electroabsorption modulation in GaInAs/InP multiple quantum well diodes", Top. Meet. on QWs for optics and optoelectronics", Salt Lake City, pp. 198-201, Mar 1989

Stevens,P.J., and Mukai,T., "Predicted performance of quantum well GaAs/(GaAl)As optical amplifiers", to be submitted to IEEE J. Quant. Elect.

REFERENCES

Ajisawa,A., Fujiwara,M., Shimizu,J., Sugimoto,M., Uchida,M., Ohta,Y and Asakawa,K., "Monolithic integrated optical gate 2x2 matrix switch using GaAs/AlGaAs multiple quantum well structure", Photonic Switching, Springer series in electronics and photonics, 25, pp. 63-66, 1987.

Alping,A. and Tell,R., "100 Mbit/s semiduplex optical fibre transmission experiment using GaAs/GaAlAs laser transceivers", J. Light. Tech., LT-2, pp. 663-667, 1984.

Alping,A., Wu,X.S., Hausken,T.R. and Coldren,L.A., "Highly efficient waveguide phase modulator for integrated optics", Appl. Phys. Lett., 48, pp. 1243-1245, 1986.

Alping,A., Wu,X.S. and Coldren,L.A., "Wavelength dependence of high-performance AlGaAs/GaAs waveguide phase modulators", Elect. Lett., 23, pp. 93-95, 1986.

Asada,M., Kameyama,A. and Suematsu,Y., "Gain and intervalence band absorption in quantum well laser", IEEE J. Quant. Elect., QE-20, pp. 745-753, 1984.

d'Auria,L., Chevalier,G. and Maillot,P., "Libido using Eros: half-duplex optical link", Elect. Lett., 15, pp. 820-821, 1979.

Austin,F.J. and Jaros,M., "Electronic structure of an isolated GaAs-GaAlAs quantum well in a strong electric field", Phys Rev B, 31, pp. 5569-5571, 1985.

Bailey,R.B., Sahai,R., Lastufka,C. and Vural,K., "Temperature-dependent characteristics of GaAs/GaAlAs multiple quantum well optical modulators", Topical meeting on QWs for Opt. and Opto-elect., pp. 210-213.

Bar-Joseph,I., Klingshirn,C., Miller,D.A.B., Chemla,D.S., Koren,U. and Miller,B.I., "Quantum confined Stark effect in InGaAs/InP quantum wells grown by organometallic vapor phase epitaxy", Appl. Phys. Lett., 50, pp. 1010-1012, 1987.

Barnes,P., Zouganeli,P., Rivers,A., Whitehead,M., Parry,G., Woodbridge,K., Roberts,C., "GaAs/AlGaAs multiple quantum well optical modulator using multilayer reflector stack grown on Si substrate", Elect. Lett., 25, pp. 995-996, 1989.

Bastard,G., Mendez,E.E., Chang,L.L. and Esaki,L., "Variational calculations on a quantum well in an applied field", Phys. Rev. B, 28, pp. 3241-3245, 1983.

Bastard,G. and Brum,J.A., "Electronic states in semiconductor heterostructures", IEEE J. Quant. Elect., QE-22, pp.1625-1644, 1986.

Bennett,B.R. and Soref,R.A., "Electrorefraction and electroabsorption in InP, GaAs, GaSb, InAs and InSb", IEEE J. Quant. Elect., QE 23, pp. 2159-2166, 1987.

Bimberg,D., Mars,D., Miller,J.N., Bauer,R., Oertel,D. and Cristen,J. "Kinetics of island formation at the interfaces of AlGaAs/GaAs/AlGaAs quantum wells upon growth interruption", Superlattices and Microstructures, 3, pp.

79-82, 1987.

Bimberg,D., Christen,J., Fukunaga,T., Nakashima,H., Mars,D.E. and Miller,J.N., "Cathodoluminescence atomic scale images of monolayer islands at GaAs/GaAlAs interfaces", J. Vac. Sci. Technol., B5, pp. 1191-1197, 1987.

Blakemore,J.S., "Semiconducting and other major properties of Gallium Arsenide", J. Appl. Phys., 53, pp. R123-R181.

Bohn,P.B. and Das,S.K., "Return loss requirements for optical duplex transmission", J. Light. Tech., LT-5, pp 243-254, 1987.

Born,M. and Wolf,E., "Principles of optics", Pergamon, pp. 66-70, 1984.

Boyd,G.D., Miller,D.A.B., Chemla,D.S., McCall,S.L., Gossard, A.C. and English, J.H., "Multiple quantum well reflection modulator", Appl. Phys. Lett., 50, pp. 1119-1121, 1987.

Boyd,G.D., Bowers,J.E., Soccolich,C.E., Miller,D.A.B., Chemla,D.S., Chirovsky,C.E., Gossard,A.C. and English, J.H., "5.5 GHz Multiple quantum well reflection modulator", Elect. Lett., 25, pp. 558-559, 1989.

Brenner,K.-H. and Sauer,F., "Diffractive-reflective optical interconnects", Appl. Opt., 27, pp. 4251-4254, 1988.

Brum,J.A. and Bastard,G., "Electric field induced dissociation of excitons in semiconductor quantum wells", Phys. Rev. B, 31, pp. 3893-3898, 1985.

Carr.E.C., Wood,T.H. and Burrus,C.A., "Analysis of the quantum-confined Stark effect in GaSb/AlGaSb" multiple quantum wells", Appl. Phys. Lett., 53, pp. 2305-2307, 1988.

Casey,H.C. and Panish,M.B., "Heterostructure Lasers", Academic Press, pp.193, 1978.

Chan,K.S., "Theory of optical absorption due to unbound states of an exciton in a quantum well", J. Phys. C, 20, pp. 791-796, 1987.

Chemla,D.S. and Miller,D.A.B., "Room temperature excitonic nonlinear-optical effects in semiconductor quantum well structures", J. Opt. Soc. Am. B, 7, pp. 1155-1173, 1985.

Chemla,D.S., Miller,D.A.B., Smith,P.W., Gossard,A.C. and Weigmann,W., "Room temperature excitonic nonlinear absorption and refraction in GaAs/AlGaAs multiple quantum well structures", IEEE J. Quant. Elect., QE-20, pp. 265-275, 1984.

Chen,Y., Kothiyal,G.P., Singh,J. and Bhattacharya,P.K., "Absorption and photoluminescence studies of the temperature dependence of exciton lifetime in lattice- matched and strained quantum well systems", Superlattices and Microstructures, 3, pp. 657-664, 1987.

Collins,R.T., Klitzing,K.v. and Ploog,K., "Photocurrent spectroscopy of GaAs/AlGaAs quantum wells in an electric field", Phys. Rev. B, 33, pp. 4378-4381, 1986.

Coombes,G.P., "565 Mbits/s duplex transmission at 1300 nm over 50 km of single-mode optical fibre", Elect. Lett., 22, pp 821-822, 1987.

Das,U., Berger,P.R. and Bhattacharya,P.K., "InGaAs/GaAs multiquantum well electroabsorption modulator with integrated waveguide", *Opt. Lett.*, 12, pp. 820-822, 1987.

Dawson,P., Duggan,G., Ralph,H.I and Woodbridge,K., "Photoluminescence decay times in (AlGa)As-GaAs multiple quantum well heterostructures", *Superlattices and Microstructures*, 1, pp. 173-176, 1985.

Dawson,P., Moore,K.J., Duggan,G., Ralph,H.I. and Foxon,C.T.B., "Unambiguous observation of the 2s state of the light and heavy hole excitons in GaAs-(AlGa)As multiple-quantum-well structures", *Phys. Rev. B*, 34, pp. 6007-6010, 1986.

Delavaux, J.-M.P., Kuo,C.Y., Nguyen,T.V., Smith, R.W., "Dependence of bit error rate performance on extinction ratio of Ti:LiNbO₃ intensity modulator", *Elect. Lett.*, 22, pp 1139-1141, 1986.

Dickinson,A. and Prise,M.E., "A free space optical interconnect scheme", *Top. Meet. Optical Computing*, Salt lake City, pp. 132, 1989.

Dingle.R., Wiegmann,W. and Henry,C.H., "Quantum states of confined carriers in very thin Al_xGa_{1-x}As-GaAs-Al_xGa_{1-x}As heterostructures", *Phys. Rev. B*, 33, pp. 827-830., 1974.

Dingle,R. and Weigmann,W., "Optical investigation of stress in the central layer of molecular-beam-grown AlGaAs-GaAs-AlGaAs structures", *J. Appl. Phys.*, 46, pp. 4312-4315, 1975.

Duggan,G., H.I.Ralph and Moore,K.J., "Reappraisal of band-edge discontinuities at the AlGaAs-GaAs heterojunction", *Phys. Rev. B*, 32, pp. 8395-8397, 1985.

Dolfi,D.W., Nazarathy,M. and Jungerman,R.L., "40 GHz electro-optic modulator with 7.5 V drive voltage", *Elect. Lett.*, 24, pp. 528-529, 1988.

Ekenberg,U., and Altarelli,M., "Exciton binding energy in a quantum well with inclusion of valence band coupling and non-parabolicity", *Phys. Rev. B*, 7585-7595, 1987.

Elliott,R.J., "Intensity of optical absorption by excitons", *Phys. Rev.*, 106, pp. 1384-1389, 1957.

Feldman,M.R., Esener,S.C., Guest,C.C., Lee,S.H., "Comparison between optical and electrical interconnects based upon power and speed considerations", *Appl. Opt.*, 27, pp. 1742-1751, 1988.

Fernandez,F.M. and Castro,E.A., "Hypervirial-perturbational treatment of a particle in a box in the presence of an electric field", *Physica A*, 111, pp. 334-342, 1982.

Forrest,S.R., Schmidt,P.H., Wilson,R.B. and Kaplan,M.L., "Relationship between the conduction-band discontinuities and band-gap differences of InGaAsP/InP heterojunctions", *Appl. Phys. Lett.*, 45, pp. 1199-1201, 1984.

Frijink,P.M., Andrè,J.P. and Erman,M., "Metal-organic vapour-phase epitaxy of multilayer structure with III-V semiconductors", *Philips Tech. Rev.*, 43, pp.

118-132, 1987.

Gaggione,H., Le Gall,D., "Digital video transmission and coding for broadband IDSN", IEEE Trans. Cons. Elect., 34, pp. 16-35, 1988.

Goodman,J.W., Leonberger,F.I., Kung,S.Y. and Athale,R.A., "Optical interconnections for VLSI systems", Proc. IEEE, pp. 850-866, 1984.

Gossard,A.C., "Growth of microstructures by molecular beam epitaxy", IEEE J. Quant. Elect., QE-22, pp.1649-1655, 1986.

Gourley,P.L. and Drummond,D.J., "Single crystal, epitaxial multilayers of AlAs, GaAs, and $\text{Al}_x\text{Ga}_{1-x}\text{As}$ for use as optical interferometric elements", Appl. Phys. Lett., 49, pp. 489-491, 1986.

Gowar,J., "Optical communication systems", Prentice Hall International, chapter 15, 1983.

Greene,R.L., Bajaj,K.K. and Phelps,D.E., "Energy levels of Wannier excitons in $\text{GaAs-Ga}_{1-x}\text{Al}_x\text{As}$ quantum well structures", Phys. Rev. B, 29, pp. 1807-1812, 1984.

Guy,D.R.P., Apsley,N., Taylor,L.L., Bass,S.J., "Theory of an electro-optic modulator based on quantum wells in a semiconductor etalon", SPIE: 1987 Semiconductor Conferences, Vol. 792, Quantum well and superlattice physics, 1987.

Guy,D.R.P., Besgrove,D.D., Taylor,L.L., Apsley,N. and Bass,S.J., "Experimental study of InGaAs-InP MQW electro-absorption modulators", IEE Proc., Pt. J, 136, pp. 46-51, 1989.

Harwit,A., Harris,J.S.,Jnr. and Kapitulnik,A., "Calculated quasi-eigenstates and quasi-eigenenergies of quantum well superlattices in an applied electric field", J. Appl. Phys. ,pp. 3211-3213, 1986.

Harwit,A. and Harris,J.S.,Jnr., "Observation of Stark shifts in quantum well intersubband transitions", Appl. Phys. Lett., 50, pp. 685-687, 1987.

Hiroshima,T. and Lang,R., "Effect of conduction band nonparabolicity on the quantized energy levels of a quantum well", 1986,Appl. Phys. Lett., 49, pp 457-456.

Hong,S. and Singh,J., "Excitonic energies and line broadening effects in InAlAs/InGaAs modulator structures", J. Appl. Phys, 62, pp. 1994-1999, 1987a.

Hong, S.C., Jaffe,M. and Singh,J., "Theoretical studies of optical modulation in lattice matched and strained quantum wells due to transverse electric fields", IEEE J. Quant. Elect., QE 23, pp 2181-2195, 1987b.

Hsu,T.Y., Wu,W.Y. and Efron,U., "Amplitude and phase modulation in a 4 μm thick GaAs/GaAlAs multiple quantum well modulator", Elect. Lett., 24, pp 603-605, 1988a.

Hsu,T.Y., Efron,U., Wu,W.Y., Schulman,J.N. and D'Haenens,I.J., "Multiple quantum well spatial light modulators for optical processing applications", Opt. Eng., 27, pp. 372-384., 1988b.

Huang,A., "Architectural considerations involved in the design of an optical digital computer", Proc. IEEE, 72, pp. 780-786, 1984.

Ikonic,Z., Milanovic,V. and Tjapkin,D., "Quantum well electroabsorption in a strong electric field: a continuous spectrum approach" , J. Phys. C, 20, pp. 1147-1160, 1987.

Islam,M.N., Hillman,R.L., Miller,D.A.B., Chemla,D.S., Gossard,A.C. and English,J.C., "Electroabsorption in GaAs/AlGaAs coupled quantum well waveguides", 50, Appl. Phys. Lett., pp. 1098-1100, 1988.

Iwamura,H., Kobayashi,H. and Okamoto,H., "Excitonic absorption spectra of GaAs-AlAs superlattice at high temperature", Jap. J. Appl. Phys., 23, pp. L795-L798, 1984.

Jelley,K.W., Alavi,K. and Engelmann,R.W.H., "Experimental determination of electroabsorption in GaAs/Al_{0.32}Ga_{0.68}As multiple quantum well structures as a function of well width", Elect. Lett., 24, pp. 1555-1557, 1988; and subsequent private communication.

Jewell,J.E., Huang,K.F., Tai,K., Lee,Y.E., Fisher,R.J., McCall,S.L. and Cho,A.Y., "Vertical cavity single quantum well laser", post-deadline for Top. Meet. on Photonic Switching, PD3, 1989.

Juang,F-Y., Singh,J., Bhattacharya,P.K., Bajema,K. and Merlin,R., "Field dependent linewidths and photoluminescence energies in GaAs-AlGaAs multi-quantum well modulators", Appl. Phys. Lett., 48, pp. 1246-1248, 1986.

Kawasaki,B.S., Hill,K.O., Johnson,D.C., and Tenne-Sens,A.U., "Full-duplex transmission link over single strand optical fibre", Opt. Lett., 1, pp. 107-108, 1977.

Kinoshita,S., and Iga,K., "Circular buried heterostructure (CBH) GaAlAs/GaAs surface emitting lasers", IEEE J. Quant. Elect., QE-23, pp. 882-888, 1987.

Klipstein,P.C. and Apsley,N., "A theory for the electroreflectance spectra of quantum well structures", J. Phys C, 19, pp. 6461-6478, 1986.

Kostuk,R.K., Goodman,J.W. and Hesselink,L., "Optical imaging applied to microelectronic chip to chip interconnections", Appl. Opt., 24, pp.2851-2858, 1985.

Koren,U., Miller,B.I., Tucker,R.S., Eisenstein,G., Bar-Joseph,I., Miller,D.A.B. and Chemla,D.S., "High frequency InGaAs/InP multiple quantum well buried mesa electro-absorption modulator", Elect. Lett., 23, pp. 621-622, 1987a.

Koren,U., Miller,B.I., Koch,T.L., Eisenstein,G., Tucker,R.S., Bar-Joseph,I., and Chemla,D.S., "Low-loss InGaAs/In P multiple quantum well optical electroabsorption waveguide modulator", Appl. Phys. Lett., 51, pp. 1132-1134, 1987b.

Koyama,F. and Iga,K., "Frequency Chirping in External Modulators", J. Light. Tech., 6, pp. 87-93, 1988.

Koyama,F., Kinoshita,S., and Iga,K., "Room temperature CW operation of GaAs vertical cavity surface emitting laser laser", Post deadline for

Optoelectronics Conf., Tokyo, PD-4, 1988.

Lang,D.V., Panish,M.B., Capasso,F., Allam,J., Hamm,R.A., Sergent,A.M. and Tsang,W.T., "Measurement of heterojunction band offsets in InP/Ga_{0.47}In_{0.53}As by admittance spectroscopy", J.Vac. Sci. Tech., 5, pp. 1215-1220, 1987.

Larsson,A., Yariv,A., Tell,R., Maserjian,J. and Eng,S.T., "Spectral and temporal characteristics of AlGaAs/GaAs superlattice p-i-n photodetectors" Appl. Phys. Lett., 47, pp. 866-868, 1985.

Larsson,A., Andrekson,P.A., Eng,S.T. and Yariv,A., "Tunable superlattice p-i-n photodetectors: characteristics, theory, and applications", IEEE J. Quant. Elect., 24, pp. 787-801, 1988.

Lentine,A.L., Hinton,H.S., Miller,D.A.B., Henry,J.E., Cunningham,J.E., Chirovsky,L.M.R., "Symmetric self electro-optic effect device: optical set-reset latch", Appl. Phys. Lett., 52, pp. 1419-1421, 1988.

Linke,R.A., "Transient chirping in single-frequency lasers: lightwave systems consequences", Elect. Lett., 20, pp. 472-475, 1984.

Linke,R.A., "Ultra-high speed digital transmission systems", Eur. Conf. Opt. Comm., pp. 127-131, 1987.

Matsumoto,Y., Matsuura,M., Tarucha,S. and Okamoto,H., "Direct observation of two-dimensional shrinkage of exciton wave function in quantum wells", Phys Rev. B, 32, pp. 4275-4278, 1985.

Matsusue,T. and Sakaki,H., "Radiative recombination coefficient of free carriers in GaAs-GaAlAs quantum wells and its dependence on temperature", Appl. Phys. Lett., 50, pp. 1429-1431, 1987.

Matsuura,M. and Kamizato,T., "Subbands and excitons in a quantum well in an electric field", Phys. Rev. B, 33, pp. 8385-8389, 1986.

McDonald,A.J., Fyath,R.S., O'Reilly,J.J., "Influence of extinction ratio on performance of optical receivers incorporating laser preamplifiers", Elect. Lett., 25, pp. 249-250, 1989.

Mead,C. and Conway,L., "Introduction to VLSI systems", Addison Wesley, pp. 230-231, 1980.

Midwinter,J.E., "Novel approach to the design of optically activated wide band switching matrices", IEE Proc. Pt. J, 134, pp. 261-268, 1987.

Miller,D.A.B., Chemla,D.S., Damen,T.C., Gossard,A.C., Wiegmann,W., Wood,T.H. and Burrus,C.A., "Novel hybrid optically bistable switch: The quantum well self electro-optic effect device", Appl. Phys Lett., 45, pp. 13-15, 1984.

Miller,D.A.B., Chemla,D.S., Damen,T.C., Gossard,A.C., Wiegmann,W., Wood,T.H., Burrus,C.A., "Electric field dependence of optical absorption near the band gap of quantum-well structures", Phys. Rev. B, 32, pp. 1043-1060, 1985.

Miller,D.A.B., Weiner,J.S. and Chemla,D.S., "Electric field dependence of linear optical properties in multiple quantum well structures : Waveguide

electroabsorption and sum rules", IEEE J. Quant. Elect., QE-22, pp. 1816-1830, 1986.

Miller,D.A.B., "Optics for low-energy communication inside digital processor: quantum detectors, sources, and modulators as efficient impedance converters", Opt. Lett., 14, pp. 146-148, 1989.

Miller,R.C., Kleinman,D.A. and Gossard,A.C., "Energy gap discontinuities and effective masses for GaAs-AlGaAs quantum wells", Phys. Rev. B, 29, pp. 7085-7087, 1984.

Miyazawa,T., Tarucha,S., Ohmori,Y., Suzuki,Y., Okamoto,H., "Observation of room temperature excitons in GaSb-AlGaSb multi-quantum wells", Jap. J. Quant. Elect., 25, pp. L200-202, 1986.

Moseley,A.J., Scott,M.D., Williams,P.J., Wallis,R.H., Davies,J.I., and Riffat,J.R., "Exciton electroabsorption at room temperature in InGaAs/InP multi-quantum well structures grown by atmospheric pressure MOCVD", Elect. Lett., 23, pp. 516-517, 1987.

Mozer,A.P., "Chirp free transmission conditions with directly modulated semiconductor lasers", Eur. Conf. Opt. Comm., pp. 365-368, 1986.

Nagai,N., Yamanishi,M., Kan,Y. and Suemune,I., "Field induced modulations of refractive index and absorption coefficient in GaAs/AlGaAs quantum well structures", Elect. Lett., 22, pp. 888-889, 1986.

Nakagawa,K. and Nosu,K., "An overview of very high capacity transmission technology for NTT networks", IEEE J. Light. Tech., LT 5, pp 1498-1504, 1987.

Nelson,D.F., Miller,R.C., Kleinman,D.A., "Band nonparabolicity effects in semiconductor quantum wells", Phys. Rev. B, 35, pp. 7770-7773, 1987a.

Nelson,D.F., Miller,R.C., Tu,C.W. and Spitz,S.K., "Exciton binding energies from an envelope-function analysis of data on narrow quantum well of integral monolayer widths in $Al_{0.4}Ga_{0.6}As/GaAs$ ", Phys. Rev. B, 36, pp. 8063-8070, 1987b.

Newson,D.J. and Kurobe,A., "Effect of residual doping on the optimum structure of multiple quantum-well optical modulators", Elect. Lett., 23, pp. 439-440, 1987.

Ninomiya,Y., Ohsuka,Y., Izumi,Y., Gohshi,S. and iwadate,Y., "A HDTV broadcasting system utilising a bandwidth compression technique-MUSE", IEEE Trans. Broad., BC-33, pp. 130-160, 1987.

Noda,S., Kojima,K., Mitsunaga,K., Kyuma,K., Hamanaka,K. and Nakayama,T., "Monolithic integration of an AlGaAs/GaAs multiple quantum well distributed feedback laser and a grating coupler for surface emission", Appl. Phys. Lett., 51, pp. 1200-1202, 1987.

Noda,Y., Suzuki,Y., Kushiro,Y. and Akiba,S., "High speed electroabsorption modulator with strip-loaded GaInAsP planar waveguide", J. Light. Tech., LT 4, pp. 1445-1453, 1986.

- Okiyama,T., Nishimoto,H., Touge,T., Seino,M. and Nakajima,H., "Optical fibre transmission over 132 km at 4 Gb/s using a Ti:LiNbO₃ Mach-Zehnder modulator" , Eur. Conf. Opt. Comm., Helsinki, pp. 55-58, 1987.
- Okiyama,T., Yokota,I., Nishimoto,H., Hironishi,K., Horimatsu,T. and Touge,T., "A 10-Gb/s, 65 km optical fibre transmission experiment using a monolithic electro-absorption modulator/DFB laser light source", Eur. Conf. Opt. Comm., Gothenberg, pp. 1-4, 1989.
- Olsson,N.A. and Buhl,L.L., "Single laser high-selectivity bidirectional transmission system for local area network applications", Elect. Lett., 23, pp. 62-64, 1987.
- Orton,J.W., Fewster,P.F., Gowers,J.P., Moore,K.J., Dobson,P.J., Curling,C.J., Foxon,C.T., Woodbridge,K., Duggan,G. and Ralph,H.I., "Measurement of "material" parameters in multi-quantum-well structures", Semicond. Sci. Technol, 1987, 2, pp. 597-607, 1987.
- Ozeki,T., Uematsu,T., Ito,T., Yamamoto,M. and Unno,Y., "Half-duplex optical transmission link using an LED source-detector scheme", Opt. Lett., 2, pp. 103-105, 1978.
- Presby,H.M., Amitay,N., Scotti,R. and Benner,A., "Simplifies laser to fibre coupling via optical fibre up-tapers", Elect. Lett., 24, pp. 323-324, 1988.
- Pucknell,D.A. and Estraghian,K., "Basic VLSI design: systems and circuits", Prentice Hall, pp. 75-87, 1988.
- Redfield,D., "Electric fields of defects in solids", Phys. Rev., 130, pp. 914-915, 1963.
- Roberts.J.S., Pate,M.A., Mistry,P., David,J.P.R., Franks,R.B., Whitehead,M. and Parry,G., "MOVPE grown MQW pin diodes for electro-optic modulators and photodiodes with enhanced electron ionisation coefficient", ICMOVPE, Japan, 1988.
- Sanders,G.D., Bajaj,K.K., "Electronic properties and optical absorption spectra of GaAs-GaAlAs quantum wells in externally applied electric fields", Phys. Rev. B, 35, pp. 3893-3898, 1987.
- Sarkar,C.K., Nicholas,R.J., Portal,J.C., Razeghi,M., Chevrier,J. and Massies,J., "Effective masses and non-parabolicity in Ga_xIn_{1-x}As", J. Phys. C, 18, pp. 2667-2676, 1985.
- Sauer,R., Harris,T.D. and Tsang,W.T., "Spectroscopy of excited states in In_{0.53}Ga_{0.47}InP single quantum wells grown by chemical beam epitaxy", Phys. Rev. B, 34, pp. 9023-9026, 1986.
- Shinada,M. and Sugano,S., "Interband optical transitions in extremely anisotropic semiconductors: I. Bound and unbound exciton absorption.", J. Phys. Soc. Jpn., 21, pp. 1936-1946, 1966.
- Shorthose,M.G., Maciel,A.C., Ryan,J.F., Scott,M.D., Davies,J.I. and Moseley,A., "Optical studies of excitons in GaInAs/InP quantum wells grown by low pressure metal organic vapour phase epitaxy", Semiconductor Sci. and Tech., pp. 612, 1986.

- Singh, J. and Hong, S., "Theory of field induced optical modulation in single and multiple quantum well structures using a Monte Carlo approach", IEEE J. Quant. Elect., QE-22, pp. 2017-2019, 1986.
- Singh, J., Hong, S., Bhattacharya, P.K., Sahai, R., Lastufka, C. and Sobel, H.R., "System requirements and feasibility studies for optical modulators based on GaAs/GaAlAs multiple quantum well structures for optical processing", J. Light. Tech., 6, pp. 818-831, 1988.
- Skolnik, M.S., Tapster, P.R., Bass, S.J., Pitt, A.D., Apsley, N. and Aldred, S.P., "Investigation of InGaAs-InP quantum wells by optical spectroscopy", Semicond. Sci. and Tech., 1, pp. 29-40, 1986.
- Smyth, P.P. and Hunkin, D.J., "High performance 2.4 Gbit/s PIN GaAs IC optical receiver", Eur. Conf. Opt. Comm., Brighton, pp 408, 1988.
- Stallard, W.A., Beaumont, A.R. and Booth, R.C., "Integrated optic devices for coherent transmission", J. Light. Tech., LT-4, pp.852-857, 1986.
- Stevens, P.J., Whitehead, M., Parry, G. and Woodbridge, K., "Computer modeling of the electric field dependent absorption spectrum of multiple quantum well material", IEEE J. Quant. Elect., 24, pp. 2007-2016, 1988.
- Stevens, P.J., Whitehead, M., Bradley, P.J., Rivers, A.W., Parry, G., Roberts, J.S., Mistry, P., Pate, M.A., and Hill, G. "Limits to the performance of transverse and waveguide electroabsorption and electrorefraction modulators", European Conference on Optical Communications, pp. 33-36, Brighton, Sept. 1988a.
- Tai, K., Hegarty, J., Tsang, W.T., "Nonlinear spectroscopy in $\text{In}_{0.53}\text{Ga}_{0.47}\text{As}/\text{InP}$ multiple quantum wells", Appl. Phys. Lett., 51, pp. 86-88, 1987.
- Tarucha, S., Iwamura, H., Saku, T. and Okamoto, H., "Waveguide type optical modulator of GaAs quantum well double heterostructure using electric field effect on exciton absorption", Jap. J. Appl. Phys., pp. L442-L444, 1985.
- Tarucha, S. and Okamoto, H., "Monolithic integration of a laser diode and an optical waveguide modulator having a GaAs/AlGaAs quantum well double heterostructure", 1986, Appl. Phys. Lett., 48, pp. 1-3.
- Tsang, D.Z., "Free-space optical interconnects", SPIE meeting, Boston, Sept. 1988.
- Van der Ziel, J.P. and Ilegems, M., "Multilayer GaAs- $\text{Al}_{0.3}\text{Ga}_{0.7}\text{As}$ dielectric quarter wave stacks grown by molecular beam epitaxy", Appl. Opt., 14, pp. 2627-2630, 1975.
- Viña, L., Collins, R.T., Mendez, E.E. and Wang, W.I., "Comparative study of the effect of an electric field on the photocurrent and luminescence of GaAs-GaAlAs quantum wells", Phys. Rev. B, 33, pp. 5939-5942, 1986.
- Viña, L., Mendez, E.E., Wang, W.I., Chang, L.L. and Esaki, L., "Stark shifts in GaAs/GaAlAs quantum wells studied by photoluminescence spectroscopy", J. Phys. C, 20, pp. 2803-2815, 1987.
- Wakita, K., Kawamura, K., Yoshikuni, Y. and Asahi, H., "High-temperature excitons and enhanced electroabsorption in InGaAs/InAlAs multiple quantum wells", Elect. Lett., 21, pp. 574-575, 1985.

- Wakita,K., Kawamura,Y., Nakao,M. and Asahi,H., "Long wavelength waveguide multiple quantum well optical modulators", IEEE J. Quant. Elect., QE 23, pp. 2210-2215, 1987.
- Wale,M.J., Duthie,P.J., Bennion,I., "The design of bidirectional fibre optic links using reflective modulation techniques", Proc. Eur. Conf. Opt. Commun., pp. 149-152, 1986.
- Walker, R.G., "High speed electrooptic modulation in GaAs/GaAlAs waveguide devices", J. Light. Tech., LT 5, pp. 1445-1453, 1987.
- Weiner,J.S., Chemla,D.S., Miller,D.A.B., Wood,T.H., Sivco,D. and Cho,A.Y., "Room temperature excitons in 1.6 μm band-gap GaInAs/AlInAs quantum wells", Appl. Phys. Lett., 46, pp. 619-621, 1985.
- Weiner,J.S., Miller,D.A.B. and Chemla,D.S., "Quadratic electro-optic effect due to the quantum confined Stark effect in quantum wells", Appl. Phys. Lett., 50, pp. 842-844, 1987.
- Weisbuch,C., "Fundamental properties of III-V semiconductor two-dimensional quantized structures: the basis for optical and electronic device applications", Semiconductors and Semimetals, vol 24, pp. 1-123, Academic Press, 1987
- Westlake,H.J. and O'Mahony,M.J., "Bidirectional and two-channel transmission system measurements using a semiconductor repeater amplifier", Elect. Lett., 23, pp. 649-651, 1987.
- Wheatley,P., Bradley,P.J., Whitehead,M., Parry,G., Midwinter,J., Mistry,P., Pate,M.A., Roberts,J.S., "Novel nonresonant optoelectronic logic device", Elect. Lett., 32, pp. 92-93, 1986.
- Wherrett,B.S., "Optical bistable interference filters: optimization considerations", J. Opt. Soc. Am. B, 3, pp. 351-362, 1986.
- Whitehead,M., Parry,G., Roberts,J.S., Mistry,P., Li Kam Wa,P. and David,J.P.R., "Quantum confined Stark shifts in MOVPE grown GaAs-GaAlAs multiple quantum wells", Elect. Lett., 23, pp. 1048-1050, 1987.
- Whitehead,M., Parry,G., Woodbridge,K., Dobson,P. and Duggan,G., "Experimental confirmation of a sum rule for room temperature electro-absorption in GaAs-AlGaAs multiple quantum well structures", Appl. Phys. Lett., 52, pp. 345-347, 1988a.
- Whitehead,M., Stevens,P.J., Rivers,A., Parry,G., Roberts,J.S., Mistry,P., Pate,M.A., Hill,G., "The effects of well width on the characteristics of GaAs/GaAlAs multiple quantum well electro-absorption modulators", Appl. Phys. Lett., 53, pp. 956-958, 1988b.
- Whitehead,M., Parry,G., and Wheatley,P., "Investigation of etalon effects in GaAs-AlGaAs multiple quantum well modulators", IEE Proc., Pt.J, 136, pp. 52-58, 1989a.
- Whitehead,M. and Parry,G., "High contrast reflection modulator at normal incidence in asymmetric Fabry Perot structure", Elect. Lett., 25, pp. 567-567, 1989b.

Whitehead,M., Rivers,A., Parry,G., Roberts,J. and Button,C., "A low voltage multiple quantum well reflection modulator with >100:1 on/off ratio", *Elect. Lett.*, 25, pp. 984-985, 1989c.

Wight,D.R., Allen,P.C., Trussler,J.W.A., Cooper,D.P., Esdale,D.J. and Oliver,P.E., "Ultra high speed micro-optical modulators in GaAs: The TEAM and the LEAM", *Int. Symp. GaAs and Related Compounds, Karuizawa, Japan*, pp. 667-672, 1985.

Wood,T.H., Burrus,C.A., Miller,D.A.B., Chemla,D.S., Damen,T.C., Gossard, A.C. and Wiegmann,W., "High speed optical modulation with GaAs/GaAlAs quantum wells in a p-i-n diode structure", *Appl. Phys. Lett.*, 44, pp. 16-18, 1984.

Wood,T.H., Burrus,C.A., Miller,D.A.B., Chemla,D.S., Damien,T.C., Gossard,A.C., "131 ps optical modulation in semiconductor multiple quantum wells (MQWs)", *IEEE J. Quant. Elect.*, QE-21, pp 117-118, 1985a.

Wood,T.H., Burrus,C.A., Tucker,R.S., Weiner,J.S., Miller,D.A.B., Chemla,D.S., Damen,T.C., Gossard, A.C. and Wiegmann,W., "100 ps waveguide multiple quantum well (MQW) optical modulator with 10:1 on/off ratio", *Elect. Lett.*, 21, pp. 693-694, 1985b.

Wood,T.H., Carr,E.C., Kasper,B.L., Linke,R.A., Burrus,C.A., "Bidirectional fibre-optical transmission using a multiple quantum well (MQW) modulator/detector", *Elect. Lett.*, 22, pp. 528-529, 1986a.

Wood,T.H., Carr,E.C., Burrus,C.A., Tucker,R.S., Chiu,T.-H. and Tsang,W.-T., "High speed waveguide optical modulator made from GaSb/AlGaSb multiple quantum wells (MQWs)", *Elect. Lett.*, 23, pp. 540-541, 1987.

Wood,T.C., Linke,R.A., Kasper,B.L. and Carr,E.C., "Observation of coherent Raleigh noise in single-source bidirectional optical fibre systems", *J. Light. Tech.*, pp. 346-351, 1988a.

Wood,T.C., Carr,E.C., Burrus,C.A., Miller,B.I. and Koren,U., "Large electroabsorption effect in GaInAs/InP multiple quantum well (MQW) optical modulator grown by OMVPE", *Elect. Lett.*, 24, pp. 840-841, 1988b.

Wood,T.C., "Multiple quantum well (MQW) waveguide modulators", *J. Light. Tech.*, 6, pp. 743-757, 1988c.

Wu,W.H., Bergman,L.A., Johnston,A.R., Guest,C.C., Esener,S.C., Yu,P.K.L., Feldman,M.R. and Lee,S.H., "Implementation of optical interconnections for VLSI", *IEEE Trans. Elect. Dev.*, ED-34, pp.706-714, 1987.

Yamamoto,H., Asada,M. and Suematsu,Y., "Electric-field induced refractive index variation in quantum well structure", *Elect. Lett.*, 21, pp. 579-580, 1988.

Yamanaka,K., Fukunaga,N., Tsukada,N., Kobayashi,K.L.I. and Ishii,M., "Photocurrent spectroscopy in GaAs/GaAlAs multiple quantum wells in an electric field perpendicular to the interface", *Appl. Phys. Lett.*, 48, pp. 840-842, 1986.

Yamanishi,M. and Suemune,I., "Comment on polarization dependent momentum matrix elements in in quantum well laser", *Jap. J. Appl. Phys.*, 23, pp. 135-136, 1984.

Zucker, J.E., Bar-Joseph, I., Miller, B.I., Koren, U. and Chemla, D.S., "Quaternary quantum wells for electro-optic intensity and phase modulation at 1.3 and 1.55 μm ", Appl. Phys. Lett., 54, pp. 10-12, 1989.

PREDICTED PERFORMANCE OF QUANTUM WELL GaAs/(GaAl)As OPTICAL AMPLIFIERS

Peter John Stevens

*Dept. of Electronic and Electrical Engineering,
University College London,
Torrington Place,
London WC1E 7JE,
England.*

Takaaki Mukai

*NTT Basic Research Laboratories,
Musashino,
Tokyo 180,
Japan.*

Abstract

The gain, noise and saturation performance of GaAs/(GaAl)As quantum well laser amplifiers is calculated. A single quantum well amplifier with 100 mA injection can achieve similar gains and saturation output powers to equivalent devices with bulk active regions, but with near ideal noise performance. A low current amplifier with a 2.5 mA injection current is investigated with different numbers and thicknesses of quantum wells.

Quantum wells (QW) have successfully been used in lasers to give low threshold currents, high speed operation and narrow linewidths [Tsang, Kobayashi and Mito]. These advantages arise from two basic properties of the QWs in the laser: the small active volume in which you need to achieve population inversion, and the high differential gain.

The use of quantum well for optical amplifiers has surprisingly received much less attention. We identify two areas where optical amplifiers might be useful. Firstly, they might be used as single devices as repeaters in long distance fibre optic communications, where they need to demonstrate in excess of 20 dB gain and saturation and noise performance similar or better than the existing bulk devices [Mukai and Yamamoto, 1981 and 1982]. Secondly, they might form part of an opto-electronic integrated circuit (OEIC) where the main requirement is for low drive currents. Koren et al. [] has recently achieved the integration of a (GaIn)As/InP QW amplifier with three DFB lasers and a optical combiner, clearly demonstrating the potential of using quantum wells in OEICs.

The large number of adjustable parameters (well width, number of wells, barrier height, waveguiding structure, injection current, active region width and device length) makes an experimental optimization of a quantum well amplifier a long and expensive process. Hence some form of theoretical model is useful.

In this paper we calculate quantum well gain as a function of current density in the standard way, and extend the calculation to consider the gain, noise and saturation properties of GaAs/(GaAl)As laser amplifiers. This material system is better characterized than the longer wavelength ones suitable for long distance communication (GaInAsP/InP, GaAlInAs/InP), but we hope the model will also be applicable to the latter materials

Calculation of Gain in Quantum Wells

The characterization of QW gain for relatively low injected current densities has been carried out by many authors [Agrawal and Dutta, Sugimura, Asada et al., Zielinsky et al., Blood et al., Chinn et al.] with the intent of minimising QW laser threshold currents. Our model is very similar to the above and it seeks to remain as simple as possible while retaining all of the important physical mechanisms limiting the gain in QWs.

the following steps:

i) Evaluation of Subband Energies

Quantum confinement in the well causes the conduction and valence bands to break up into a series of subbands with a step-like density of states function. The subband energies are equal to the energy levels in the finite quantum well defined by the spatial variation of the band edge in the well and barrier materials. These energies were calculated in the usual way [Agrawal and Dutta] assuming constant effective masses for the electron, heavy and light holes of $0.0667m_0$, $0.34m_0$ and $0.094m_0$, and a band offset ratio of 65% [Miller, R.C. et al.].

To calculate the transition energies, one adds the conduction and valence subband energies to the bandgap energy. In doing so it is important to include the bandgap renormalization, a shrinkage of the bandgap at high carrier densities [Kleinmann and Miller].

ii) Evaluation of Quasi-Fermi Levels

The quasi-Fermi levels in conduction and valence bands are evaluated such that the number of injected carriers equals the sum of the carriers in each subband as well as the number residing in 'unconfined' states above the barrier height. To avoid artificial discontinuities when the well width is such as to just introduce a new subband, for subbands of energies within 20 meV of the barrier energy, the density of electrons in that subband is assumed to drop linearly with the energy difference between subband edge and the barrier height. The number of unconfined carriers is estimated by assuming that both the well and barrier material act as bulk semiconductor of the same composition as the barrier material. The importance of including these states has been demonstrated by Nagarajan [], since under high injection, the conduction band Fermi level can be close to or above the barrier height. We neglect electrons in the L subbands because with the barriers of 20 % aluminium concentration considered in this paper, the L subband levels are at a greater energy than the unconfined states mentioned above.

iii) Unbroadened Gain

The gain is calculated assuming both a subband- and a k-selection rule. The following expression is used for the QW material gain with similar notation

$$g = \sum_{lh, hh} \sum_{\text{subbands}} \frac{2q^2 m_r^* |M_{qw}|^2}{\epsilon_0 m_0^2 c \hbar n_{in} E L_w} [f_c - f_v] H(E - E_{cv}^{n,n}) \quad (1)$$

where q is the electronic charge, m_r^* is the reduced mass, M_{qw} is the matrix element, ϵ_0 is free space dielectric constant, m_0 is the free space electron rest mass, c is the speed of light, \hbar is Planck's constant, n_{in} is the refractive index (3.63), E is the photon energy, L_w is the well width, f_c and f_v are the conduction and valence band Fermi functions, which in the case of f_v is the probability of finding a electron (as opposed to a hole), and $E_{cv}^{n,n}$ is the energy separation between the n^{th} conduction and valence subbands.

There is an extra factor of 2 compared to [Agrawal and Dutta] which arises from the fact that four, and not two, spin transition combinations are associated with each k -space transition. This means we are using almost exactly the same expression as Chinn et al. [].

M_{qw} is dependent upon photon energy, polarization and whether the subband is a light or heavy hole. We use expressions derived by Asada et al. [] and Yamanishi and Suemune [], the one for the TE mode being:

$$M_{qw}^{hh,TE} = (3/4 + 3E_v^n/4E_v) |M_b|^2 \quad (2)$$

$$M_{qw}^{lh,TE} = (5/4 - 3E_v^n/4E_v) |M_b|^2 \quad (3)$$

where M_b is the average momentum matrix element for the well material Bloch states with $|M_b|^2$ equal to 1.735×10^{-30} eVkg, and E_v and E_v^n the energies of the excited valence band state and the valence subband with respect to the well material valence bandedge.

We find that if the equivalent TM mode expressions are used, the TE/TM material gain difference reduces and even reverses at high carrier densities. Experimental measurements, although not at such high carrier densities [Kobayashi, H. et al.], do not show such behaviour and this brings into question the validity of the standard gain model. The discrepancy might be explained by the lack of band-mixing in the model, which has been shown to be significant in the calculations of Colak et al. []. However we have chosen to retain the simplicity of the standard model for the TE mode, in the knowledge that relatively good agreement has been found between theory and experiment when modelling quantum well laser thresholds [Chinn et

iv) Broadening

The sharp step-like spectra predicted by the theory above are not seen in practice because of broadening arising from well width fluctuations [Blood], and scattering by phonon and carrier-carrier interactions. The well width fluctuation broadening is added to each subband separately, with a Gaussian shape and a linewidth proportional to the rate of change in subband energy with the well width [Juang et al.]. A RMS well width fluctuation of 1 monolayer is assumed.

The carrier-carrier scattering linewidth is taken from calculations by Asada [] and is added to a phonon linewidth of 6.3 meV, derived taken from exciton linewidths in MQW absorption spectra [Stevens et al.]. Yamanishi and Lee [] have considered the best lineshape to use for such homogeneous broadening and show that the correct one is between a Lorentzian and a Gaussian. We use a Gaussian one because the Lorentzian shape has unrealistically large bandtails which tend to depress the gain peak artificially.

Figure 1 shows the gain spectra for a 100 Å quantum well for injected carrier densities from 2×10^{18} to $30 \times 10^{18} \text{ cm}^{-3}$. For carrier densities of $10 \times 10^{18} \text{ cm}^{-3}$ and above, the $n=2$ peak is clearly defined and of higher gain than the $n=1$ peak.

Recombination Mechanisms

The injected current is determined by the recombination rate, the dominant mechanism at small carrier densities being radiative recombination of confined carriers in the well given by

$$R_{\text{rad}} = \frac{N}{N_w} \sum_{lh, hh} \sum_{\text{subbands}} \int_{-\infty}^{\infty} \frac{32\pi^2 n_{\text{in}} q^2 m_r^* E |M_{\text{qw}}|^2}{\epsilon_0 m_0^2 h^4 c^3 L_w} \times f_c [1 - f_v] H(E - E_{\text{cv}}^{n,n}) dE \quad (4)$$

where N_w is the density of confined carriers in the quantum well and N is the sum of the confined and unconfined carriers. Here we are assuming that the unconfined carriers in the barriers have the same recombination time as

The active region in a quantum well laser is very small, and hence the carrier densities are very high. In this regime it is important to include non-radiative forms of recombination that contribute to the total injected current. Two non-radiative mechanisms are considered in our model: Auger recombination and current leakage into the far cladding region.

The Auger rate for the quantum well is derived from measurements in bulk GaAs is given by [Takeshita, Chinn et al.]:

$$R_{\text{aug}} = C_p NP^2 + C_n N^2 P \quad (5)$$

where P is the hole density, and C_p and C_n are the Auger coefficients of $3.33 \times 10^{-30} \text{ cm}^6 \text{ s}^{-1}$ and $1.75 \times 10^{-31} \text{ cm}^6 \text{ s}^{-1}$ respectively.

The leakage current is calculated in the same way as described in Casey and Panish and Wu and Yang. The minority carrier concentration at the cladding edge is assumed to be in thermal equilibrium with the carriers in the quantum wells, and a diffusion current is set up as the carrier recombine in the cladding. To calculate the energy of the cladding bands with respect to the the quantum well, it is assumed that the majority carrier Fermi level is equal to that within the quantum well. The total leakage current is then

$$J_{\text{lk}} = P_{\text{cl}} q D_p / L_p + \sum_{\Gamma, X, L} N_{\text{cl}} q D_n / (L_n \tanh(s/L_n)) \quad (6)$$

where the summation is over the Γ, X and L conduction bands, N_{cl} and P_{cl} are the minority carrier concentration at the cladding edges, D_n and D_p are the conduction and valence band diffusion constants, L_n and L_p are the conduction and valence diffusion lengths and s is the distance from the edge of the GRIN to the contact (assumed to be $1 \mu\text{m}$). The Γ, X, L and valence band diffusion constants and lengths are taken as $76, 5.1, 50.8$ and $7.6 \text{ cm}^2 \text{ s}^{-1}$ and $1.23, 0.31, 1.01$ and $0.39 \mu\text{m}$. The cladding regions are assumed to be doped to a level of $5 \times 10^{17} \text{ cm}^{-3}$. It is found for high aluminium cladding regions, the dominant bands contributing to the leakage are the X and the valence bands, as might be expected for an indirect material.

The current, excluding any due to intensity-dependent stimulated emission is then given by

$$J_{\text{ns}} = q M L_w (R_{\text{rad}} + R_{\text{aug}}) + J_{\text{lk}} \quad (7)$$

carrier density for single wells of 50,75,100,125 and 150 Å width. A feature of the gain-current relationship of quantum well material is its non-linearity, with gain flattening due to the step-like density of states and the non-radiative recombination mechanisms.

The model has also been compared to experimental and theoretical results of Chinn et al., and good agreement is obtained with their 75 Å data.

Design of Waveguiding Region

The quantum wells alone are not sufficient to obtain high confinement, and hence it is beneficial to add additional layers to form an efficient waveguide. The use of graded index (GRIN) regions was developed by Tsang [] for low threshold quantum well lasers. To evaluate the confinement factors for an given GRIN index profile, we split the profile up into a series of flat steps so that the modal function within each step is sinusoidal or its' evanescent equivalent. Hence a simple transfer matrix approach, similar to that used in evaluating energy levels in tilted quantum wells [Stevens et al.], can be used to evaluate the waveguiding modes. This method enables us to consider graded index regions of arbitrary shape and find the widths of such regions that give the maximum confinement factors.

We find that there is no appreciable difference in the confinement factors for GRIN regions with different profiles (parabolic, linear or separate confinement) so we choose a linear one in order to minimise the number of carriers spilling out of the well.

Figure 3 shows the confinement factor as a function of the number of wells and well width, when the optimum width of GRIN region is used. The barriers between wells are 60 Å in width and have an aluminium concentration of 20 %, the value found to minimise the threshold current in QW lasers [Tsang]. The cladding regions to either side of the GRIN have an aluminium concentration of 80 %, in order to obtain high confinement factors and reduce leakage currents. For few wells the overall GRIN width is of the order of 0.25 µm.

Finally we note that while high confinement gives the maximum device gain, it also increases the intensity at the QWs for a given output power (and hence lowers the saturation output power) and increases the difficulty of coupling into the device. In cases of excess material gain, the confinement

performance.

Specification of Amplifier Performance

After modelling the gain in quantum wells we go on to consider the performance of a real device, notably the device gain, and its noise and saturation properties. We consider a perfect travelling wave amplifier rather than a Fabry-Perot one with finite reflectivities at both ends, so as to concentrate upon the properties of QWs and to keep the analysis simple.

The amplifier gain can then be expressed by

$$G = \exp\{(\Gamma g - \alpha)L\} \quad (8)$$

where Γ is the confinement factor, α is the waveguide loss, assumed to be 5 cm^{-1} , and L is the amplifier length. This expression neglects effects of imperfect non-perfect anti-reflection coatings and saturation due to amplified spontaneous emission, which are likely to restrict the device gain to around 30 dB.

The noise produced by amplifiers is caused by the spontaneous emission and is composed of several separate beat and shot noise contributions [Mukai and Yamamoto, 1982]. All can be characterised in terms of the ratio between the spontaneous and stimulated rates, commonly called the spontaneous noise parameter or population inversion parameter (n_{sp}). For n_{sp} we use the expression used by Arakawa and Yariv []:

$$n_{sp} = \frac{1}{\{1 - \exp[(E - \Delta E_f)/kT]\}} \frac{\Gamma g}{\{\Gamma g - \alpha\}} \quad (9)$$

where ΔE_f is the energy separation between conduction and valence Fermi levels, k is Boltzmann's constant and T is the temperature.

When the signal-spontaneous beat noise exceeds the other types, we can define a noise figure, the ratio of the effective beat noise at the input to the unavoidable signal shot noise present. It can be expressed by [Saitoh and Mukai]:

$$F = 2n_{sp}\chi \quad (10)$$

where χ is excess noise factor, almost equal to 1 for a perfect travelling wave

Gain saturation occurs when high optical intensities cause the stimulated emission rate to reduce the carrier density and hence suppress the gain. With a linear gain curve and a constant carrier lifetime, the gain can be written as [Mukai and Yamamoto, 1981]

$$g = \frac{g_0}{(1+(I/I_s))} \quad (11)$$

where g_0 is the unsaturated gain, I is the intensity in the active region and I_s is the saturation intensity given by

$$I_s = \frac{E}{\tau_c \partial g / \partial N} \quad (12)$$

where τ_c is the carrier lifetime, and $\partial g / \partial N$ is the differential gain.

However at high carrier densities both the gain curve is nonlinear and the carrier lifetime changes as a result of leakage currents and Auger recombination. In this case the evaluation of the intensity dependent gain needs more careful consideration of the gain saturation effect. At high intensities the current associated with the stimulated emission becomes significant and carrier density must drop to reduce other forms of recombination. Current conservation states that

$$J_{tot} = J_{ns} + g(J_{ns})qML_w I / E \quad (13)$$

where J_{tot} is the total injected current density, J_{ns} is the current density excluding recombination current through stimulated emission and the last term describes the stimulated emission current. For a given intensity, I , J_{ns} must be found to satisfy the above equation. Hence the saturation performance is derived from the small signal gain-current relationship (g vs. J_{ns}).

In figure 4 we see a comparison between the accurate and approximate methods of calculating the intensity dependent gain for injected current densities of 40000 Acm^{-2} and 1000 Acm^{-2} . At the higher current density the use of equation (11) is clearly inaccurate, with the gain at low intensities underestimated due to the increase in carrier lifetime with reduced injected carrier concentration, whereas at high intensities the gain is overestimated because of the non-linear gain profile. The agreement at the lower current

The saturation output power is the power at which the amplifier gain drops by 3 dB, and it is found by integration of the intensity dependent gain through the length of the amplifier.

$$G = \exp \left\{ \int_0^L \Gamma g(I(z)) - \alpha \, dz \right\} \quad (14)$$

Other important device properties of the amplifier are the optical bandwidth and TE/TM gain difference. The optical bandwidth, estimated from figure 1, of the order of 30 nm for most devices. The TE/TM gain difference is not evaluated here because of the neglect of band-mixing in the simple gain model. More sophisticated gain models and experimental measurements will be required to determine this TE/TM gain difference.

High Output Power Amplifiers

For the best noise and saturation performance in a quantum well amplifier one wants to achieve as high a population inversion as possible and hence we start by evaluating a device a single quantum well in the active region. We choose a amplifier of 1 μm wide and 250 μm long, a length typical of laser amplifiers with bulk material active regions: long enough to provide reasonable gains, and short enough to ensure reasonable saturation output powers.

We choose a well width of 100 \AA , which has an associated confinement factor of 4.385%. Figure 5 plots the device gain at the $n=1$ and $n=2$ peak wavelengths (around 855 nm and 795 nm respectively) as a function of the injected current into the device. Rather unexpectedly, even with a single quantum well it is possible to achieve gains of 20-30 dB at the $n=1$ peak wavelength. The device gain is found not to vary significantly with well width as the L_w^{-1} dependence of the gain in expression (1) is cancelled by the L_w dependence of the confinement factor.

Figure 6 shows the spontaneous noise parameter, and it is clearly evident that unlike bulk material, it is possible to approach the ideal value of 1. Non quantum well amplifiers have values of 2-3. In figure 7 we show the output saturation power. At higher currents the dependence with injection current is almost linear, a result of the flat gain current relationship at these

the local gain significantly but does provide proportionally more carriers for the stimulated gain process.

The $n=2$ gain peak starts to exceed that of the $n=1$ gain peak at a relatively low current. In figure 5 we truncate the $n=2$ gain curve when calculated gain rise significantly above 30 dB since we believe that such gains will be unrealisable as a result of finite facet reflectivities and amplified spontaneous emission. In these cases it is advantageous to reduce the optical confinement so that the saturation performance and ease of coupling into the device are improved. Surprisingly, when the confinement factor is reduced so that the device gain is equal to that of the original $n=1$ peak gain, the saturation performance for the modified $n=2$ device is almost equal to the $n=1$ performance. The explanation is that the increased photon energy, which reduces number of electrons required per unit optical power, is balanced by the fact that the $n=2$ gain peak subsides at a higher carrier density than the $n=1$ peak.

The introduction of more quantum wells increases the confinement factor so that, as in the $n=2$ peak case, calculated device gains are too high to be realistic. Again the confinement can be relaxed to achieve to improve saturation and coupling properties. In amplifiers with the same injected current and device gain, the confinement required for a double well device is just over half that of the single well one, and the resultant saturation output power is only 10 % lower.

Low Current Amplifiers

In the high current quantum well amplifier described in the previous section, the device uses the small active region together with high injection current to give low noise and a high saturation output power. Alternatively the small active region can be used to achieve population inversion, and hence amplification, at much smaller currents suitable for OEICs. To demonstrate what can be achieved, we limit the device current to 2.5 mA, choose the same cavity length and width as before ($250 \times 1 \mu\text{m}$), and calculate device performance for varying well widths and number of wells.

Figure 8 shows how the device gain is maximised (22 dB) with 3 wells of 75 Å. For thinner wells the heavy and light hole subbands separate, whereas thicker wells have more subbands to fill and hence the Fermi level is lowered. The number of wells is such as to place the operating point on the

parameter is close to 1 for a single well, but additional wells lower the Fermi level and increases n_{sp} . For reasons of computational efficiency, the saturation output power shown in figure 10 is calculated utilizing expression (11), accurate enough because of the relatively low current densities.

With an increased injected current, the gain, noise and saturation properties all improve.

Conclusions

The performance of quantum well GaAs/(GaAl)As optical amplifiers has been predicted and it is found that the ability to obtain high injected carrier densities in the small active region gives them superior properties to their bulk counterparts. In a single device repeater or preamplifier application, the small active region can be pumped very hard to achieve a gain of 20-30 dB, almost ideal noise due to almost complete population inversion, and saturation output powers similar to bulk devices. For calculation of the saturation performance a new model was developed to deal with of the non linear gain characteristic and non-radiative recombination mechanisms. Single quantum wells give the best noise and saturation performance but need high confinement, a requirement which can be relaxed by using more wells.

For an OEIC application, a attractive novel feature of quantum well amplifiers is their low injected currents, as small as 2.5 mA. The device gain is maximised with 3 QWs of 75 Å width.

Acknowledgements

Peter Stevens is most grateful to Cable and Wireless plc and Plessey Research for providing financial support for visiting Japan. We thank Dr. H. Kanbe, Dr. T.Kimura and Dr. Parry for arranging the trip and encouraging the work. The authors would also like to acknowledge stimulating discussions with Dr. A.Sugimura, Prof. M.Asada, Prof. M.Yamanishi, Dr. P.Blood and Dr. A.Kucharska.

References

Tsang,W.T., "Extremely low threshold (AlGa)As modified multiquantum

Kobayashi,K. and Mito,I., "Single frequency and tunable laser diodes", IEEE J. Light Tech., LT-6, pp 1623-1633, 1988.

Koren,U., Eisenstein,G., Tucker,R.S., Koch,T.L. and Miller,B.I., " Integrated multiple quantum well lasers and optical amplifiers at 1.55 micron wavelength", Top. Meet. on QWs for Optics and Optoelectronics, Salt Lake City, pp. 128-131, March 1989.

Mukai,T. and Yamamoto,Y., "Gain, frequency bandwidth, and saturation output power of AlGaAs DH laser amplifiers", IEEE J. Quant. Elect., QE-17, pp. 1028-1034, 1981.

Mukai,T. and Yamamoto,Y., "Noise in an AlGaAs semiconductor laser amplifier", IEEE J. Quant. Elect., QE-18, pp. 564-574, 1982.

Agrawal,G.P. and Dutta,N.K., "Long wavelength semiconductor lasers", Von Nostrand Rienhold, 1986.

Sugimura,A., "Threshold currents for AlGaAs quantum well lasers", IEEE J. Quant. Elect., QE-20, pp. 101-108, 1984.

Asada,M., Kameyama,A. and Suematsu,Y., "Gain and intervalence band absorption in quantum-well lasers", IEEE J. Quant. Elect., QE-20, pp. 745-753, 1984.

Arakawa,Y., and Yariv,A., "Quantum well lasers-gain, spectra, dynamics", IEEE J. Quant. Elect., QE-22, pp. 1887-1899, 1986.

Zielinsky,E., Schweizer,H., Hausser,S., Stuber,R., Pilkuhn,M.H. and Weimann,G., "Systematics of laser operation in GaAs/AlGaAs multiple quantum well heterostructures", IEEE J. Quant. Elect., QE-23, pp. 969-975, 1987.

Blood,P., Colak,S., Kucharska,A.I., "Influence of broadening and high-injection effects on GaAs/GaAlAs quantum well lasers", IEEE J. Quant.

Chinn,S.R., Zory,P.S. and Reisinger,A.R., "A model for GRIN-SCH-SQW diode lasers", IEEE J. Quant. Elect., QE-24, pp. 2191-2214, 1988.

Miller,R.C., Kleinman,D.A. and Gossard,A.C., "Energy gap discontinuities and effective masses for GaAs-GaAlAs quantum wells", Phys. Rev. B, 29, pp. 7085-7087, 1984.

Kleinman,D.A., and Miller,R.A., "Band-gap renormalisation in semiconductor quantum wells containing carriers", Phys. Rev. B, 32, pp. 2266-2272, 1985.

Nagarajan,R., Kamiya,T., and Kurobe,A., "Band filling in GaAs/AlGaAs in multiple quantum well lasers and its effect on the threshold current", IEEE J. Quant. Elect., 25, pp. 1161-1170, 1989.

Yamanishi,M., and Suemune,I., "Comment on polarization dependent momentum matrix elements in quantum well lasers", Jap. J. Appl. Phys., 23, pp. 135-36, 1984.

Kobayashi,H., Iwamura,H., Saku,T. and Otsuka,K., "Polarisation dependent gain-current relationship in GaAs/AlGaAs MQW laser diodes", Elect. Lett., 19, pp. 166-167, 1983.

Colak,S., Eppenga,R., and Schuurmans,M.F.H., "Band mixing effects on quantum well gain", IEEE J. Quant. Elect., QE-23, pp. 960-968, 1987.

Juang,F.-Y., Singh,J., Bhattacharya,P.K., Bajema,K. and Merlin,R., "Field dependent linewidths and photoluminescence energies in GaAs-AlGaAs multiple quantum well modulators", Appl. Phys. Lett., 48, pp. 1246-1248, 1986.

Asada,M., Hausser,S., Zielinski,E. and Pilkuhn,M., "Intraband relaxation time in quantum well lasers due to carrier-carrier scattering", Int. Quant. Elect. Conf., Tokyo, TuP44, pp. 419, 1988.

Yamanishi,M. and Lee,Y., "Phase dampings of optical dipole moments and

Stevens,P.J., Whitehead,M., Parry,G. and Woodbridge,K., "Computer modeling of the field dependent absorption spectrum of multiple quantum well material", IEEE J. Quant. Elect., 24, pp. 2007-2016, 1988.

Takeshima,M., "Effect of Auger recombination on laser operation in $Ga_{1-x}Al_xAs$ ", J. Appl. Phys., 58, pp. 3846-3850, 1985.

Casey,H.C.,Jnr. and Panish,M.B., "Heterostructure lasers, Part A", Academic Press, 1978.

Wu,C.-M. and Yang,E.S., "Physical mechanisms of carrier leakage in DH injection lasers", J. Appl. Phys., 49, pp. 3114-3117, 1978.

Tsang,W.T., "Extremely low threshold (AlGa)As graded index waveguide separate-confinement heterostructure lasers grown by molecular beam epitaxy", Appl. Phys. Lett., 40, pp. 217-219, 1982.

Simon,J.C., "GaInAsP semiconductor laser amplifiers for single- mode fiber communications", J. Light. Tech., LT-5, pp. 1286-1295, 1987.

Saitoh,T. and Mukai,T., "1.5 μm GaInAsP traveling-wave semiconductor laser amplifier", QE-23, pp 1010-1020, 1987.

Figure 1

Gain spectra of a quantum well of 100 Å width for carrier densities between 2×10^{18} and $30 \times 10^{18} \text{ cm}^{-3}$. The barrier are of 20% aluminium and the polarization is TE.

Figure 2

Material gain of n=1 subband peak as a function of injected current density for a single quantum wells of widths between 50 Å and 150 Å.

Figure 3

Optimum confinement factor for TE mode against well width for 1 to 10 wells. The graded regions are linear with aluminium concentrations shown in the inset.

Figure 4

Plot of material gain against optical intensity for current densities of 1000 Acm^{-2} (lower curves) and 40000 Acm^{-2} (upper curves). The straight lines are those calculated from full current-gain relationship, whereas the dotted ones are calculated using equation (11).

Figure 5

Device gain against injected current for a single 100 Å quantum well with cavity dimensions $1 \times 250 \text{ } \mu\text{m}$. The solid line is for the n=1 gain peak whereas the dotted one is for the n=2 peak, truncated because gains of significantly greater than 30 dB are unrealizable because of neglected saturation through the amplified spontaneous emission and finite facet reflectivities.

Figure 6

Spontaneous noise parameter (n_{sp}) against injected current for a single 100 Å quantum well with cavity dimensions $1 \times 250 \text{ } \mu\text{m}$.

Figure 7

Saturation output power as a function of injected current for a single 100 Å quantum well with cavity dimensions 1 x 250 μm.

Figure 8

Device gain of optical amplifier against well width for 1 to 10 wells. The injected current is 50 mA and the cavity dimensions are 1 x 250 μm.

Figure 9

Spontaneous noise parameter (n_{sp}) of optical amplifier against well width for 1 to 10 wells. The injected current is 50 mA and the cavity dimensions are 1 x 250 μm.

Figure 10

Saturation output power of optical amplifier against well width for 1 to 10 wells. The injected current is 50 mA and the cavity dimensions are 1 x 250 μm. The intensity dependent gain is calculated using the approximate equation (11).

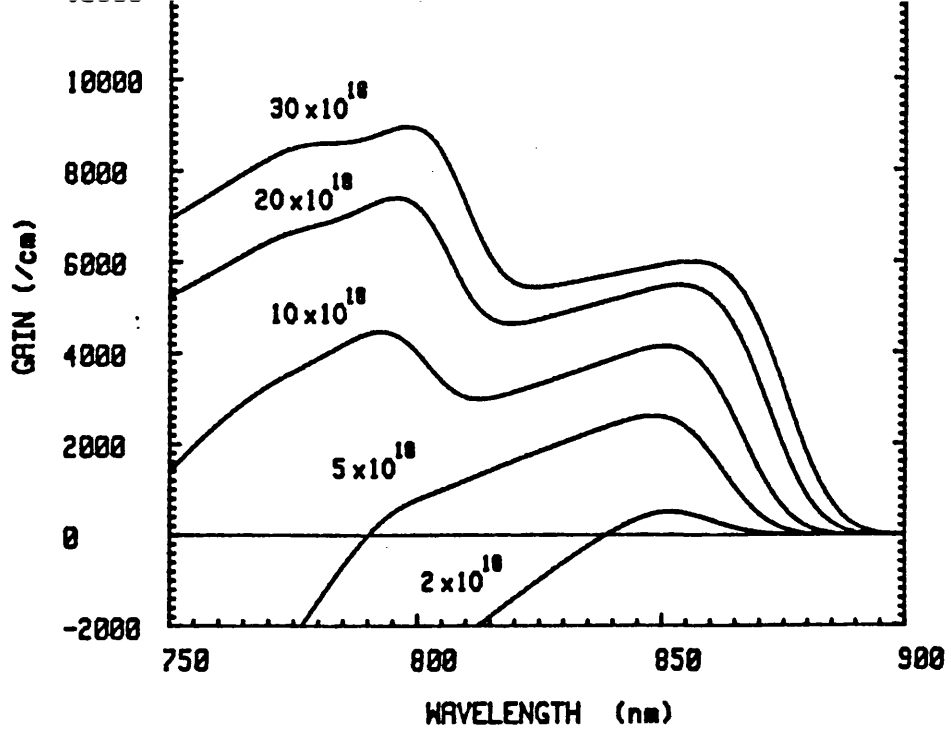


Figure 1

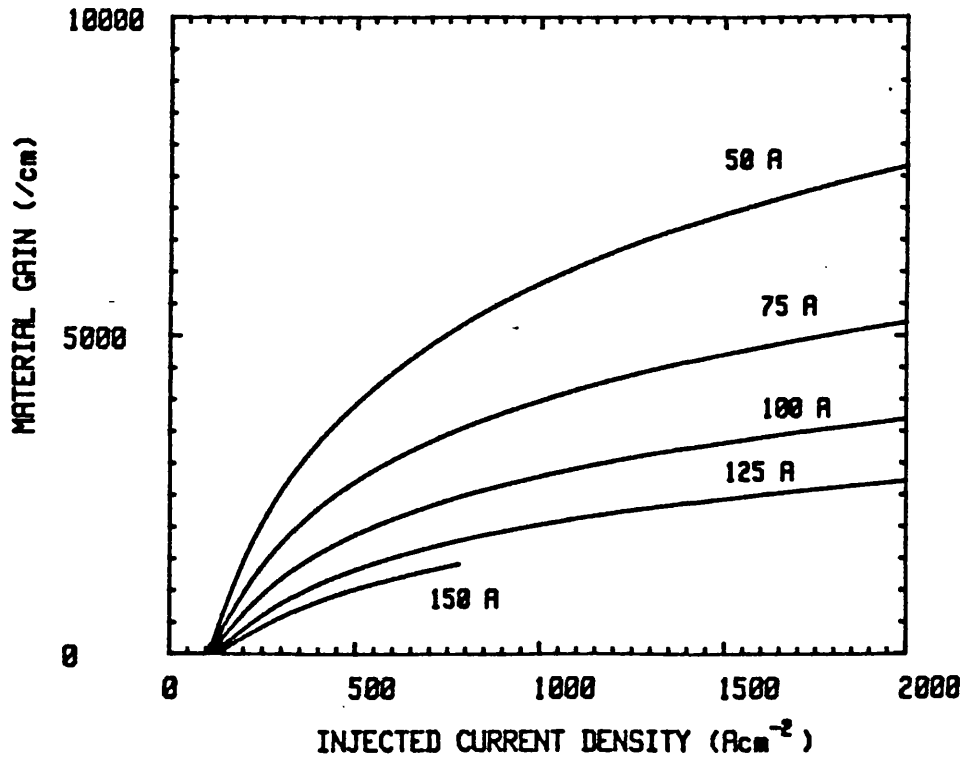


Figure 2

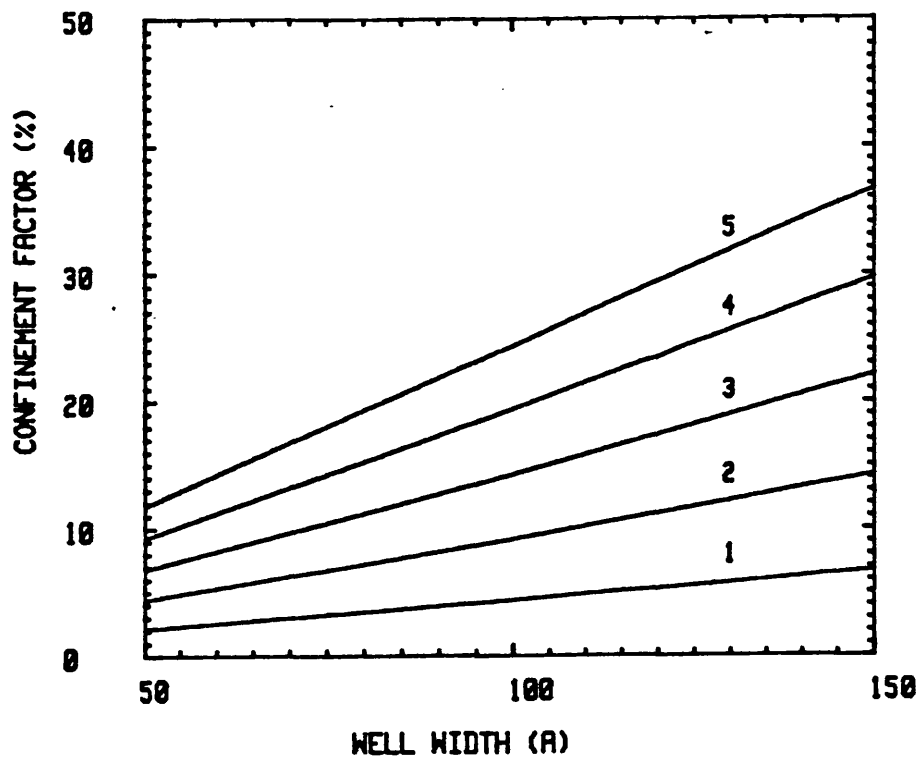


Figure 3

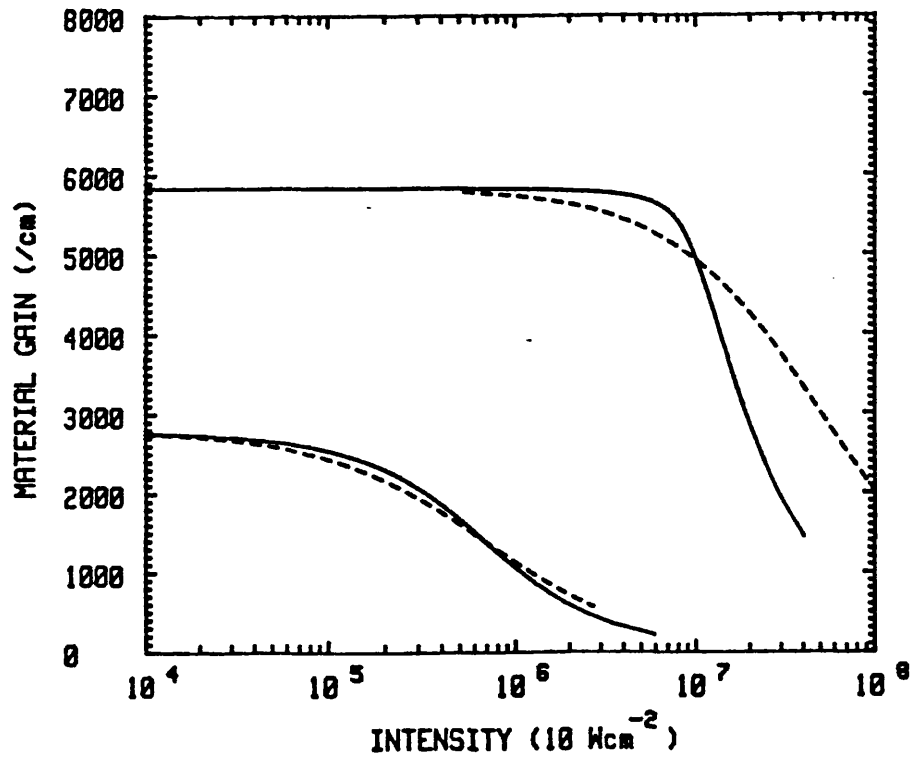


Figure 4

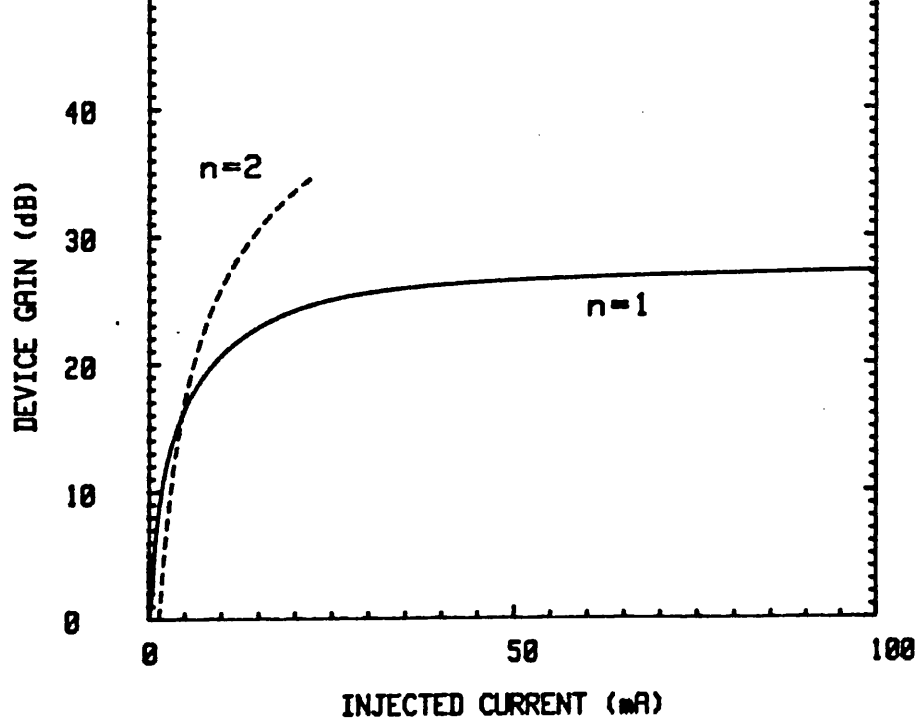


Figure 5

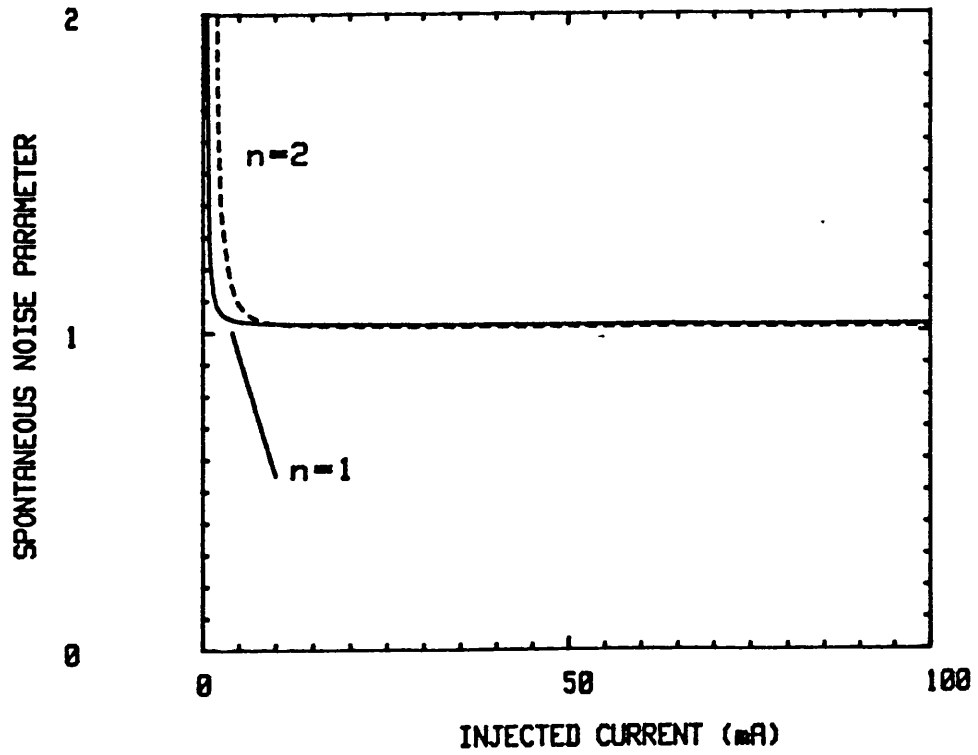


Figure 6

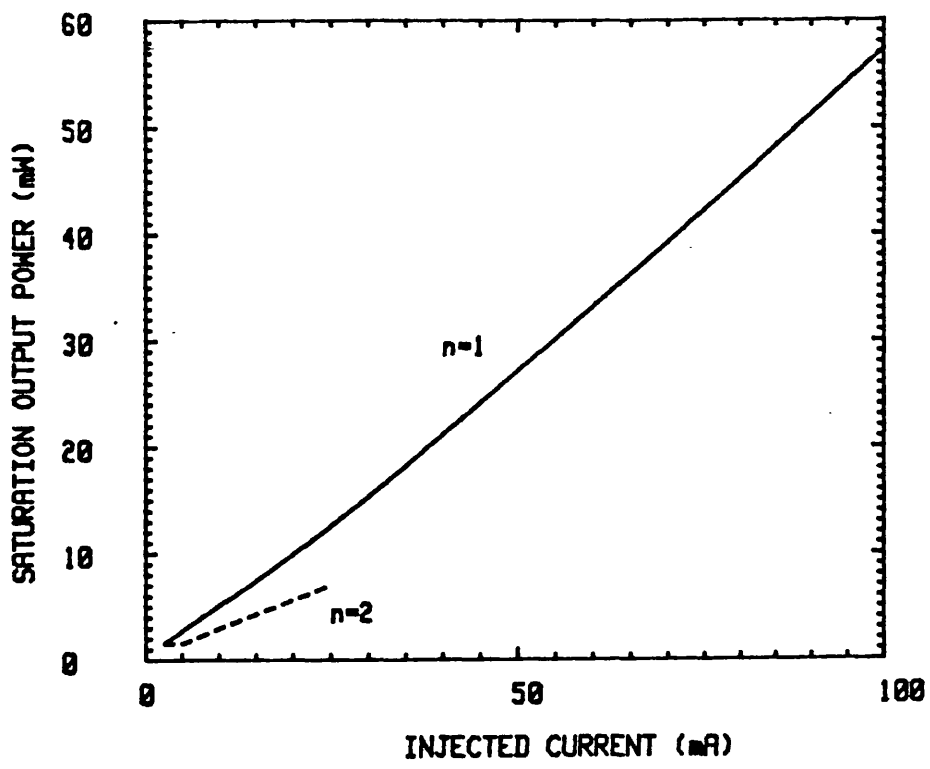


Figure 7

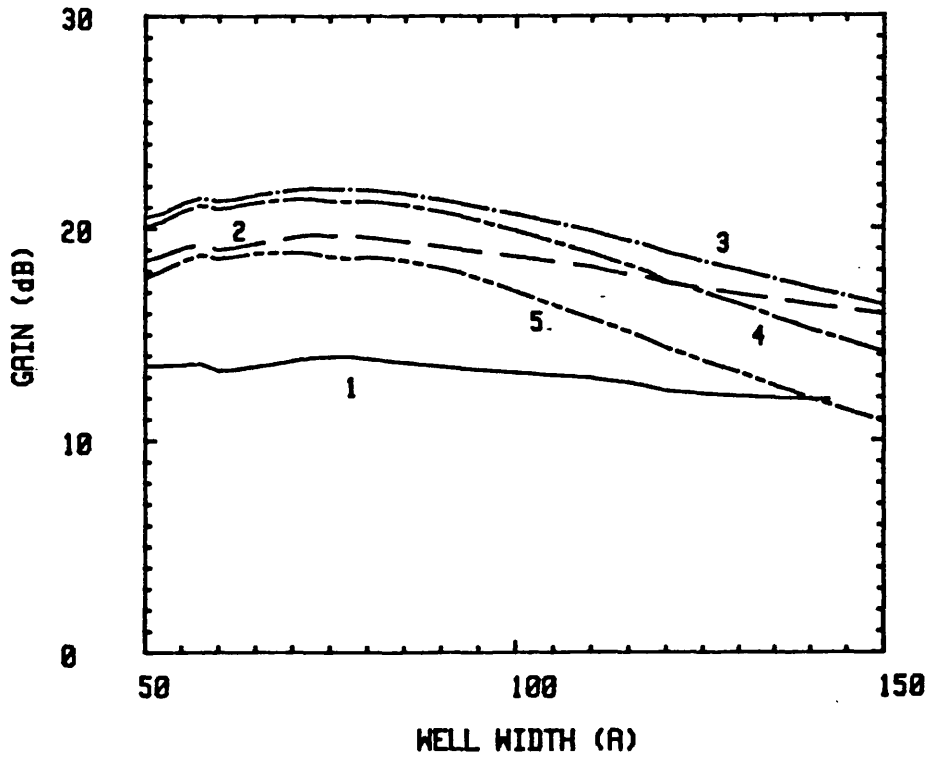


Figure 8

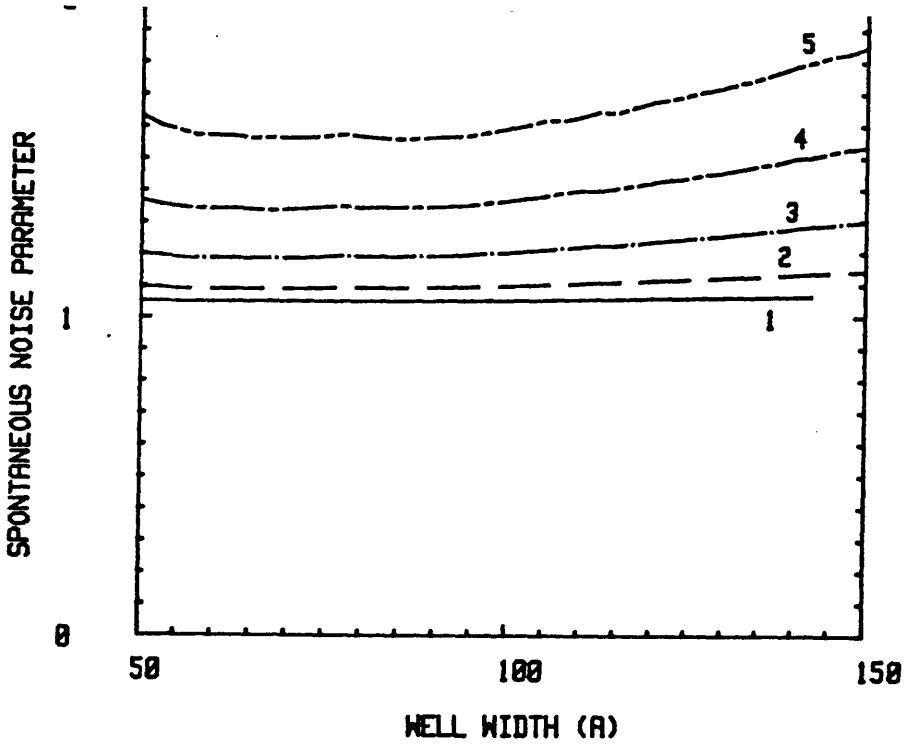


Figure 9

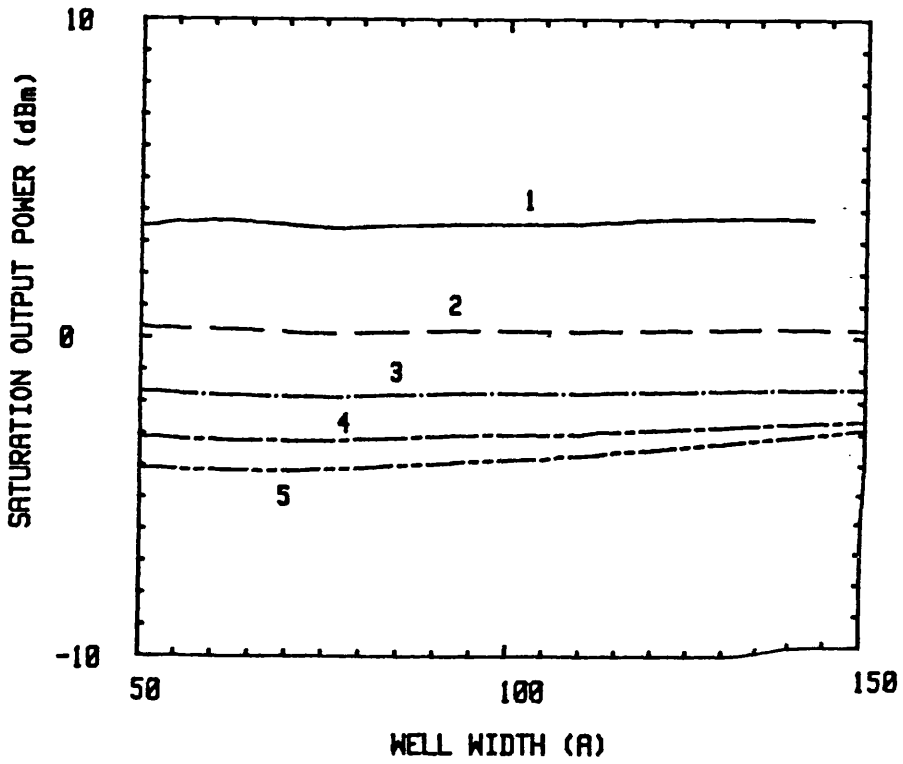


Figure 10